

AN ABSTRACT OF THE DISSERTATION OF

Beau Baukol for the degree of Doctor of Philosophy in Physics presented on
May 17, 2001. Title: Alternating-Current Thin-Film Electroluminescent
Device Fabrication and Characterization.

Redacted for privacy

Abstract approved: _____

John F. Wager

The goals of this thesis are to provide an improved understanding of luminescent materials, and to exploit their properties to achieve bright, efficient, and manufacturable red, green, and blue (RGB) phosphors for use in full-color flat-panel displays. A high-luminance, high-efficiency, full-color alternating-current thin-film electroluminescent (ACTFEL) phosphor system, capable of being processed at temperatures below the glass substrate melting temperature, has been developed through the use of source layer diffusion doping (SLDD) of atomic layer epitaxy (ALE) deposited SrS thin-films. The development of ACTFEL phosphors has also been advanced through the exploration of alternate phosphor materials, such as $\text{Sr}_x\text{Ca}_{1-x}\text{S}:\text{Eu,Cu}$ and $(\text{Ba,Zn})\text{S}:\text{Mn}$.

This thesis offers new insight into the nature of ACTFEL device operation, especially SrS:Cu ACTFEL devices. A comparison of "EL" thermal quenching trends for evaporated ZnS:Mn, ALE ZnS:Mn, ALE SrS:Ce, sputtered SrS:Cu,Ag, and sputtered multi-layer SrS:Cu,Ag / SrS:Ce ACTFEL devices is presented. ZnS:Mn ACTFEL devices exhibit the least amount of EL thermal quenching, which is attributed to non-radiative recombination. SrS:Cu and SrS:Cu,Ag ACTFEL devices possess the greatest amount of thermal quenching, which is primarily EL thermal quenching. The extent of EL thermal quenching is significantly reduced in a multi-layer SrS:Cu,Ag / SrS:Ce ACTFEL device, compared to that of a single-layer SrS:Cu or SrS:Cu,Ag

ACTFEL device. The operation of SrS:Cu is examined as a function of temperature; the space charge density is found to increase with temperature up to ~ 250 K with an activation energy of 0.02 eV. The space charge density in SrS:Cu ACTFEL devices is estimated as $\sim 1.8 \times 10^{16}$, which yields estimates of the cathode phosphor field and the interfacial trap depth of ~ 1.3 MV/cm and ~ 0.73 eV, respectively.

©Copyright by Beau Baukol

May 17, 2001

All rights reserved

Alternating-Current Thin-Film Electroluminescent Device Fabrication and
Characterization

by

Beau Baukol

A DISSERTATION

submitted to

Oregon State University

in partial fulfillment of
the requirements for the
degree of

Doctor of Philosophy


Completed May 17, 2001
Commencement June 2002

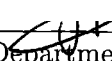
Doctor of Philosophy dissertation of Beau Baukol presented on May 17, 2001

APPROVED:

 Redacted for privacy 

Major Professor, representing Physics



Redacted for privacy 

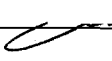
_____
Chair of the Department of Physics

 Redacted for privacy

Dean of the Graduate School

I understand that my dissertation will become part of the permanent collection of Oregon State University libraries. My signature below authorizes release of my dissertation to any reader upon request.

 Redacted for privacy 

_____
Beau Baukol, Author

ACKNOWLEDGMENT

The completion of this thesis and the research upon which it is based was made possible by a number of individuals and organizations who have greatly assisted this effort. This section intends to acknowledge the efforts of these people who have aided me throughout this process.

I would like to thank Sey-Shing Sun of Planar America, Inc., for his commendable support of this research by providing technical advice, SrS:Cu devices for characterization, and substrates for ACTFEL device fabrication. I would also like to thank Richard Tuenge of Planar America and Stephanie Moehnke, formerly of Planar America, for providing undoped ALE SrS films for use in this project. I am also indebted to Markku Leskela and Jarkko Ihannus for their effort to supply ALE CaS films.

There are several former and current members and affiliates of the electroluminescence research group at here Oregon State University. To begin with, I would like to thank Dane Vinson for introducing me to the various methods of electrical characterization of ACTFEL devices. Insurmountable amounts of gratitude are owed to Dr. Paul Keir for indoctrinating me into the field of ACTFEL device processing and bestowing upon me knowledge about the e-beam evaporator and its nuances, and the RTA, PECVD, rf sputtering and thermal evaporation systems. This thesis would certainly have taken a different course without his guidance. In addition, I owe thanks to Drs. Paul Keir and John Hitt for their inspiring, unbridled work ethic and passion for jousting. I would also like to express my gratitude to them for writing the Visual Basic code for the characterization programs, and to Jeff Bender for completing the upgrade of the programs to the new OS. These tedious tasks have made this work much less difficult and more enjoyable. I have also received a great deal of help from Ben Clark in the OSU Chemistry department. I am deeply grateful for his willingness to supply sulfide material for thin-film deposition efforts and for assisting

the growth of my understanding of phosphor materials. Chris Tasker has been an enormous help with maintaining the equipment in the clean room, for which I am very grateful. I am also indebted to Brad Cleary and Corey Nevers for introducing me to the temperature control systems and optical equipment in our characterization lab. Finally, I would like to thank "The Bossman," Dr. John F. Wager, for providing funding and industry contacts, for stimulating ideas about ACTFEL devices, and for providing entertaining kindling to stoke the political deliberation that frequently accompanied our group's pitchers of ale.

Also, I would like to thank my parents, Bard and Nicki Baukol, for their support and encouragement, and my wife Jennifer for her patience, support, understanding, and for enduring through all the years of my education.

This work was supported by the Defense Advanced Research Projects Agency through the Phosphor Technology Center of Excellence, Grant No. MDA 972-93-1-0030, and by the National Science Foundation under Contract No. DMR-0071899.

TABLE OF CONTENTS

	<u>Page</u>
1. INTRODUCTION	1
2. OPERATION AND CHARACTERIZATION OF ACTFEL DEVICES ...	4
2.1 ACTFEL device fundamentals	4
2.1.1 Device structure	4
2.1.2 ACTFEL device operation	5
2.2 Optical characterization.....	11
2.2.1 Luminance-voltage characterization	12
2.2.2 Efficiency-voltage characterization.....	13
2.2.3 Electroluminescence emission spectrum and color coordinates	15
2.2.4 Transient brightness analysis	18
2.3 Electrical characterization.....	20
2.3.1 Experimental Setup.....	20
2.3.2 Charge-voltage characterization	21
2.3.3 Capacitance-voltage characterization	24
2.3.4 Internal charge-phosphor field characterization	26
2.3.5 Maximum charge-maximum voltage characterization.....	27
2.4 Conclusion.....	30
3. ACTFEL MATERIALS AND LUMINESCENT IMPURITY ISSUES	31
3.1 ACTFEL device materials	31
3.1.1 The phosphor layer	31
3.1.2 Insulator layers for ACTFEL devices	36
3.1.3 Transparent contacts.....	38
3.1.4 Opaque contacts	39
3.1.5 Substrates	39
3.2 Thin-film processing.....	39
3.2.1 Evaporation	40
3.2.2 Sputter deposition	41
3.2.3 Chemical vapor deposition	42
3.2.4 Atomic layer epitaxy.....	43

TABLE OF CONTENTS (Continued)

	<u>Page</u>
3.2.5 Post-deposition annealing	45
3.3 Luminescent impurities	47
3.3.1 Mn^{2+}	48
3.3.2 Ce^{3+}	48
3.3.3 Cu^{+}	50
3.3.4 Eu^{2+}	57
3.4 Conclusion	57
4. ACTFEL PHOSPHOR FABRICATION	59
4.1 Source layer diffusion doping of ALE thin-film phosphors	59
4.1.1 Cu doping of ALE SrS	61
4.1.2 $CeCl_3$ doping of ALE SrS	77
4.1.3 Eu doping of ALE SrS and CaS	79
4.2 $Sr_xCa_{1-x}S:Eu,(Cu)$	84
4.3 $(Ba,Zn)S:Mn$	89
4.4 Conclusions	90
5. ACTFEL DEVICE CHARACTERIZATION	92
5.1 EL thermal quenching	92
5.1.1 $ZnS:Mn$	93
5.1.2 $SrS:Ce$	96
5.1.3 $SrS:Cu$	98
5.1.4 $SrS:Cu,Ag$ with $SrS:Ce$ interface layers	105
5.1.5 Summary	109
5.2 Spectral shift with temperature of $SrS:Cu$ ACTFEL devices	111
5.3 Space charge in $SrS:Cu$ ACTFEL devices	113
5.3.1 Temperature dependence of space charge density in $SrS:Cu$ ACTFEL devices	114
5.3.2 Effect of Na coactivation on space charge density in $SrS:Cu$ ACTFEL devices	120

TABLE OF CONTENTS (Continued)

	<u>Page</u>
6. CONCLUSIONS AND RECOMMENDATIONS FOR FUTURE WORK .	124
6.1 Conclusions	124
6.2 Recommendations for future work	125
6.2.1 Recommendations for future ACTFEL fabrication	125
6.2.2 Recommendations for future ACTFEL characterization	127
BIBLIOGRAPHY	130

LIST OF FIGURES

<u>Figure</u>	<u>Page</u>
2.1 The standard ACTFEL device structure.....	5
2.2 An energy band diagram of an ideal ACTFEL device under applied voltage, illustrating the primary physical properties involved in its operation.	8
2.3 An energy band diagram of an ACTFEL device containing positive space charge in the phosphor under applied voltage, illustrating band bending.....	10
2.4 An energy band diagram of an ACTFEL device illustrating space charge creation by (1) band-to-band impact ionization and hole trapping, (2) trap-to-band impact ionization, and (3) field emission.	11
2.5 A luminance-voltage (L-V) curve for an ALE ZnS:Mn ACTFEL device driven by a 60 Hz bipolar trapezoidal waveform.....	13
2.6 An efficiency-voltage (η -V) curve for an ALE ZnS:Mn ACTFEL device driven by a 60 Hz bipolar trapezoidal waveform.....	14
2.7 Electroluminescence spectra displaying band emission (SrS:Eu ²⁺) and line emission (BaS:Eu ³⁺).	16
2.8 The 1931 CIE chromaticity diagram.....	18
2.9 Transient brightness curve for a sputtered SrS:Cu ACTFEL device...	19
2.10 ACTFEL electrical characterization setup.	21
2.11 The bipolar trapezoidal waveform.	22
2.12 A Q-V curve for an evaporated ZnS:Mn ACTFEL device.	23
2.13 C-V curves for an evaporated ZnS:Mn ACTFEL device taken at 20, 40, and 60 V above threshold. The arrow indicates the direction of increasing voltage.....	26
2.14 A Q-F _p curve for an evaporated ZnS:Mn ACTFEL device.	28
2.15 A Q _{max} ^e -V _{max} curve for an ALE ZnS:Mn ACTFEL device.	29
2.16 A $\frac{dQ_{max}^e}{dV_{max}}$ -V _{max} curve for an ALE ZnS:Mn ACTFEL device.....	30
3.1 A depiction of the sputtering process.	42
3.2 Atomic layer deposition of one monolayer of ZnS.	45

LIST OF FIGURES (Continued)

<u>Figure</u>	<u>Page</u>
3.3 Cu ⁺ energy levels in an alkali halide host. Shown, from right to left, are: free-ion levels, the energy shift due to the crystal-field, Jahn-Teller distortion, and spin-orbit splitting of the lowest level (emitting states). (not to scale)	50
3.4 Electroluminescence spectra of SrS:Cu,Ag,Cl; SrS:Cu,Cl; and SrS:Cu,Na ACTFEL devices.	55
3.5 Eu ²⁺ energy level diagram showing energy level splitting as a function of crystal field strength.	58
4.1 Depiction of the source layer diffusion doping (SLDD) process for dopant incorporation into an ALE ACTFEL phosphor host film.	60
4.2 Electroluminescence emission spectrum for an ALE SrS film doped with Cu ₂ S via source layer diffusion doping.	62
4.3 L-V and η -V curves for a 650 nm thick ALE SrS ACTFEL device doped with 1.2% Cu ₂ S and 1.5% NaF via source layer diffusion doping.	66
4.4 EL emission spectra for a 1000 nm ALE/SLDD SrS:Cu,Cl ACTFEL device prepared using a CuCl ₂ concentration of 0.75%.	67
4.5 L-V and η -V curves for a 1000 nm thick ALE SrS ACTFEL device doped with 0.75% CuCl ₂ via source layer diffusion doping.	67
4.6 L-V and η -V curves for a 1000 nm thick ALE SrS ACTFEL device doped with 0.15%, 0.75%, and 1.5% CuCl ₂ via source layer diffusion doping.	68
4.7 Electroluminescence emission spectrum for an ALE SrS ACTFEL device doped with CuCl ₂ and AgCl via source layer diffusion doping.	71
4.8 Internal charge - phosphor field curves for ALE SrS ACTFEL devices doped with CuCl ₂ and AgCl via source layer diffusion doping.	72
4.9 Q_{max} - V_{max} curves for ALE SrS ACTFEL devices doped with CuCl ₂ and AgCl via source layer diffusion doping.	72
4.10 L-V and η -V curves for an ALE SrS ACTFEL device doped with CuCl ₂ , and GaF ₃ via source layer diffusion doping.	73
4.11 L-V and η -V curves for an ALE SrS ACTFEL device doped with CuCl ₂ , AgCl, and GaF ₃ via source layer diffusion doping.	74

LIST OF FIGURES (Continued)

<u>Figure</u>	<u>Page</u>
4.12 EL emission spectrum for an ALE SrS ACTFEL device doped with CuCl ₂ , AgCl, and GaF ₃ via source layer diffusion doping.	75
4.13 Q_{max} - V_{max} curves for ALE/SLDD SrS:CuCl ₂ ACTFEL device with and without GaF ₃	77
4.14 Electroluminescence emission spectrum for an ALE SrS film doped with CeCl ₃ and NaF via source layer diffusion doping.	78
4.15 L-V and η -V curves for an ALE SrS film doped with CeCl ₃ and NaF via source layer diffusion doping.	79
4.16 Electroluminescence emission spectra of ALE SrS:Eu and CaS:Eu ACTFEL devices.	81
4.17 L-V and η -V curves obtained at a frequency of 60 Hz for an ALE SrS:Eu ACTFEL device.	82
4.18 Q - F_p curves for ALE SrS:Eu and CaS:Eu ACTFEL devices taken at 40 V above the threshold voltage.	82
4.19 Transient brightness curves for ALE SrS:Eu ACTFEL devices taken at 40 V above the threshold voltage. Curves for both positive and negative pulse polarities are shown.	83
4.20 Transient brightness curves for ALE CaS:Eu ACTFEL devices taken at 40 V above the threshold voltage. Curves for both positive and negative pulse polarities are shown.	84
4.21 EL emission spectra of Sr _x Ca _{1-x} S:Eu ACTFEL devices for x=0, 0.2, 0.4, 0.7 and 1 (the arrow indicates decreasing x).	86
4.22 L-V curves of Sr _{0.5} Ca _{0.5} S:Eu,Cl ACTFEL devices with and without Cu co-activation.	88
4.23 η -V curves of Sr _{0.5} Ca _{0.5} S:Eu,Cl ACTFEL devices with and without Cu co-activation.	88
4.24 EL emission spectra of ZnS:Mn and Ba _{0.875} Zn _{0.125} S:Mn, with the CIE coordinates given in parentheses.	91
5.1 L-V and η -V curve comparison for an evaporated ZnS:Mn ACTFEL device at 25°C and 50°C.	94

LIST OF FIGURES (Continued)

<u>Figure</u>	<u>Page</u>
5.2 L-V and η -V curve comparison for an ALE ZnS:Mn ACTFEL device at 25°C and 50°C.....	95
5.3 Q_{max} - V_{max} curves for an ALE ZnS:Mn ACTFEL device at 25°C and 50°C.	96
5.4 Q- F_p curves (at ~ 40 V above V_{th}) for an ALE ZnS:Mn ACTFEL device at 25°C and 50°C.	97
5.5 L-V and η -V curves for an ALE SrS:Ce ACTFEL device at 25°C and 50°C.	98
5.6 L-V curves for a sputtered SrS:Cu ACTFEL device at -40, 20, and 80°C (arrow indicates increasing temperature).....	99
5.7 A configurational coordinate diagram of a luminescent center.	100
5.8 L-V and η -V curves for a sputtered SrS:Cu,Ag ACTFEL device at 25°C and 50°C.	101
5.9 Q_{max} - V_{max} and transferred charge capacitance curves for a sputtered SrS:Cu,Ag ACTFEL device at 25°C and 50°C.	102
5.10 Q-V curves for a sputtered SrS:Cu,Ag ACTFEL device at 25°C and 50°C.	104
5.11 Q- F_p curves for a sputtered SrS:Cu,Ag ACTFEL device at 25°C and 50°C.	104
5.12 Luminance-voltage and efficiency-voltage curves for a sputtered SrS:Cu,Ag ACTFEL device containing SrS:Ce interface layers at 25°C and 50°C.	105
5.13 Q_{max} - V_{max} and transferred charge capacitance curves for a sputtered SrS:Cu,Ag ACTFEL device containing SrS:Ce interface layers at 25°C and 50°C.....	106
5.14 Q-V curves for a sputtered SrS:Cu,Ag ACTFEL device containing SrS:Ce interface layers at 25°C and 50°C.	107
5.15 Q- F_p curves for a sputtered SrS:Cu,Ag ACTFEL device containing SrS:Ce interface layers at 25°C and 50°C.	108
5.16 Electroluminescence emission spectra of a sputtered SrS:Cu,Ag ACTFEL device with and without SrS:Ce interface layers.	109

LIST OF FIGURES (Continued)

<u>Figure</u>	<u>Page</u>
5.17 Electroluminescence emission spectra of a sputtered SrS:Cu,Ag ACTFEL device with SrS:Ce interface layers at 25 and 50°C.	110
5.18 EL spectra for a sputtered SrS:Cu ACTFEL device at temperatures of 30, 100, 175, 250, and 325 K (arrow indicates increasing temperature).	112
5.19 EL spectra for a sputtered SrS:Cu,Ag ACTFEL device at temperatures of 30, 100, 175, 250, and 325 K (arrow indicates increasing temperature).	113
5.20 Q_{max} - V_{max} curves for a sputtered SrS:Cu,Ga ACTFEL device at 25 and 50°C.	115
5.21 Q_{max} - V_{max} curves for a sputtered SrS:Cu ACTFEL device at temperatures of 50, 100, 200, 250, and 300 K (arrow indicates increasing temperature).	119
5.22 Arrhenius plot of space charge density estimate.	121
5.23 Q_{max} - V_{max} curve comparison of a SrS:Cu,F ACTFEL device with and without NaF fluxing.	122

LIST OF TABLES

<u>Table</u>	<u>Page</u>
3.1 Properties of phosphor host materials used in ACTFEL devices.	34
3.2 Properties of luminescent impurities.	35
3.3 Target luminance, efficiency, and CIE coordinates (60 Hz) for a high-luminance full-color ACTFEL display.	36
3.4 Properties of dielectric materials commonly used as ACTFEL insulators.	37
4.1 The effect of Cl containing co-activators on the EL properties of SrS:Cu prepared by the ALE/SLD process.	64
4.2 The effect of Cu concentration on the operation properties of SrS:Cu,Na ACTFEL devices prepared by the ALE/SLDD process with a 650 nm thick phosphor and NaF layers with thickness $\sim 1.5\%$ of the phosphor thickness.	65
4.3 The effect of CuCl_2 concentration on the operation properties of SrS:Cu,Cl ACTFEL devices prepared by the ALE/SLDD process with a 1000 nm thick phosphor.	68
4.4 The effect of CuCl_2 and AgCl concentration on the emission properties of SrS:Cu,Ag,Cl ACTFEL devices prepared by the ALE/SLDD process.	70
4.5 The EL emission characteristics of ~ 1000 nm ALE/SLDD SrS:Cu,Cl and SrS:Cu,Ag,Cl ACTFEL devices with and without GaF_3	76
4.6 EL emission from $\text{Sr}_x\text{Ca}_{1-x}\text{S:Eu}$ ACTFEL devices as a function of x.	87
4.7 EL emission from (Ba,Zn)S:Mn ACTFEL devices of varying Ba:Zn ratios.	90
5.1 Summary of electroluminescence thermal quenching properties for several types of ACTFEL device. Values represent differences between measurements at 25°C and 50°C	111
5.2 Estimated threshold voltage values and space charge density estimates for a 1100 nm sputtered SrS:Cu,Ga ACTFEL device at 25° and 50°	116

LIST OF TABLES (Continued)

<u>Table</u>	<u>Page</u>
5.3 Estimated cathode field values for a 1100 nm sputtered SrS:Cu,Ga ACTFEL device at 25 and 50°C, along with experimentally determined average phosphor field and space charge density.....	117
5.4 Phosphor space charge density and threshold voltage estimates at various temperatures for an 1100 nm sputtered SrS:Cu,Ga ACTFEL device.	120

ALTERNATING-CURRENT THIN-FILM ELECTROLUMINESCENT DEVICE FABRICATION AND CHARACTERIZATION

1. INTRODUCTION

An introduction to alternating-current thin-film electroluminescent (ACTFEL) device technology begins with the discovery of the category of materials that luminesce, known as phosphors. Luminescence is the non-thermal conversion of energy from some excitation source into light. The phenomenon of luminescence is observable in many forms, such as bioluminescence from the biochemical reactions of luciferin in fireflies, triboluminescence from the mechanical energy imparted while crushing sugar, and cathodoluminescence occurring in an operating television. The earliest man-made luminescent material is thought to have been synthesized by ancient Romans, who formed calcium sulfide phosphors as early as 186 B.C. by heating sulfur with chalk, lime, or oyster shells. [1] A more recent synthesis was carried out by the Italian shoemaker and alchemist Vincenzo Cascariolo, who in 1603 ground barium sulfate and then heated it with coal ($\text{BaSO}_4 + 2\text{C} \rightarrow \text{BaS} + 2\text{CO}_2$). The material was noticed to produce blue light at night which could be replenished upon exposure to sunlight, and the material was named *lapis solaris* (sun stone). [2] Some consider this discovery to be the origin of inorganic phosphors. Later phosphor developments occur in 1768 when Canton obtained CaS and then in 1866 when Sidot formed the first ZnS, green emitting, luminescent material. An understanding of the luminescence from these materials began in 1886 when Verneuil proved that pure CaS did not luminesce, and that a trace of Bi was necessary for light emission. Later it was found that a trace of Cu was necessary for emission from green ZnS.

Electroluminescence (EL) is the conversion of electric energy into light by subjecting a phosphor to an electric field. High-field EL was first discovered by Destriau in 1936. [3] Destriau observed light emission after applying a high AC voltage to a

thin layer of fine Cu doped ZnS powder particles suspended in castor oil. Practical high-field AC-EL devices in the form of powder lamps were later developed by Sylvania after the emergence of the transparent conductor ITO in the early 1950's. The development of powder AC-EL gave way to thin-film EL technology after Vlasenko and Popkov showed brighter luminance from thin-film ZnS doped with Mn. [4] Thin-film electroluminescence suffered stability problems until 1974 when Inoguchi *et al.* reported a TFEL ZnS:Mn device sandwiched between two insulators which showed high luminance and a long operating life under an applied AC voltage. [5] ACTFEL technology has since matured with the commercialization of monochrome flat panel displays in the early 1980's and the development of multi-color displays in the 90's.

The primary application of ACTFEL technology is as a thin display in the flat-panel display (FPD) industry, which is driven by the demand for portable displays. The leading FPD technology is the liquid-crystal display (LCD), found in a number of applications, such as watches, calculators, laptop computer monitors, and hand-held electronic devices. The LCD display is expanding into the desktop monitor market, replacing cathode-ray tube (CRT) technology. Other FPD technologies are the plasma display panel and the field-emission display (FED). The advantages of ACTFEL displays over LCDs are full-viewing angle, performance over a wider temperature range, sufficient ruggedness, and the ability to pattern smaller pixels. ACTFEL displays are inferior to LCDs in that they suffer greater power consumption, lack adequate chromaticity, and require much larger driving voltages. The strong interaction of "hot" electrons with lattice phonons and crystal imperfections renders high-field EL an inefficient process, making it naturally more difficult to find sufficiently efficient phosphor materials for ACTFEL devices that emit in the primary colors. The best known ACTFEL phosphor to date is the yellow emitting ZnS:Mn, which can be filtered to give bright red and green emission. SrS:Cu has emerged as a sufficiently bright blue phosphor, which should lead to improved full-color ACTFEL displays in the near future. Despite recent progress in the development of full-color

ACTFEL displays, there remains room to improve the brightness and efficiency of all three primary colors in ACTFEL displays. The luminescence mechanisms of SrS:Cu ACTFEL phosphors are also poorly understood. Thus the aim of this thesis is to provide better understanding and to improve the overall performance of primary color ACTFEL phosphors.

The outline of this dissertation is as follows. Chapter 2 introduces the ACTFEL device and reviews basic device physics and standard characterization techniques. Important materials properties relevant to ACTFEL devices and their deposition techniques are investigated in Chapter 3. Chapter 4 presents results obtained from fabrication of ACTFEL devices in an effort to improve phosphor performance. An investigation of ACTFEL device operation and electrical characteristics is featured in Chapter 5. Finally, Chapter 6 presents conclusions and recommendations for future work.

2. OPERATION AND CHARACTERIZATION OF ACTFEL DEVICES

This chapter is an overview of fundamental concepts of ACTFEL device operation and characterization. The ACTFEL device structure and an operation model are presented first, followed by a description of standard optical and electrical characterization methods.

2.1 ACTFEL device fundamentals

2.1.1 Device structure

An ACTFEL device has the structure of a metal-insulator-semiconductor - insulator-metal (MISIM) thin-film stack. The standard ACTFEL device structure, shown in Fig. 2.1, employs a transparent substrate, typically glass, coated with a transparent conducting layer, which serves as the bottom electrode. The bottom insulator, phosphor, and top insulator layers reside between the bottom transparent conductor and a top conducting layer, which is opaque. The top conducting layer serves both as an electrical contact and as a reflector to direct light generated in the phosphor layer out through the glass substrate. The standard structure is the most prominently used structure by ACTFEL researchers. It is also used in manufacturing.

It is not uncommon to encounter ACTFEL devices with other structures, one of which is the inverted structure. The inverted structure is similar to the standard structure in that both contain the same insulator-phosphor-insulator sandwich, but the inverted structure is built on an opaque substrate, rather than a transparent substrate. Light cannot be viewed through the substrate of an inverted device; therefore, a transparent top contact must be employed. The inverted structure makes it possible to use higher processing temperatures than the standard structure, since a substrate with a melting point higher than that of glass can be used. The inverted structure

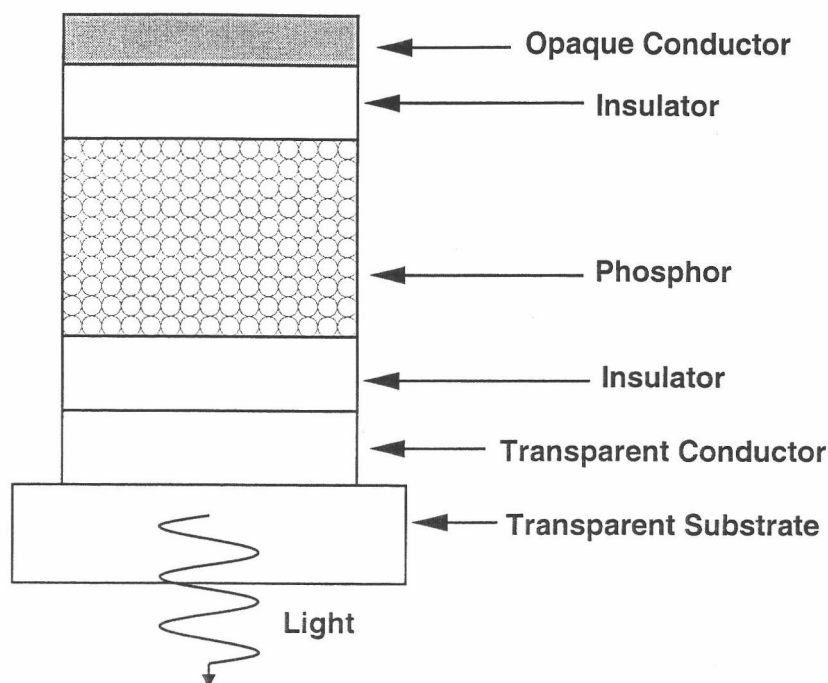


Figure 2.1: The standard ACTFEL device structure.

also allows the use of high dielectric constant materials, which then serve both as the substrate and the bottom insulator.

Another variation of the ACTFEL device structure is the single insulator structure. In this structure, the top insulator is not deposited in order to simplify processing. This can cause reduced device lifetime because the lack of a top insulator exposes the phosphor layer to the atmosphere. For this reason, the single insulator structure is used almost exclusively for research purposes where a quick assessment of a device is all that is desired.

2.1.2 ACTFEL device operation

The generation of light in an electroluminescent device is achieved by transferring energy from charge carriers to luminescent centers in the phosphor. This requires that there are charge carriers in the phosphor and that those carriers have sufficient energy to excite the luminescent impurity to an excited state. The phosphor layer in

an ACTFEL device is in series with at least one insulator, so light generation cannot be induced by a direct current flow through the phosphor layer.

In an ACTFEL device, light emission is produced when some type of alternating-current (AC) voltage waveform is applied to the electrically conducting layers of the thin-film stack. [6] In the basic model, the conduction of charge carriers in the phosphor layer of an ACTFEL device is usually assumed to originate from tunneling of electrons from insulator-phosphor interface states. [7, 8, 9, 10] The energy depth of the states necessitates a high electric field be present at the phosphor-insulator interface for injection to occur. This field also serves to accelerate the carriers to energies sufficient to excite the dopant in the phosphor.

Upon application of an AC voltage waveform to the electrical contacts of an ACTFEL device, an electric field is set up in the phosphor layer. In an ideal device, the field is constant throughout the phosphor layer. If the field in the phosphor is insufficient for injection of charge carriers from interface states, the phosphor layer behaves like a dielectric and the device behaves like a capacitor with a capacitance equal to the capacitance of the phosphor and insulator layers in series,

$$C_{tot} = \frac{C_{ins}C_{ph}}{C_{ins} + C_{ph}}. \quad (2.1)$$

The field in the phosphor layer is then given by

$$f_p = \frac{C_{ins}}{C_{ins} + C_{ph}} \frac{V_{applied}}{t_{ph}}, \quad (2.2)$$

where $V_{applied}$ is the voltage applied to the device and t_{ph} is the thickness of the phosphor layer. The applied voltage at which injection occurs and the purely capacitive behavior of the phosphor layer is no longer present is the threshold voltage, V_{th} . When a voltage is applied across the device with a magnitude greater than V_{th} , charge is transferred across the phosphor layer and light emission is observed, if the carriers excite luminescent impurities.

There are two regimes of operation when the applied AC voltage has a magnitude greater than the threshold voltage in an ideal ACTFEL device. When the applied

voltage is below the turn-on voltage, the device behaves as a capacitor as described above. Above the turn-on voltage, the following processes occur in the phosphor layer of the device, as illustrated in Fig. 2.2. [11] Above the turn-on voltage, the phosphor field at the phosphor/insulator interface on the cathodic side of the device is large enough that electrons trapped in interface states or bulk traps are tunnel emitted into the phosphor conduction band, as illustrated by process 1 in the energy band diagram representation shown in Fig. 2.2. The injected electrons gain kinetic energy from the electric field and drift across the phosphor layer (process 2 in Fig. 2.2). As electrons transit across the phosphor, collisions with the host lattice atoms and the impurity atoms may occur. After undergoing a collision with an electron, a luminescent impurity could absorb some of the energy and become excited from its ground state to its excited state (process 3 in Fig. 2.2). The luminescent impurity subsequently relaxes back to its ground state, either radiatively by emitting a photon with energy equal to the energy level difference (process 4 in Fig. 2.2), or non-radiatively through phonon emission. Optical device efficiency is maximized when all of the excited impurity centers relax radiatively. After undergoing collisions, electrons continue to be transported across the remainder of the phosphor, gaining energy and possibly undergoing more collisions, until reaching the anodic phosphor/insulator interface, where they are captured in electron traps (process 5 in Fig. 2.2). A plethora of traps exist at the interface due to the disorder of the phosphor/insulator heterojunction. Some of the photons released during the luminescent impurity relaxation outcouple from the device and are observed by the viewer (process 6 in Fig. 2.2).

If the applied voltage waveform is such that there is a delay between the end of one pulse and the beginning of the next, some of the trapped charge is emitted from the interface states and leaks across the phosphor to the opposite interface. The trapped electrons at the anodic interface and the ionized states they left at the cathodic interface create a field in the phosphor, even when there is no applied voltage. The trapped electrons experience this field and some leak back across the phosphor

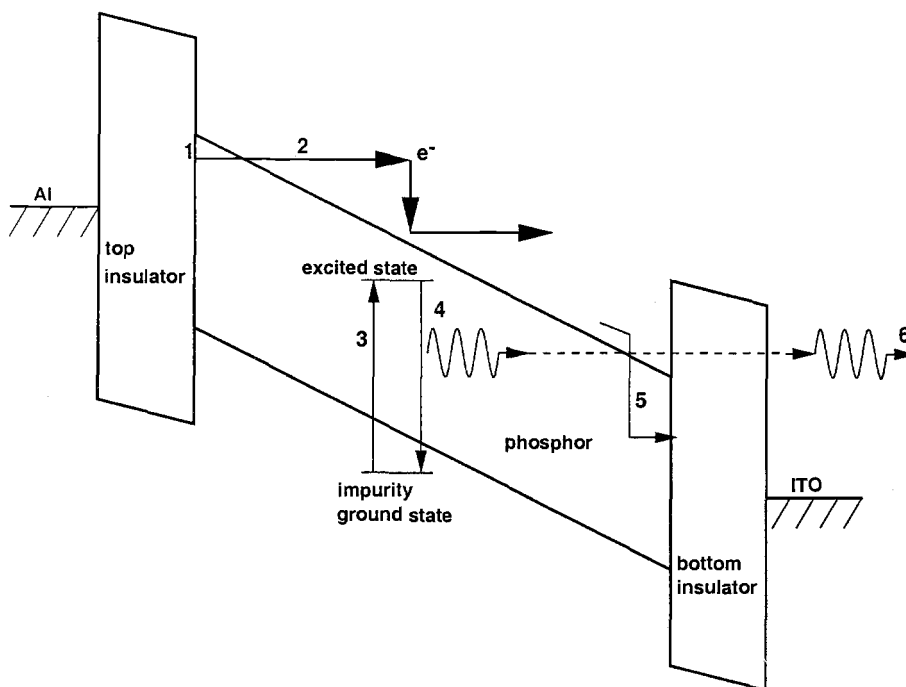


Figure 2.2: An energy band diagram of an ideal ACTFEL device under applied voltage, illustrating the primary physical properties involved in its operation.

if there is no applied voltage to keep them at the interface. When the following pulse of opposite polarity arrives, the process repeats in the opposite direction. The charge remaining at the interfaces affects the phosphor field and modifies the turn-on voltage of the following pulse. As the maximum applied voltage is increased, the amount of charge remaining at the interface, termed polarization charge, is often observed to increase, which lowers the voltage required for injection, termed the turn-on voltage. The biasing electric field is enhanced by the field due to the polarization charge and the two fields combine to generate a phosphor field sufficient for injection. The enhancement of the biasing field has the effect of lowering the voltage at which injection will occur as the applied voltage is increased. The threshold voltage is equal to the turn-on voltage in the limit in which the polarization charge goes to zero.

The simple model described above is acceptable as a basic description of ACTFEL operation; however, actual devices are more complicated. One of the most exten-

sively researched departures from the simple ACTFEL device model is the presence of space charge in the phosphor bulk. A phosphor field dependent on both position and time complicates ACTFEL device operation. The presence of space charge in the phosphor causes a non-uniform electric field profile, as shown in Fig. 2.3. The magnitude of the electric field is depicted in an energy band diagram as the slope of the conduction and valence bands. In the ideal model (Fig. 2.2), where it is assumed that there is no space charge in the phosphor, the slope of the bands, and the electric field, is constant. If space charge exists in the phosphor, there is a field due to this charge, and the bands become bent when this field is represented in the energy band diagram. When the device is biased and space charge is present in the phosphor, the bands are bent so that the field is enhanced near the cathodic side of the device and made weaker on the anodic side. The enhancement of the cathodic field leads to enhanced tunnel injection of electrons from interface states, and allows the tunnel injection to occur at lower voltages than would be necessary without space charge. The weakening of the anodic field results in the excitation of fewer luminescent centers in the phosphor, since the electron distribution will be less energetic in the lower field region. [12] Positive space charge will also have the effect of decreasing insulator degradation due to hot electron bombardment at the anode.

Space charge is created in the phosphor bulk via (1) the trapping of holes generated by band-to-band impact ionization [8, 13, 14, 15], (2) impact ionization of trapped electrons [9, 16, 17, 18, 19], and (3) field emission of trapped electrons to the conduction band, as depicted in Fig. 2.4. [16, 17, 20, 21] The mechanism of space charge generation varies depending on the phosphor host, luminescent impurities, and co-dopants. Space charge in ACTFEL devices is ordinarily assumed to be positive because all of the II-VI wide bandgap semiconductors commonly used for ACTFEL phosphors are typically n-type. [20] Space charge is categorized as static or dynamic, depending on how long it persists in the phosphor. [22, 23] Static space charge refers to charge that exists within the phosphor in a steady-state manner throughout

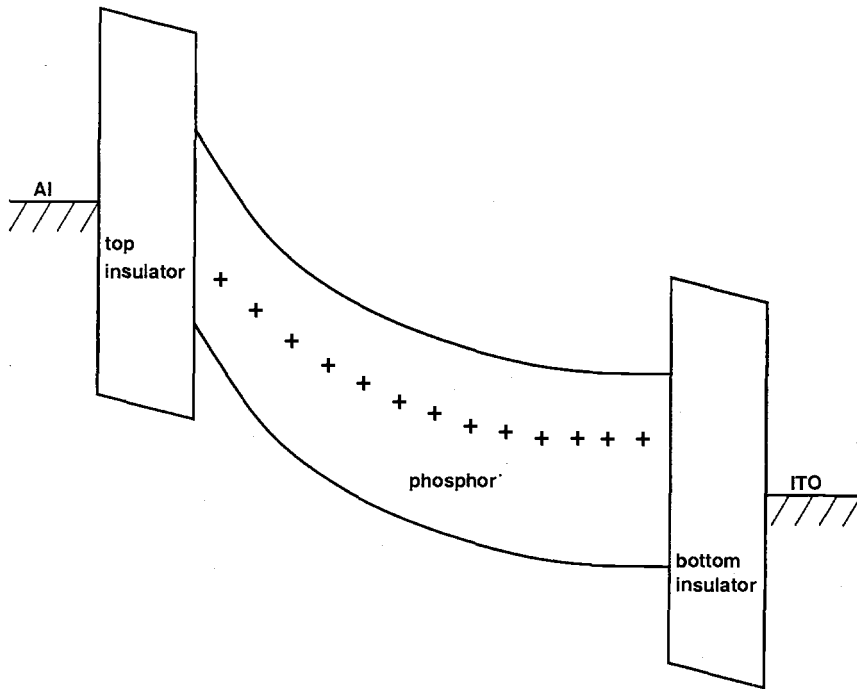


Figure 2.3: An energy band diagram of an ACTFEL device containing positive space charge in the phosphor under applied voltage, illustrating band bending.

device operation. Space charge that is created and annihilated within one period of the applied voltage waveform is referred to as dynamic space charge. If static or dynamic space charge are present in an ACTFEL device, it is evident experimentally in electrical characterization, as described in Sect. 2.3.

Another effect that hinders the understanding of ACTFEL operation is the dependence of the emission rate of electrons into the phosphor on the density of interface states. Emission from the insulator-phosphor interface is dependent on the field in the phosphor layer adjacent to the interface and on the temperature. A higher field is required for electron emission from a deeper state. [17] Measurement of the interface state depth is complicated by the fact that space charge in the phosphor creates a higher field at the cathodic interface where emission occurs. In addition, electron multiplication due to impact ionization in the phosphor causes the measurement of more charge than is actually sourced from the interface states, making it appear that

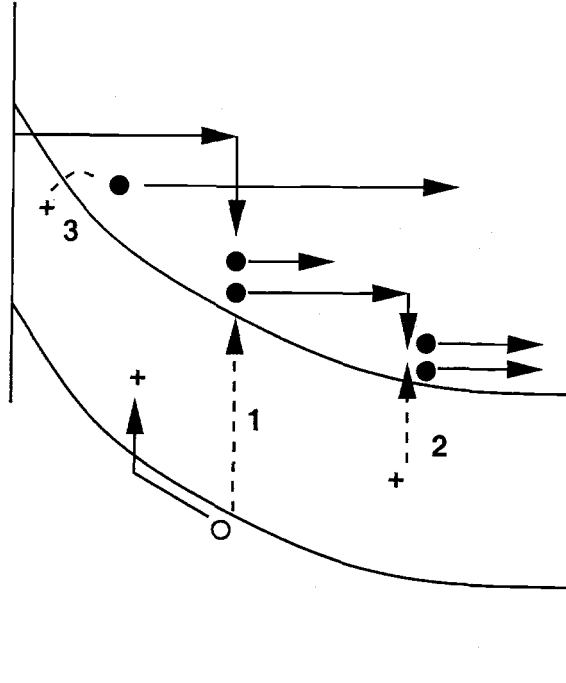


Figure 2.4: An energy band diagram of an ACTFEL device illustrating space charge creation by (1) band-to-band impact ionization and hole trapping, (2) trap-to-band impact ionization, and (3) field emission.

there are more interface states than actually exist. The interface state distribution assumed in the zero-order model does not simultaneously predict experimental leakage charge and turn-on voltage trends. [23, 24]

2.2 Optical characterization

The most important properties of an ACTFEL device are the intensity of the light output, the power required to generate that light, and the color of the light. As a result of this, the most commonly performed characterization experiments measure the luminance, the luminous efficiency, and the color spectrum of an ACTFEL device. These experiments are expounded upon in greater detail in this section.

2.2.1 Luminance-voltage characterization

One measurement required to evaluate the performance of an ACTFEL device is the luminance-voltage (L-V) measurement, also known as the brightness-voltage (B-V) measurement. The L-V measurement is performed by measuring the light output of an ACTFEL device at applied voltages of increasing amplitudes until a predetermined stopping point is reached. The first point is measured by applying a voltage waveform with amplitude below the threshold voltage, allowing the device to reach steady-state, and measuring the luminance with a photometer, photomultiplier tube, or photodiode, in a direction perpendicular to the substrate. The SI unit for luminance is candelas per square meter (cd/m^2), but is also sometimes reported in the English units of footLambert (fL). The amplitude of the voltage waveform is increased and another measurement is taken, and so on until a sufficiently high voltage above threshold is reached. The L-V curve is obtained by plotting luminance on the y-axis and voltage on the x-axis, as shown in Fig. 2.5.

The L-V curve is dependent on several factors, and it is necessary to specify some of them when reporting results. [6] The measured luminance is dependent on the type of driving waveform, the shape of the waveform, and the frequency of the waveform. The fraction of time that the driving waveform spends above the turn-on voltage determines the luminance of the device. Thus, a driving waveform with a higher frequency or a shape such that the time above turn-on is greater will cause a higher luminance. The L-V curve is also dependent on the ambient temperature, the dopant concentration, and the thickness of the phosphor layer. When the temperature is increased, the probability of de-excitation through non-radiative recombination is significantly increased, which leads to reduced light output. Temperature also may affect the threshold voltage in an L-V curve since interface emission and space charge generation mechanisms are dependent on temperature. [17, 25, 26, 27] Luminance increases with luminescent impurity dopant level for low concentrations. Increasing the density of luminescent centers raises the probability of an electron undergoing a

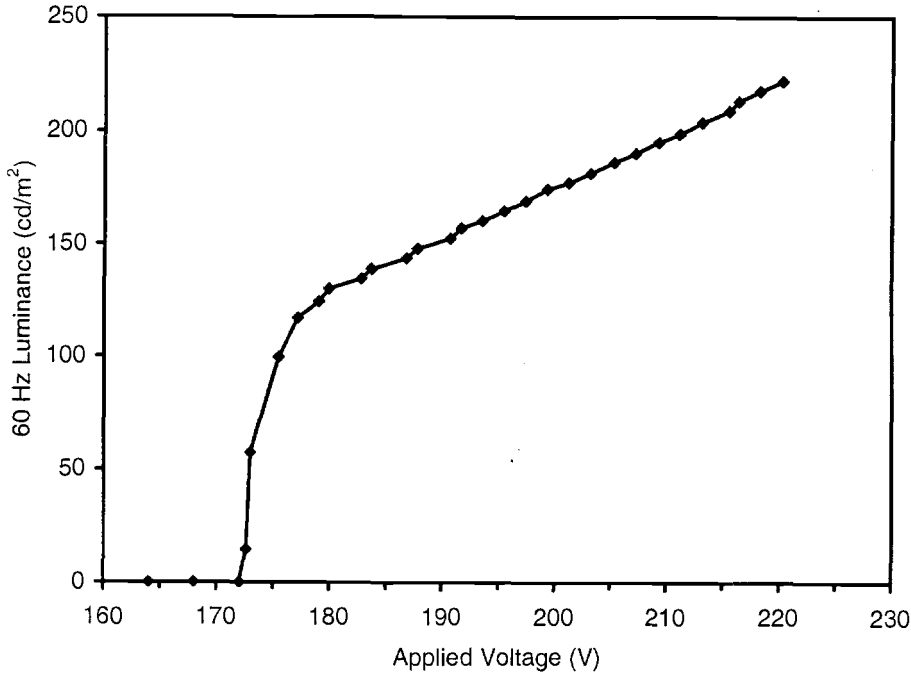


Figure 2.5: A luminance-voltage (L-V) curve for an ALE ZnS:Mn ACTFEL device driven by a 60 Hz bipolar trapezoidal waveform.

collision with a luminescent center. This trend holds as long as the impurity concentration is low enough that phosphor crystallinity is maintained and concentration quenching does not occur. Increasing the phosphor layer thickness also increases the probability of electron impact excitation with an impurity. The threshold voltage is also affected by the phosphor thickness, since a higher voltage is required to achieve the threshold electric field in a thicker device.

2.2.2 Efficiency-voltage characterization

Another ACTFEL characterization procedure of interest is the efficiency-voltage (η -V) measurement. The η -V measurement determines the luminous intensity of an ACTEL device per unit power consumed, or luminous efficiency, η , which has units of lumens per Watt (lm/W). The luminous efficiency is found from

$$\eta = \pi \frac{L}{P}, \quad (2.3)$$

where L is the measured luminance in cd/m^2 and P is the applied power density in W/m^2 . The luminous intensity is found by assuming the luminance is constant in all directions and integrating over all viewable angles. The power density is measured at the same time as the luminance and is found from

$$P = \frac{1}{A\tau} \int_t^{t+\tau} v(t')i(t')dt', \quad (2.4)$$

where A is the device area, τ is the period of the driving waveform, and $v(t)$ and $i(t)$ are the applied voltage and current waveforms, respectively. Figure 2.6 shows an η - V curve for an ALE ZnS:Mn device.

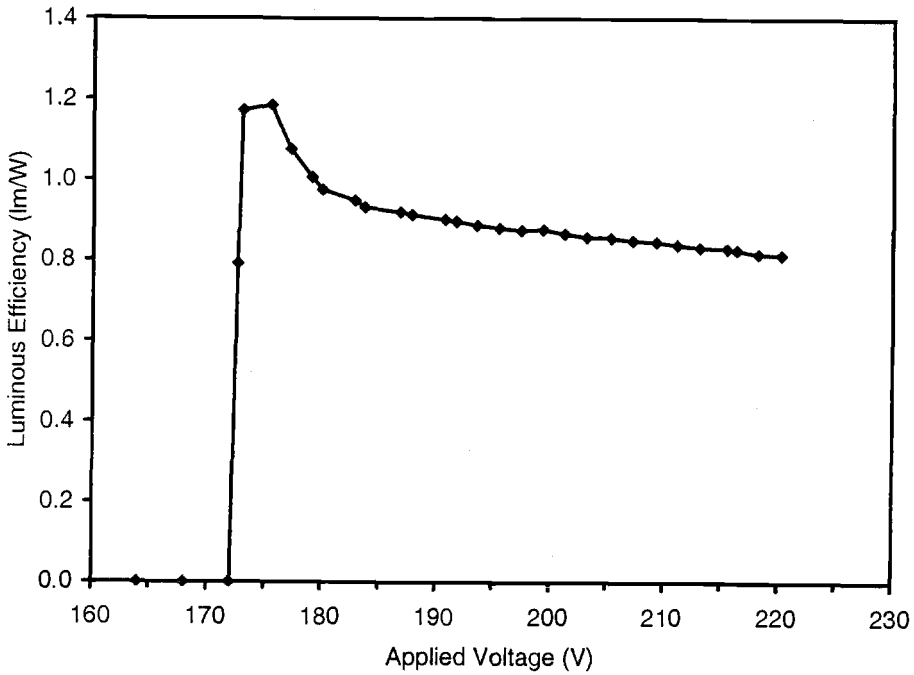


Figure 2.6: An efficiency-voltage (η - V) curve for an ALE ZnS:Mn ACTFEL device driven by a 60 Hz bipolar trapezoidal waveform.

Since the luminous efficiency is dependent on the luminance, it is influenced by most of the same factors. When contemplating the influences on the efficiency, it is useful to consider the interactions an electron may undergo in an ACTFEL device and

the conditions required for the interactions to take place. Once an electron is in the phosphor, in order for electroluminescence to occur, an electron must impact excite a luminescent impurity, so the luminous efficiency is proportional to the excitation efficiency, $\eta_{exc} = \sigma Nd$, where σ is the impact excitation cross section, N the dopant concentration, and d the phosphor layer thickness. This assumes that the field is large enough everywhere in the entire thickness d of the phosphor that the electrons have enough energy to impact excite the luminescent center. This is not the case if there is positive space charge present in the phosphor. The thickness of the active region, where there is a sufficient field for impact excitation, is reduced if space charge is present, which reduces η_{exc} and therefore the luminous efficiency η . [28, 29]

In addition to the luminance, the luminous efficiency also depends on the power input to the ACTFEL device. Thus if a factor that increases the brightness also increases the power consumption, such as the frequency of the driving waveform, then the efficiency is not increased. The change in luminance caused by a change in the driving frequency coincides with an increase in the power consumed, so the luminous efficiency does not increase with frequency. Luminous efficiency is affected in a similar way by the device thickness. Thicker phosphor layers enhance the luminance, but also cause the threshold voltage to increase. This would require a higher operating voltage, which causes the power to increase, as evident from Eq. 2.4.

2.2.3 Electroluminescence emission spectrum and color coordinates

The color of the light emitted from an ACTFEL device is readily apparent to the observer, but the exact nature of the light source is not. Information about the properties of the luminescent center can be extracted by measuring the emission spectrum of the electroluminescence. The emission spectrum and color coordinates are also important from an industrial point of view for assessing the effectiveness of a phosphor for full color ACTFEL displays.

The emission spectrum is created by plotting the intensity of the emission as a function of wavelength. The energy of the transition(s) is then apparent from the value of the wavelength where the emission peaks. Also evident in the emission spectrum is the nature of the energy levels involved in the radiative transition in the luminescent center. For example, the valence of a luminescent Eu ion is readily apparent from the emission spectrum, as demonstrated in Fig. 2.7. The emission from Eu impurities in SrS exhibit broad emission, revealing the $5d \rightarrow 4f$ band emission of divalent Eu, while in BaS the observed $4f \rightarrow 4f$ line emission exposes the charge state of the Eu impurities as trivalent.

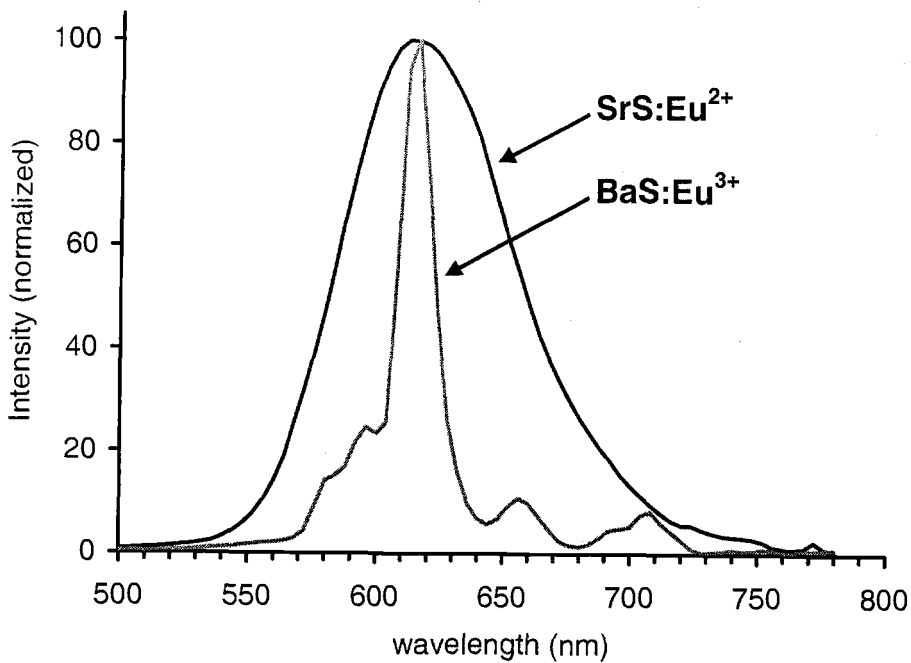


Figure 2.7: Electroluminescence spectra displaying band emission (SrS:Eu^{2+}) and line emission (BaS:Eu^{3+}).

Although the visible color of an ACTFEL device is apparent from the emission spectrum, it is useful to quantify the color of the light in terms of its CIE color

coordinates. The CIE colorimetric system was established by the Commission Internationale de l'Eclairage (CIE) in 1931. CIE color coordinates x and y are determined from the three CIE tristimulus values X , Y , and Z . [30] X , Y , and Z are found by integrating over the visible range of wavelengths the product of the spectrum of the test light source, $P(\lambda)$, with the CIE spectral stimulus functions $x(\lambda)$, $y(\lambda)$, and $z(\lambda)$,

$$X = K \int_{380}^{780} P(\lambda)x(\lambda)d\lambda, \quad (2.5)$$

$$Y = K \int_{380}^{780} P(\lambda)y(\lambda)d\lambda, \quad (2.6)$$

$$Z = K \int_{380}^{780} P(\lambda)z(\lambda)d\lambda \quad (2.7)$$

where

$$K = \frac{1}{P(\lambda)y(\lambda)d\lambda}. \quad (2.8)$$

Then the CIE color coordinates x and y are found from

$$x = \frac{X}{X + Y + Z} \quad (2.9)$$

$$y = \frac{Y}{X + Y + Z}. \quad (2.10)$$

Figure 2.8 shows a depiction of the CIE chromaticity diagram with some color regions designated. The numbers beside the perimeter points correspond to the wavelength of monochromatic light at that coordinate. White light is represented in Fig. 2.8 by the black dot located at the CIE color coordinate $x=0.333$, $y=0.333$. The line drawn between two points on the CIE chromaticity diagram represents the range of colors that can be produced with two light sources emitting light with those coordinates, referred to as the color gamut of the two sources. [31] The colors enclosed by a triangle formed from three light sources' color coordinates make up the color gamut of those three sources. [32] This makes it possible to evaluate the chromaticity available from a full-color ACTFEL display utilizing the device or devices under study.

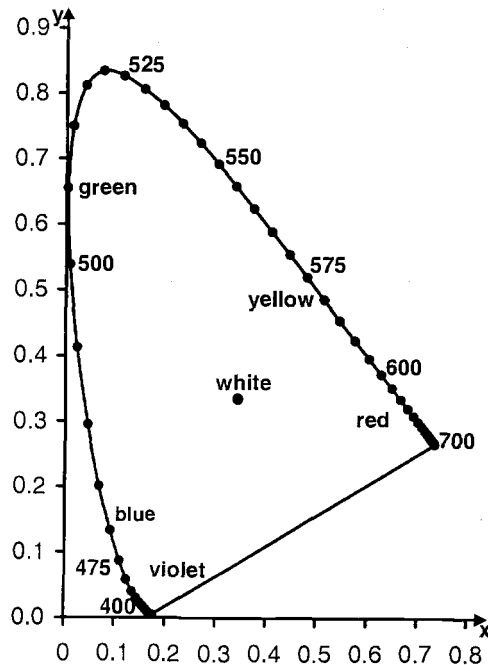


Figure 2.8: The 1931 CIE chromaticity diagram.

2.2.4 Transient brightness analysis

A less common optical ACTFEL characterization experiment is the transient brightness, or $b(t)$, measurement. In a $b(t)$ measurement, the optical output of an ACTFEL device is measured as the output current of a photomultiplier tube over the duration of an applied voltage pulse. In a $b(t)$ measurement, photon emission is observed as a function of time, so that it can be correlated with the applied voltage waveform, which yields information about various aspects of the operation of an ACTFEL device.

A $b(t)$ curve for a SrS:Cu ACTFEL device is shown in Fig. 2.9. The two peaks observed in Fig. 2.9 are identified with the corresponding portion of the applied voltage waveform, $v_a(t)$. The first peak in the transient brightness curve is termed leading edge (LE) luminescence, while the peak at the end of the applied voltage pulse is known as trailing edge (TE) luminescence. LE luminescence is due to the radiative decay process back to the ground state of luminescent centers excited by

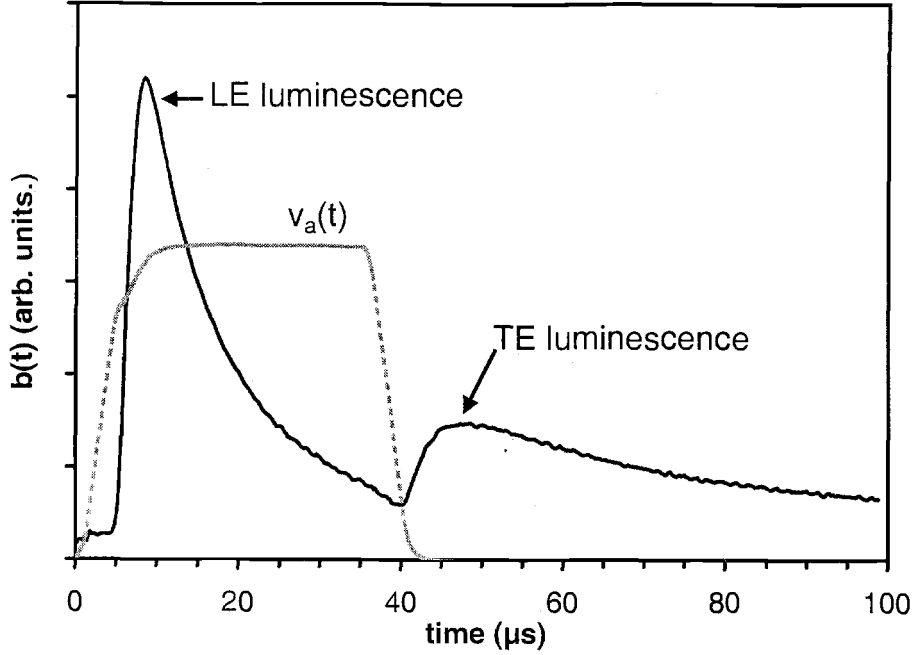


Figure 2.9: Transient brightness curve for a sputtered SrS:Cu ACTFEL device.

impact excitation with electrons as they transit the phosphor after being emitted from the cathodic phosphor/insulator interface. Some of the electrons in the excited state do not decay to the ground state but instead are further excited to the conduction band by the high electric field. These electrons, as well as the electrons injected from the cathodic phosphor/insulator interface, are swept to the anodic interface where they accumulate in traps at the phosphor/insulator interface. As the magnitude of the applied voltage is reduced, these electrons drift back across the phosphor toward the cathodic interface by an internal electric field. Radiative recombination of these electrons with the ionized luminescent centers are observed as TE emission. [33] TE emission is observed in CaS and SrS doped with Eu^{2+} , Ce^{3+} , and Cu^+ , where the ground state and first excited state of the luminescent ion lie within the band gap of the host. [28, 33, 34, 35, 36, 37, 38, 39, 40, 41] TE emission is not typically seen in ZnS:Mn ACTFEL devices, although it has been reported in thick dielectric EL devices [42] and in devices grown by ALE using ZnCl_2 as a precursor, [43] but via

a different mechanism than described here. The existence of TE luminescence in a device reveals that there are ionized impurities (i.e. positive space charge) within the phosphor bulk. Researchers have found that ACTFEL device performance can be improved through the enhancement of TE emission using a multi-layered phosphor. [44]

2.3 Electrical characterization

Measuring the optical output of an ACTFEL device is useful for evaluating its potential as a display product, but does not provide adequate information regarding the physics of device operation. More insight into the physics of ACTFEL operation is gained with the use of various electrical characterization techniques. This section describes electrical characterization techniques commonly used to investigate the physics of ACTFEL devices.

2.3.1 Experimental Setup

The electrical characterization circuit and attached measurement components comprising the experimental setup are shown in Fig. 2.10. An arbitrary waveform generator is used to produce the driving voltage waveform. The waveform is amplified by a high voltage amplifier consisting of two Apex model PA-85 op-amps and a switching network. The output of the amplifier drives the series combination of a protection resistor, the ACTFEL device, and a sense capacitor. The circuit used in this setup is known as a Sawyer-Tower circuit. [45] The value of the sense capacitor, C_{sense} , should be about 100 times greater than the capacitance of the device being tested, so that most of the applied voltage is dropped across the ACTFEL device. The voltages v_2 and v_3 in Fig. 2.10 are measured using a Tektronix model 420 digitizing oscilloscope.

For electrical characterization of ACTFEL devices, the waveform used in this work is the bipolar trapezoidal waveform, shown in Fig. 2.11. Typically, a waveform

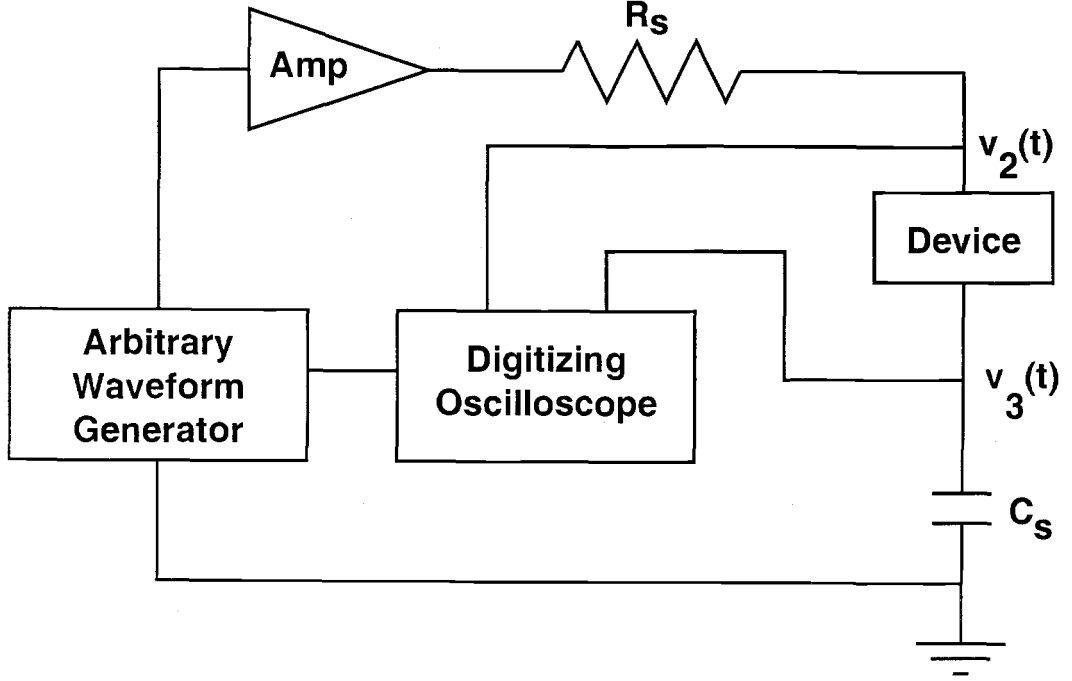


Figure 2.10: ACTFEL electrical characterization setup.

with rise and fall times of $5 \mu\text{s}$ and a $30 \mu\text{s}$ width is used. In order to match points in a data plot with points in the driving waveform, an A-J labeling scheme is used, as shown in Fig. 2.11. The points B and G identify the voltage in the waveform where the device begins conducting charge, or the turn-on voltage.

Characterization measurements are usually taken after the ACTFEL device has established a steady state with the applied voltage waveform. Depending on the type of ACTFEL device being evaluated, the number of applied voltage pulses required to establish steady state varies from several to several hundred periods of the applied voltage waveform.

2.3.2 Charge-voltage characterization

The basic technique for electrical characterization of ACTFEL devices is the charge-voltage (Q-V) measurement. A Q-V plot is obtained by plotting the charge measured on the sense capacitor, $q_{ext}(t)$, normalized to the device area, versus the

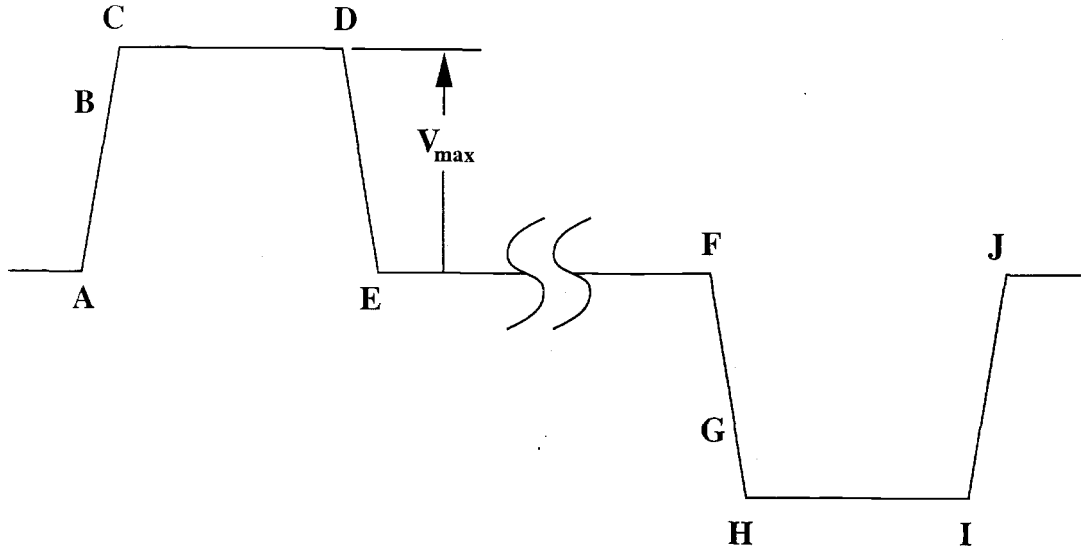


Figure 2.11: The bipolar trapezoidal waveform.

voltage measured across the device, $v_a(t)$. The external charge and applied voltage are given by

$$q_{ext}(t) = C_{sense}v_3(t) \quad (2.11)$$

and

$$v_a(t) = v_2(t) - v_3(t) \quad (2.12)$$

where $v_2(t)$ and $v_3(t)$ are as shown in Fig. 2.10. The charge Q plotted in a Q-V curve is the charge detected on the sense capacitor in the test circuit, not the actual charge inside the ACTFEL device at one of the phosphor/insulator interfaces. The voltage V in a Q-V curve is the voltage drop across the ACTFEL device, which is slightly different than the output of the high voltage output because some of the output voltage drops across the series resistor and the sense capacitor.

A Q-V curve assesses several physical parameters about ACTFEL devices. The amount of charge on the sense capacitor at various portions of a Q-V curve have physical meaning. These charges are labeled in Fig. 2.12. Q_{cond} is the conduction charge transported across the phosphor during the voltage pulse, which impact excites lu-

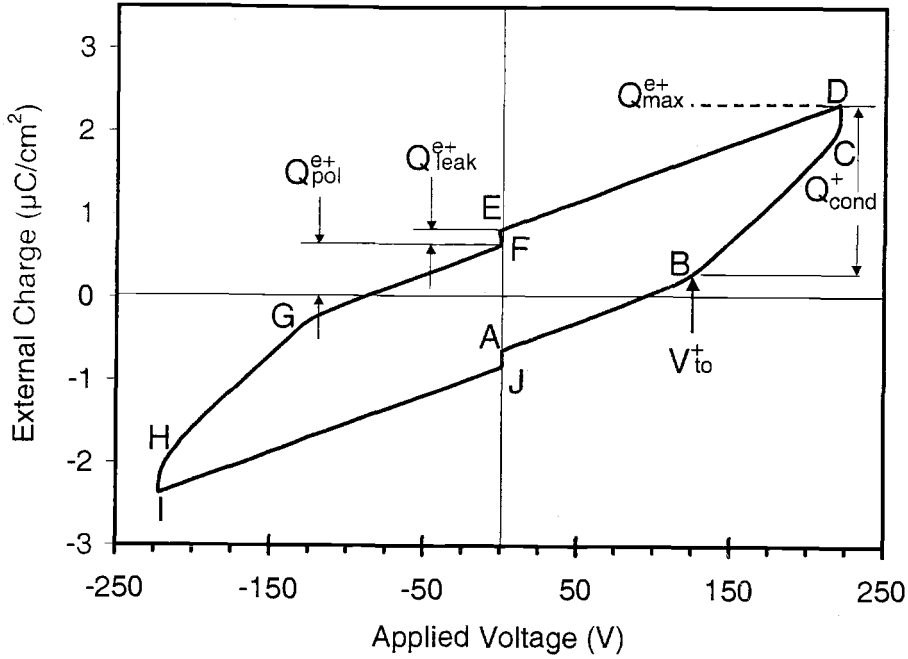


Figure 2.12: A Q-V curve for an evaporated ZnS:Mn ACTFEL device.

minescent centers and gives rise to light emission. The charge that flows across the phosphor during the portion of the waveform at which the applied voltage is constant at its maximum value, V_{max} , and the phosphor field decreases, or relaxes, is the relaxation charge, Q_{relax}^e . Q_{leak}^e is the leakage charge resulting from the emission of electrons from shallow interface states during the portion of the waveform where the voltage is zero. The polarization charge, Q_{pol}^e , is the charge stored at the phosphor/insulator interface just prior to the onset of the ensuing pulse of opposite polarity. The charge labeled Q_{max}^e in Fig. 2.12 is the maximum external charge and corresponds to the maximum voltage measured across the sense capacitor for a given applied voltage. Also apparent in a Q-V curve are the two turn-on voltages, V_{to} , the positive turn-on voltage being marked in Fig. 2.12. The turn-on voltage often differs for positive and negative portions of the Q-V curve because of polarization charge. The magnitude of polarization charge, and therefore the turn-on voltage, depends on V_{max} . The turn-on voltage should not be confused with the threshold voltage,

V_{th} , which is the lowest value of V_{max} at which the phosphor first begins conducting charge and significant light emission initiates.

A Q-V curve loops in a counter-clockwise direction, as observed in Fig. 2.12. The A through J labels correspond to the labels of the driving waveform (Fig. 2.11). The point labeled A in Fig. 2.12 corresponds to the onset of a positive voltage pulse applied to the top electrode. The charge value at point A is nonzero because of polarization charge residing on the phosphor/insulator interfaces, which is left behind from the previous pulse of opposite polarity. The portion of the Q-V curve below the turn-on voltage (the portions labeled AB and FG in Fig. 2.12) has a slope equal to that of the total capacitance of the series combination of the insulator and phosphor layers of the ACTFEL device. From point B to point C, the phosphor is conducting and is effectively shorted, and the slope is ideally equal to the physical capacitance of the series combination of the two insulators, C_i . The slope of the BC (and GH) portion of the Q-V curve can become much larger than C_i if there is a generation of positive space charge in the phosphor layer during this time. [46] From point C to point D, the applied waveform is constant at its maximum value and the increase in charge is relaxation charge. During the DE portion of the Q-V curve, the applied voltage decreases to zero; this is the trailing edge portion of the voltage waveform. The EF segment is the time between the end of the positive portion of the waveform and the beginning of the rise of the negative polarity pulse. The process repeats with the external applied voltage having negative polarity in the F to A portion of the curve.

2.3.3 Capacitance-voltage characterization

Capacitance-voltage (C-V) curves are created by plotting the dynamic capacitance of an ACTFEL device as a function of the voltage applied to the ACTFEL device during the rising edge of the applied voltage waveform. [47, 48] The dynamic capacitance is the slope of the Q-V curve and is plotted for the rising edge of both

the positive and negative portions of the applied voltage waveform. The dynamic capacitance is calculated from

$$C = \frac{i(t)}{\frac{dv_a(t)}{dt}}, \quad (2.13)$$

where

$$i(t) = \frac{dq_{ext}}{dt} = C_{sense} \frac{dv_3(t)}{dt} \quad (2.14)$$

and $v_a(t)$ is as given in Eq. 2.12. Substituting Eq. 2.14 into Eq. 2.13 gives the dynamic capacitance in terms of the differences of raw data values,

$$C = C_{sense} \frac{dv_3(t)}{dv_a(t)}. \quad (2.15)$$

The quantity C in Eq. 2.15 is plotted against $v_a(t)$ to generate a C-V curve. C-V curves for an evaporated ZnS:Mn ACTFEL device are shown in Fig. 2.13 taken with driving waveforms of maximum amplitude 20, 40, and 60 V above V_{th} . The capacitance in a C-V curve for the smaller voltages corresponds to the total capacitance of the ACTFEL device. Ideally, the above turn-on capacitance is equal to the insulator capacitance, C_i , of an ACTFEL device because the phosphor layer is shorted. The turn-on voltage V_{to} is apparent in a C-V curve as the voltage where the capacitance increases from C_t to C_i . In reality, not many ACTFEL devices have an above turn-on capacitance in a C-V curve, C_i^{cv} , equal to the physical insulator capacitance, C_i^{phys} , assessed from film thickness and dielectric constant measurements. [49] The shape of a C-V curve and its dependence upon V_{max} are indicators of whether the transferred charge is interface or bulk derived. The rigid shift of the C-V curves to smaller voltages with increasing V_{max} shown in Fig. 2.13 is characteristic of an ACTFEL device in which the electrons derive exclusively from interface states. If the initial portion of the C-V transition is soft and the C-V curves shift in a non-rigid manner, it is likely that a substantial portion of the transferred charge is bulk derived. [11]

Two deviations from the ideal above turn-on situation exist, $C_i^{cv} < C_i^{phys}$, and $C_i^{cv} > C_i^{phys}$. When $C_i^{cv} < C_i^{phys}$, there is an insufficient amount of conduction current during the rising edge of the applied waveform to completely shunt the phosphor

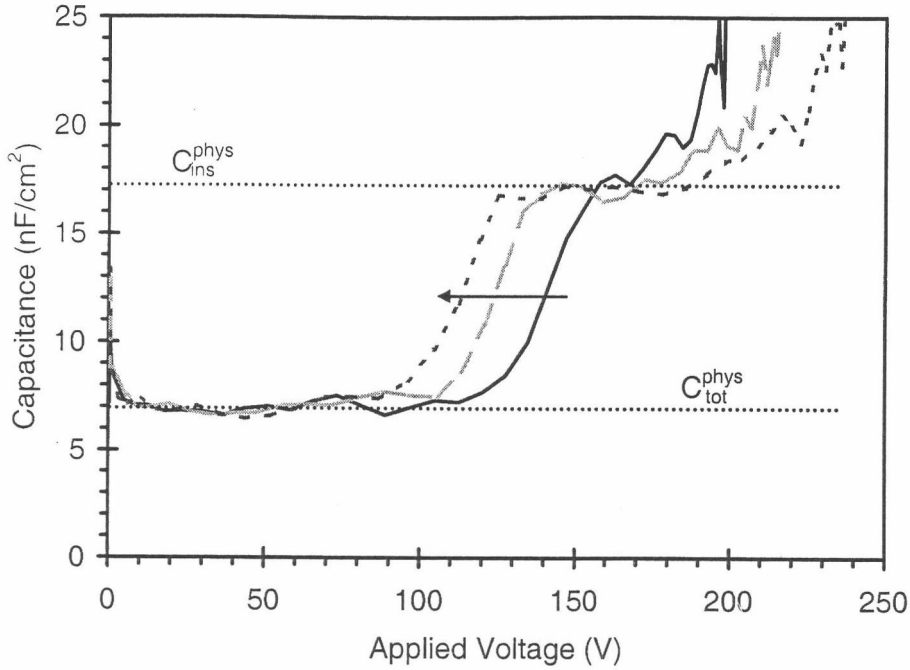


Figure 2.13: C-V curves for an evaporated ZnS:Mn ACTFEL device taken at 20, 40, and 60 V above threshold. The arrow indicates the direction of increasing voltage.

layer. [50] This can be attributed to an inadequate density of interface states or carrier multiplication in the phosphor bulk. [17] If $C_{ins}^{cv} > C_{ins}^{phys}$ occurs, a common situation, the average phosphor field is decreasing as the applied voltage is incrementally increased. This situation arises when positive space charge is generated in the phosphor layer, which serves to lower the average phosphor field as the voltage slews up. [16, 19]

2.3.4 Internal charge-phosphor field characterization

The internal charge-phosphor field ($Q-F_p$) technique was developed to obtain information about the device physics that is not obvious in a Q-V curve. A $Q-F_p$ curve is obtained by plotting the instantaneous internal charge $q(t)$ versus the internal phosphor field $f_p(t)$. [51] The internal charge and phosphor field are related to the

external voltages and external charge by

$$q(t) = \frac{C_i + C_p}{C_i} q_{ext}(t) - C_p [v_2(t) - v_3(t)] \quad (2.16)$$

and

$$f_p(t) = \frac{1}{d_p} \left(\frac{C_{sense} v_3(t)}{C_i} - [v_2(t) - v_3(t)] \right) \quad (2.17)$$

where C_i is the insulator capacitance, C_p the phosphor capacitance, and d_p the phosphor thickness. [10] In contrast to a Q-V curve, a Q- F_p curve loops in a clockwise direction and the types of charge obtainable are all internal rather than both internal and external, and are therefore directly comparable. The Q- F_p curve also provides the average steady-state phosphor field, F_{ss} , while a Q-V curve does not. F_{ss} is the constant or nearly constant average phosphor field which exists in the device during the leading edge of the applied voltage waveform in which the applied voltage exceeds the turn-on voltage. If the steady-state fields at different maximum applied voltages above V_{th} are independent of V_{max} , then the ACTFEL device is said to exhibit strong field clamping. The field may overshoot the steady-state value around points B and/or G due to dynamic space charge generation in the phosphor bulk.

The shape and accuracy of a Q- F_p curve depend directly upon the phosphor and insulator capacitances and the phosphor thickness, as seen in Eqs. 2.16, 2.17 and 2.2. An uncertainty in the phosphor thickness is reflected in an uncertainty in the phosphor field. Uncertainties in the estimates of C_i and C_p cause distortion in the shape of a Q- F_p curve. [52] Plotting a Q- F_p curve is an effective way to monitor the accuracy of the estimated values of C_i and C_p . Deviations from the estimated values and the values of C_i and C_p that give the most ideal shaped Q- F_p curve are a result of dynamic space charge in the ACTFEL device under study. [53]

2.3.5 Maximum charge-maximum voltage characterization

Maximum charge - maximum voltage (Q_{max} - V_{max}) analysis is another characterization technique used to provide information about the properties of ACTFEL

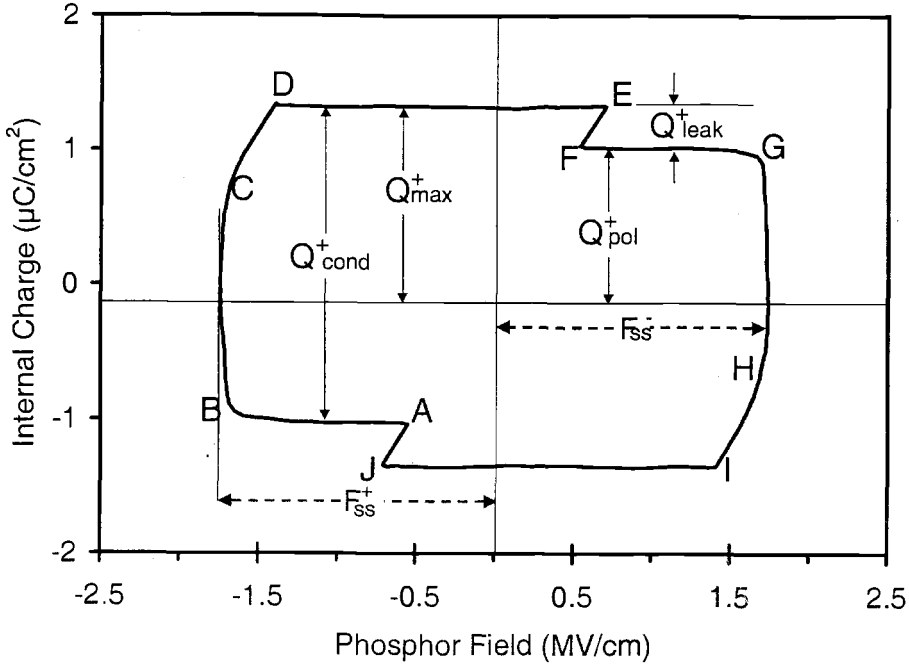


Figure 2.14: A Q - F_p curve for an evaporated ZnS:Mn ACTFEL device.

devices. [49, 54] The maximum charge stored on the sense capacitor is plotted against the maximum voltage of the applied voltage waveform in a Q_{max} - V_{max} curve. This is typically performed over a range of maximum voltages beginning below the threshold voltage to a value 40 - 60 V above V_{th} . Both the maximum internal charge (Q_{max}), analogous to the points of maximum charge in a Q - F_p plot, and the maximum external charge (Q_{max}^e), analogous to the maximum charge in a Q - V curve, can be plotted for this measurement. The Q_{max}^e - V_{max} measurement gives more reliable results than the Q_{max} - V_{max} measurement because Q_{max}^e is a directly measured quantity, while the value of Q_{max} is dependent on how certain the phosphor and insulator capacitances are known.

A Q_{max}^e - V_{max} curve for a ZnS:Mn ACTFEL device is shown in Fig. 2.15. The initial slope of the external charge curve is equal to the total capacitance of the device. The threshold voltage of a Q_{max}^e - V_{max} curve usually correlates well with the threshold assessed from a luminance-voltage (L - V) curve. Since the slope of the Q_{max}^e - V_{max}

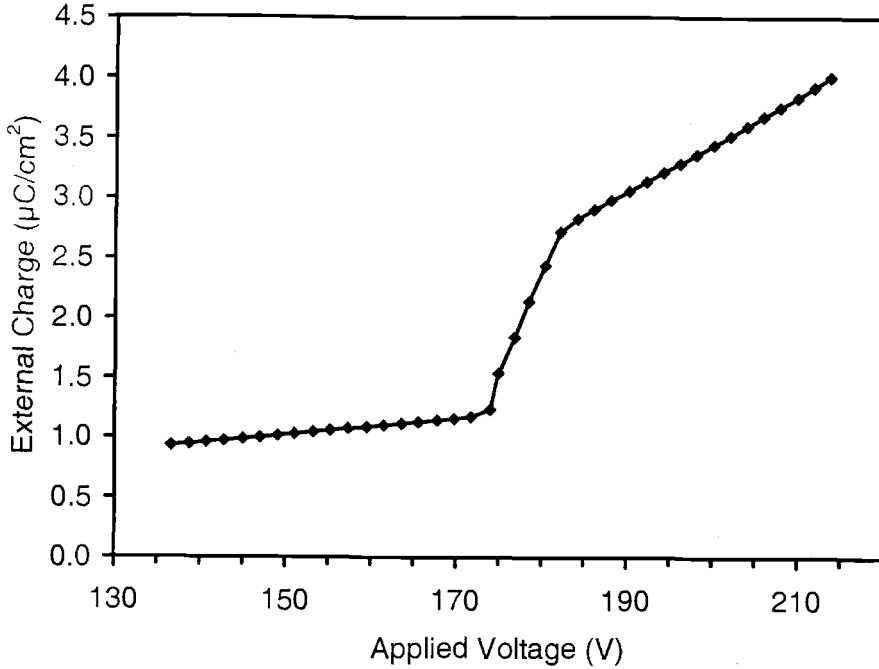


Figure 2.15: A Q_{max}^e - V_{max} curve for an ALE ZnS:Mn ACTFEL device.

curve is of primary interest, it is useful to also plot its derivative, the $\frac{dQ_{max}^e}{dV_{max}}$ - V_{max} curve, shown in Fig. 2.16. The slope of a Q_{max}^e - V_{max} curve above the threshold voltage may be greater than, less than, or equal to the physical insulator capacitance C_i^{phys} . For an ideal ACTFEL device, the post-threshold slope of the external charge is equal to the insulator capacitance.

In the transition from below to above the threshold voltage, ACTFEL devices often exhibit overshoot. The source of overshoot in the transferred charge derivative curves it has been attributed to the formation of space charge in the phosphor layer. [22] Initially, overshoot in transferred charge derivative curves for ZnS:Mn was attributed to metastable hole traps at the interfaces. [27] This was shown to not be the case by the fact that the overshoot was dependent on the phosphor thickness. [55] It is thought that holes are generated near the cathodic interface through the process of band-to-band impact ionization and are trapped as they drift across the phosphor layer. [56] This may seem unlikely due to the high field involved, but there

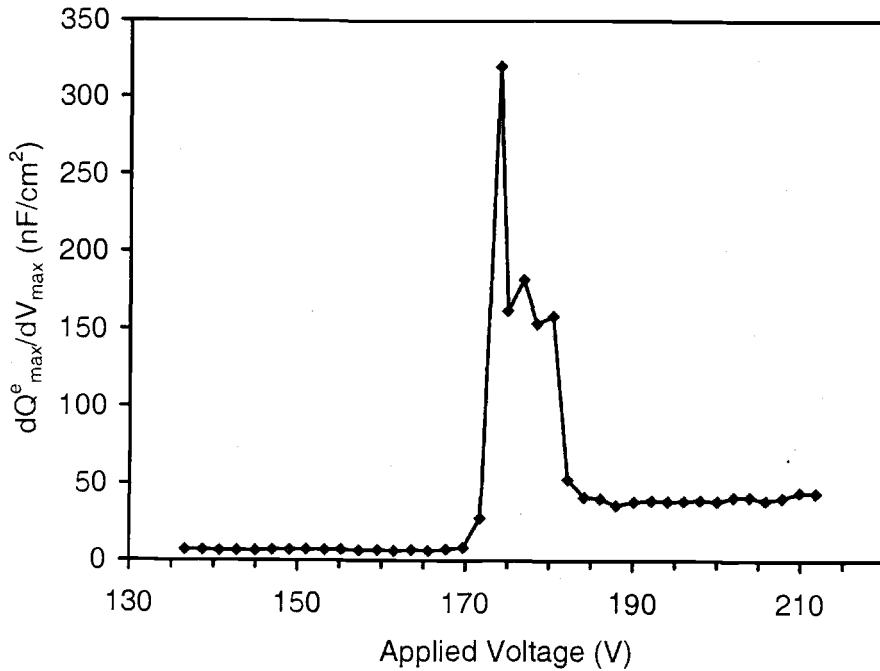


Figure 2.16: A $\frac{dQ_{\max}^e}{dV_{\max}}-V_{\max}$ curve for an ALE ZnS:Mn ACTFEL device.

is experimental evidence for bulk hole trapping at high fields. [8, 28] Space charge could also arise from the ionization of trap states in the bulk phosphor via emission of a trapped electron to the conduction band.

2.4 Conclusion

This chapter is a summary of ACTFEL device operation and common characterization techniques. An introduction to general ACTFEL operation issues is given. The cited references provide additional information on the topics presented.

3. ACTFEL MATERIALS AND LUMINESCENT IMPURITY ISSUES

This chapter begins with a description of material requirements for the constituent layers of ACTFEL devices. Next, thin-film deposition methods commonly used in ACTFEL device processing and impurity diffusion are reviewed. Finally, an overview of luminescent impurities commonly used in ACTFEL devices is given.

3.1 ACTFEL device materials

The operation of an ACTFEL device is dependent on the performance of all of the constituent layers. Especially important are the properties of the phosphor and insulator layers. This section describes ACTFEL device thin-film layer requirements and discusses properties of commonly employed materials.

3.1.1 The phosphor layer

There are many material systems available for use as phosphors; however, only certain phosphors satisfy the requirements necessary for use as ACTFEL device phosphors. Because of high field operation and the need for energetic electrons in the phosphor conduction band, many phosphor materials are not suitable for ACTFEL applications. Currently, the only two ACTFEL phosphors with the luminance, efficiency, and stability satisfactory for use commercially are ZnS:Mn and SrS:Ce.

The first requirement of an ACTFEL phosphor host material is that the bandgap be large enough to emit visible light from the luminescent centers without absorption. If the bandgap is too small, optical absorption of emitted photons in the phosphor layer prevents emitted light from reaching the viewer. Also, a phosphor material with a bandgap that is too large generally has relatively deep interface states that do not emit a sufficient number of electrons at fields reached with reasonable applied voltages (<300 V). These limits put the range of bandgaps suitable for ACTFEL

phosphor applications at ~ 3 to ~ 4.5 eV. It is also useful to know the transition type of the bandgap and the effective masses of the principal conduction bands, because of their influence on interface carrier injection. The emission rate due to pure tunneling from a coulombic interfacial trap is exponentially dependent on the square root of the effective mass of the lowest lying conduction band. [25]

The second ACTFEL phosphor material requirement is that the dielectric properties be such that an electric field large enough for electron injection can be achieved and that the injected electrons are efficiently transported in the phosphor layer. The applied voltage is dropped across both the insulator layers and the phosphor layer. Scrutiny of Eq. 2.2 reveals that the condition $C_{ph} \ll C_{ins}$ will ensure a larger phosphor field. Therefore, the dielectric constant of the phosphor should be as small as possible relative to the insulator, so that most of the applied voltage drops across the phosphor layer rather than across the insulator.

One final restriction on the phosphor material of an ACTFEL device is imposed by the use of glass as a substrate. The best ACTFEL devices are made when the phosphor layer achieves a high degree of crystallinity and a large grain size. [57, 58, 59, 60, 61] Delocalized carrier transport through the phosphor, which is necessary for a hot electron distribution that will efficiently excite luminescent centers, increases dramatically with higher crystallinity. [62] Electron transport in amorphous or poorly crystallized material is via hopping rather than normal, extended state band transport; hopping conduction is a much less efficient means of electron transport than delocalized band state conduction. Improving the crystallinity of the phosphor will enhance the transport of electrons at high fields. It has been proposed that polycrystalline grain growth begins at temperatures roughly half of the melting temperature of a material. [63] This implies that phosphor materials with melting temperatures above $\sim 1300^\circ\text{C}$ will not produce high quality ACTFEL devices on substrates that cannot tolerate temperatures above 650°C . This limit is relaxed with the use of post deposition rapid thermal annealing, where temperatures in excess of

the substrate melting temperature can be reached for short periods of time. Higher temperature substrates are also available, but are generally expensive.

The phosphor material should be chemically stable. Ideally, it should be non-hygroscopic because the phosphor will be exposed to air and moisture during and after fabrication. The ACTFEL phosphor must remain stable throughout the lifetime of the device in order to maintain constant performance.

Current ACTFEL phosphor host materials are limited by these requirements to alkaline-earth sulfides, MS, ZnS, and the ternary alkaline-earth thiogallates, MGa_2S_4 (M: Ca, Sr, Ba). Oxide materials are generally quite refractory and possess bandgaps too large for ACTFEL applications, although some ternary oxide materials, such as Zn_2SiO_4 , Zn_2GeO_4 , ZnGa_2O_4 , etc., may be suitable hosts. The crystallinity issue with refractory oxide phosphors with a suitable bandgap may be alleviated with the use of grain growth fluxes or creative annealing techniques. The polycrystallinity attainable in the sulfide materials at temperatures under 800°C is sufficient to give bright and efficient ACTFEL devices. The melting points of binary sulfides are several hundred degrees lower than the corresponding oxide, which implies that these sulfides can be processed at temperatures compatible with glass substrates. The sulfide phosphors also exhibit excellent charge injection properties, especially ZnS and SrS. Several relevant physical properties for ZnS and the MS phosphor hosts are summarized in Table 3.1.

Phosphors generally consist of a host material and a light-emitting dopant, known as an activator or a luminescent impurity. The luminescent impurity ordinarily replaces the cation of the host material. Matching of the cation and dopant ionic radii is desirable for crystallinity and stability reasons, but several bright and efficient ACTFEL phosphors are known where the ionic radii are not closely matched. Another critical parameter is the valence of the activator and whether it matches that of the cation. If the formation of Schottky defects, also known as vacancies, is not desired, then the valence of the cation and activator should match, unless other dopants are

Table 3.1: Properties of phosphor host materials used in ACTFEL devices.

Host Material	β -ZnS	CaS	SrS	BaS
Band gap (eV)	3.6	4.4	4.3	3.8
Transition type	direct	indirect	indirect	indirect
Crystal structure	zinc blende	rock salt	rock salt	rock salt
Lattice constant (\AA)	5.409	5.697	6.019	6.384
Cation radius (pm)	74	114	132	149
Dielectric constant	8.3	9.3	9.4	11.3
Melting point ($^{\circ}\text{C}$)	1700	2400	>2000	1200

utilized to extrinsically compensate the valence mismatch. The ionic properties of several luminescent impurities are given in Table 3.2. Specific properties of some luminescent centers are discussed in more detail in Sec. 3.3.

The most extensively studied ACTFEL phosphor is Mn^{2+} doped ZnS, or ZnS:Mn. ZnS:Mn emits an amber colored light with a broad emission spectrum peaked at approximately 585 nm. Most current commercial ACTFEL products are based on ZnS:Mn phosphors. Ce^{3+} doped SrS is a blue-green emitting phosphor also found in commercial products and has been extensively studied for ACTFEL applications. SrS:Ce is usually found as the blue emitting phosphor in a multicolor ACTFEL display, with ZnS:Mn providing the red and green components.

Producing a full-color ACTFEL display may be accomplished by the color-by-white approach or the patterned phosphor approach. The color-by-white approach uses a white phosphor and color filters to produce the primary colors red, green, and blue. The patterned phosphor approach produces full color by patterning pixels of phosphors that emit the three primary colors. The target luminance, efficiency, and

Table 3.2: Properties of luminescent impurities.

Ion	Ionic radius (pm)	emission orbital	lifetime (s)	emission structure
Mn ²⁺	80	3d ⁵	~10 ⁻³	broadband
Ce ³⁺	115	5d→4f	10 ⁻⁷ -10 ⁻⁸	broadband
Cu ⁺	91	3d ⁹ 4s ¹ →3d ¹⁰	10 ⁻⁶	broadband
Eu ²⁺	131	4f ⁶ 5d→4f ⁷	10 ⁻⁵ -10 ⁻⁶	broadband
Eu ³⁺	108.7	4f ⁶ →4f ⁶	10 ⁻³	sharp lines
Tb ³⁺	106.3	4f ⁸ →4f ⁸	10 ⁻³	sharp lines

CIE color coordinates for the three primary colors to produce a high quality full-color ACTFEL display are listed in Table 3.3, where L_{40} and η_{40} are the luminance and efficiency at 40 volts above V_{th} , respectively. ZnS:Mn and SrS:Ce are currently the most developed ACTFEL phosphors, but neither emits a saturated primary color. Attempts have been made to produce full-color displays with these phosphors by combining the layers in a single device to create a nearly white emission, which is then filtered into the primary colors. Producing the desired chromaticity by filtering comes at the cost of reduced brightness and efficiency. This method is especially lacking in blue emission, because the SrS:Ce color is far from an adequate blue chromaticity. If a suitable blue phosphor develops, a hybrid full color ACTFEL display could be produced by patterning the blue phosphor and ZnS:Mn and filtering ZnS:Mn for green and red. Blue emitting SrS:Cu and SrS:Cu,Ag have recently become the subject of considerable study for ACTFEL phosphors. Excellent blue chromaticity has been obtained with SrS:Cu,Ag based ACTFEL devices. Also under investigation as blue ACTFEL phosphors are CaS:Pb and BaAl₂S₄:Eu. [64, 65]

Table 3.3: Target luminance, efficiency, and CIE coordinates (60 Hz) for a high-luminance full-color ACTFEL display.

Color	L_{40} (cd/m ²)	η_{40} (lm/W)	CIE x	CIE y
Green	310	2.0-3.0	0.30	0.60
Red	155	1.0-1.5	0.65	0.35
Blue	52	0.3-0.5	0.15	0.10

3.1.2 Insulator layers for ACTFEL devices

The insulating layers of ACTFEL devices play a pivotal role in device operation and act to protect the phosphor layer from destructively large currents when electrical breakdown occurs. The insulator properties most relevant for ACTFEL devices are the breakdown electric field, the dielectric constant, and the bandgap. An insulator with a large dielectric constant is desired so that the capacitance of the insulator is large. A large insulator capacitance relative to the phosphor capacitance results in a larger voltage drop across the phosphor and therefore a larger electric field in the phosphor. This in turn results in a higher luminous efficiency, since less power is required to produce the steady-state phosphor field with a higher capacitance insulator.

The breakdown electric field of the insulating material, E_{BD} , should be large enough to prevent electric breakdown of the insulator during device operation. The dielectric breakdown electric field, E_{BD} , or breakdown strength, is the maximum electric field a material can withstand without experiencing failure of its insulating properties. The breakdown field is generally proportional to the bandgap. When the phosphor layer becomes conducting above turn-on, the additional applied voltage is dropped across the insulator layers. A high breakdown field is required to withstand this voltage. Materials with large dielectric constants typically have small

Table 3.4: Properties of dielectric materials commonly used as ACTFEL insulators.

Insulator	E_g (eV)	ϵ_r	E_{BD} (MV/cm)	$\epsilon_0\epsilon_r E_{BD}$ ($\mu\text{C}/\text{cm}^2$)	Breakdown mode
SiO_2	8	4	6	2	SHB
SiO_xN_y	5.1-8	6	7	4	SHB
Si_3N_4	5.1	8	6-8	4-6	SHB
Al_2O_3	9.7	8	5-8	3.5-6	SHB
Y_2O_3	5.6	12	3-5	3-5	SHB
BaTiO_3	3.75 [66]	14	3.3	4	SHB
Sm_2O_3	2.13 [67]	15	2-4	3-5	SHB
HfO_2	5.6	16	0.17-4	0.24-5.7	SHB
BaTa_2O_6	?	22	3.5	7	SHB
Ta_2O_5	4.6	23-25	1.5-3	4-6	SHB
TiO_2	3.2	60	0.2	1	PB
SrTiO_3	3.4 [68]	140	1.5-2	19-25	PB
PbTiO_3	3.4	150	0.5	7	PB

breakdown fields, and vice-versa. The figure of merit for an insulating material for ACTFEL applications is the product of the breakdown field and the dielectric constant, $\epsilon_0\epsilon_r E_{BD}$. This figure of merit reflects the maximum trapped charge density at the phosphor/insulator interface. Table 3.4 lists the dielectric properties of materials commonly used as insulators in ACTFEL devices. [6]

The breakdown mode of a dielectric material is another important characteristic for ACTFEL devices. The two modes of dielectric breakdown are propagating and self-healing. Propagating breakdown (PB) occurs when the electric breakdown

in a small area of the insulator expands to neighboring regions of the insulator, resulting in catastrophic failure of the device. Self-healing breakdown (SHB) is the opposite of propagating breakdown, where the microscopic insulator breakdowns remain localized. Insulating thin-films for ACTFEL applications must break down in the self-healing manner. The number of pinholes and defects in the insulating layers should be minimized so that local breakdown does not cause catastrophic failure of a display.

The insulators in an ACTFEL device should also have a small loss tangent, $\tan\delta$. The loss tangent is a measure of the dissipative characteristics and should be minimized. A large loss tangent implies that charge is leaking through the insulators, which reduces device efficiency by consuming more power. Finally, it is necessary that insulators adhere well to the neighboring layers.

3.1.3 Transparent contacts

Transparent conducting films for EL devices must have high conductivity values and high transmittance in the visible region. The best suited transparent conducting film is an alloy consisting of 90wt% In_2O_3 and 10wt% SnO_2 , commonly referred to as indium-tin-oxide, or ITO. Typical sheet resistance values for ITO thin films are 5-10 Ω/\square for a standard thickness of 2000 Å. The high conductivity is due to oxygen vacancies and donor impurities created by Sn^{4+} ions occupying In^{3+} sites. The conductivity of ITO is reduced if it is heated in an atmosphere where oxygen is present. The forbidden bandgaps of In_2O_3 and SnO_2 are both greater than 3 eV, so the material is transparent to visible light. Surface flatness is an important factor in addition to conductivity and transmittance. Poor flatness leads to electric breakdown and nonuniform emission. Sputtered ITO films have a very smooth surface. Other conducting materials are sometimes used for the transparent contact in research devices, such as ZnO:Al and CdSnO_3 .

3.1.4 Opaque contacts

The opaque contact in a standard structure ACTFEL device should have good adhesion to the neighboring insulating layer, no metal-ion migration under high electric fields, and low resistivity. The top contact of almost all standard structure ACTFEL devices is an Al electrode. The typical thickness is 1000 to 1500 Å, so that the Al electrode is thick enough to be opaque and thin enough to prevent propagating breakdown if dielectric breakdown of the phosphor layer or insulating layers occurs. Al is not useful for inverted structure devices because it melts when high-temperature annealing is performed. A refractory metal, such as Mo, Ta, or W, is usually used for inverted structure devices. [6]

3.1.5 Substrates

The substrate used for the standard structure ACTFEL device must be transparent and able to withstand the high-temperature processing used to crystallize the phosphor layer. The most common substrate used is Corning 7059 glass, a non-alkaline, phosphosilicate glass with a softening temperature of 598°C. Large size display panels are able to withstand rapid thermal annealing (RTA) at temperatures up to 650°C without warping, while smaller test samples can undergo RTA processes at temperatures of 850°C without catastrophic warpage. Glass substrates with higher softening temperatures (~200°C higher) are available, but are not practical because of their cost. To go to higher annealing temperatures without destroying the substrate, an inverted structure with opaque substrates is required. Silicon wafers and alumina substrates are often used for the inverted structure. BaTiO₃ is also used as a substrate which doubles as an insulating layer. [69]

3.2 Thin-film processing

In this section, processing methods used to fabricate thin-film layers in ACTFEL devices are discussed. The deposition methods most important for the fabrica-

tion of ACTFEL devices, such as electron-beam and thermal evaporation, sputtering, atomic layer epitaxy, and chemical vapor deposition, are explored. Also crucial to producing high quality ACTFEL devices is the process of post-deposition thermal annealing, so it is also examined in this section.

3.2.1 Evaporation

The basic physical vapor deposition process is evaporation. Evaporation takes place when a substance is heated to its vapor pressure. The vapor pressure is the pressure of vapor in equilibrium with its condensed phase at a specified temperature. [70] At high vacuum pressures, vaporized atoms are able to travel tens of meters without suffering a collision with other particles, permitting deposition onto surfaces away from the evaporating source material. Different evaporation techniques are distinguished by the manner in which the source material is heated to its vapor pressure. Two common evaporation techniques are thermal evaporation and electron beam evaporation (EBE). Thermal evaporation involves heating a crucible or boat containing the material to be evaporated by passing current through it. Electron beam evaporation is accomplished by heating the source material via a focused beam of energetic electrons (~ 10 keV). Thermal evaporation is the simplest method of evaporation, but is not suitable for materials with high vaporization temperatures. Any material can be evaporated by EBE, so long as the material does not conduct heat away too quickly. Poor conductors of heat, such as ceramics, are easily evaporated by EBE, while EBE is not well suited for materials that are good conductors of heat.

Evaporation is commonly used to deposit many of the different layers in ACTFEL devices. In fact, it is possible to build an entire ACTFEL device, from the substrate up, using evaporation methods as the deposition technique. Both the top opaque conductor and the ITO layer can be evaporated, as can many materials suitable for insulators. [71, 72] The phosphor layer may also be deposited by evaporation. Furthermore, it is advantageous at the research level to use electron beam evapora-

tion as the deposition method of the phosphor layer, rather than sputtering. The phosphor host material may be electron-beam evaporated while the dopant source is thermally evaporated. Other materials may also be co-evaporated with the host material in order to enhance film properties and improve device performance. This method allows the concentration of the dopant(s) to be varied in the phosphor without the need to undergo the elaborate task of preparing a different sputter target for each concentration. There are several disadvantages to depositing ACTFEL films by evaporation, such as the possibility of x-ray damage to films from electron beams and contamination from the evaporation crucible. It is also difficult to produce films from multinary materials and alloys by evaporation from a single source because the constituent materials generally have different vapor pressures, resulting in films with compositions different from the source material. [73]

3.2.2 Sputter deposition

The primary alternative to evaporation for film deposition is sputtering. Sputtering takes place when an energetic particle strikes the surface of a target material with enough energy to dislodge one or more surface atoms. This process is illustrated in Fig. 3.1. The energetic particles that bombard the target material to be sputtered in sputter deposition are generated in a glow-discharge. The energy of the incident ions should be large enough to elastically collide with the target surface, but not so large that the incident ions are implanted into the target. When the sputtered atoms are transported to the substrate and form a thin film, the process of sputter deposition occurs. Sputter deposition has better step coverage than evaporation, induces less radiation damage than electron-beam evaporation, and is much better at producing films of compound materials and alloys.

The glow-discharge plasma can be sustained by DC or AC voltages. Non-conducting materials cannot be sputtered with a DC glow-discharge because a DC glow-discharge plasma requires the target material to supply enough electrons to

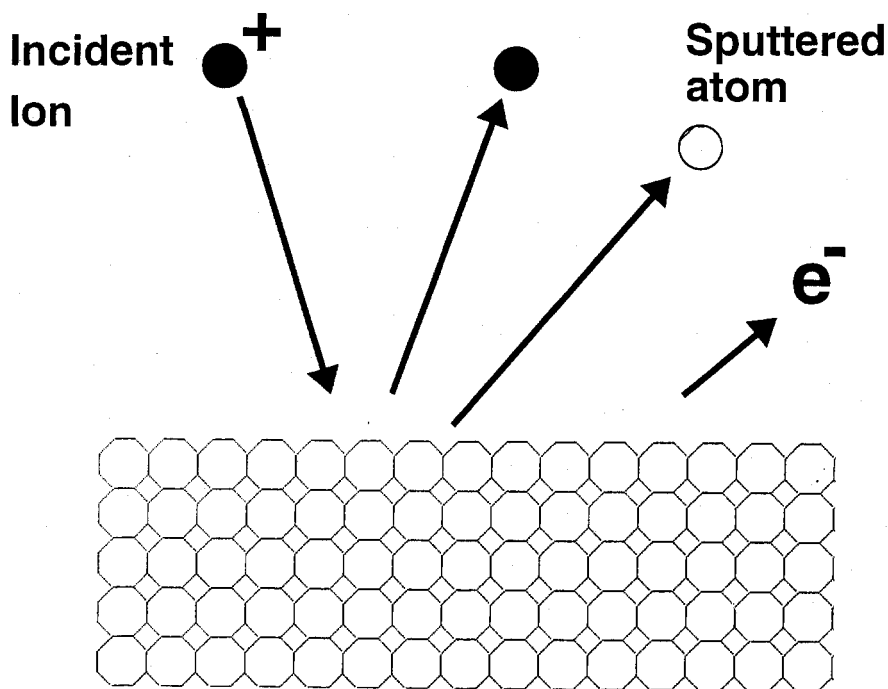


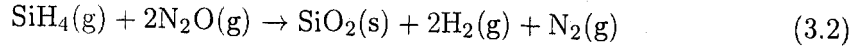
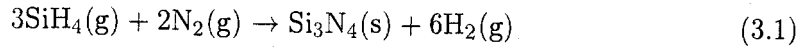
Figure 3.1: A depiction of the sputtering process.

sustain the glow discharge. This rules out DC sputtering for most ACTFEL materials. The most useful sputtering technique for ACTFEL phosphor and insulator materials is radio-frequency (RF) sputtering, where an RF AC voltage waveform is used to drive the plasma. Common variations on RF sputtering, such as magnetron and reactive sputtering, are employed in ACTFEL film deposition.

3.2.3 Chemical vapor deposition

Chemical vapor deposition (CVD) is a method of processing thin-films that is well suited for ACTFEL applications. A CVD process involves one or more reactions of precursor gases and formation of a film on a substrate from the products of reactions. The reactant gases are introduced into a reaction chamber and are decomposed and reacted at a heated surface to form a thin film. Advantages of CVD deposition include good adhesion, low pinhole density, and good thin-film uniformity.

An alternative to thermally stimulating the reacting gas is to establish a glow discharge in the reactants, known as plasma enhanced chemical vapor deposition (PECVD). Some insulators for ACTFEL devices can be deposited using PECVD. PECVD uses an RF-induced glow discharge to transfer energy to the reactant gas, rather than relying solely on thermal energy to initiate and sustain chemical reactions, which allows the substrate to remain at a lower temperature. [74] Reactions that take place in PECVD deposition of Si_3N_4 and SiO_2 , which are two possible insulators for ACTFEL devices, are given by



The quantity in parenthesis is (g) for gas and (s) for solid. The detailed process by which the reaction takes place is much more complicated; the beginning and final product is what is shown in Eqns. 3.1 and 3.2. It is also possible to form silicon oxynitride (SiO_xN_y) by reacting SiH_4 , N_2O , and N_2 , which has materials properties intermediate between SiO_2 and Si_3N_4 .

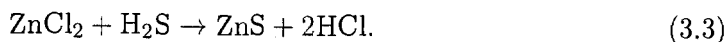
CVD offers an alternative deposition method to evaporation and sputtering that could lead to ACTFEL phosphor depositions at lower processing temperatures. SrS phosphor layers have been deposited by metal-organic chemical vapor deposition (MOCVD). [75, 76] MOCVD SrS is deposited by using $\text{Sr}(\text{thd})_2$ and H_2S as the precursor gases.

3.2.4 Atomic layer epitaxy

Another commonly used deposition technique for ACTFEL thin-films is atomic layer deposition (ALD). ALD produces high-quality films with few pinhole defects and excellent step coverage, making it a process suitable for production of ACTFEL displays. [77] The ALD technique is also attractive for ACTFEL production because it offers the possibility to produce the entire insulator/phosphor/insulator stack in one

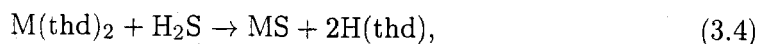
continuous process, preventing the exposure of the moisture-sensitive phosphor layer to atmosphere between process steps. The disadvantages of ALD are the expensive startup costs, slow deposition rates, and difficult precursor chemistry. ALD, also referred to as atomic layer epitaxy (ALE), is similar to CVD in that the films are deposited by reacting precursor gases on the substrate. Rather than introducing the reactants to the substrate at the same time, as is done in CVD, ALD separates the individual reactants. In the ALD process the heated substrates are exposed sequentially to the reactant gases.

The ALD process for ZnS relies on the reaction of a Zn containing compound, such as ZnCl_2 , with H_2S in the following manner:



The growth begins by introducing ZnCl_2 in the gaseous phase, which is adsorbed on the surface of the heated substrate. The excess ZnCl_2 vapor is purged by a short burst of an inert gas. Next the anionic precursor H_2S is allowed into the process chamber where some of the molecules are adsorbed onto the first monolayer of molecules containing the cationic species. The desired ZnS compound is formed by the reaction given in Eq. 3.3 and the biproduct HCl is devolved from the deposited film as vapor. A second burst of inert gas into the chamber purges the excess H_2S and the emitted HCl vapors, leaving only the monolayer of the film being grown. The cycle is repeated until enough layers have been deposited to reach the desired film thickness. Figure 3.2 depicts the process of growing one monolayer of ZnS by ALD.

The ALD method has been applied to the deposition of SrS and CaS phosphor layers in ACTFEL devices. [78] The reaction that takes place is



where M is either Ca or Sr, and thd stands for 2,2,6,6-tetramethyl-3,5-heptanedionate. Doping of the phosphor host with Ce is accomplished using $\text{Ce}(\text{thd})_3$ as the source

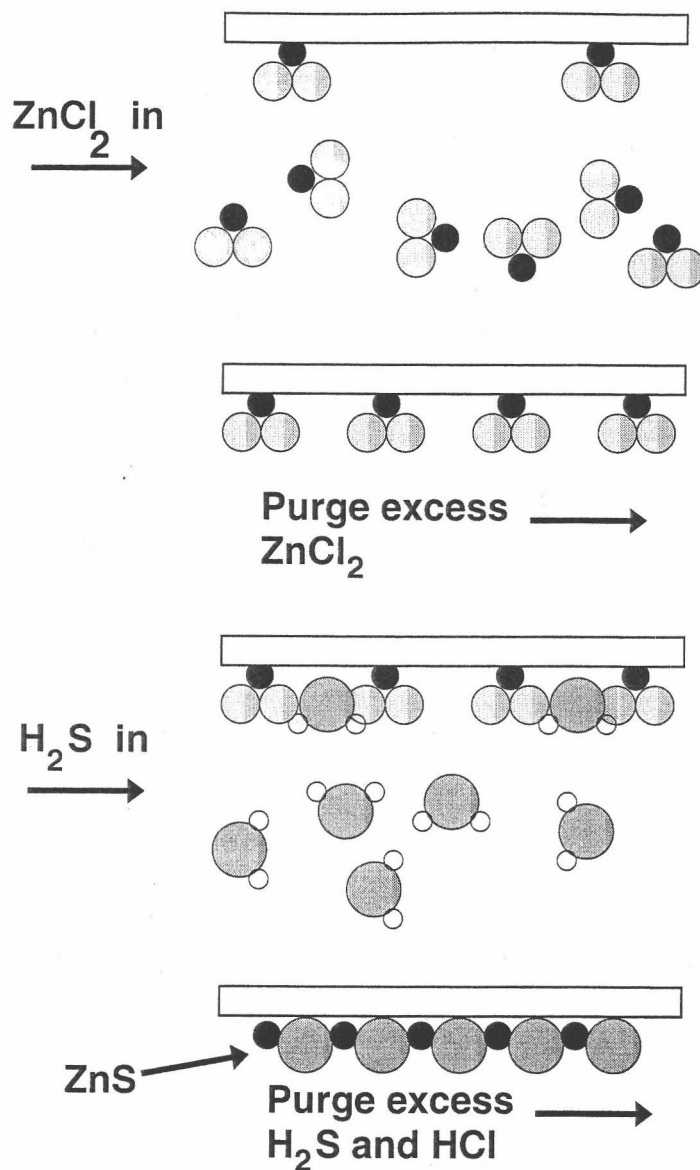


Figure 3.2: Atomic layer deposition of one monolayer of ZnS.

precursor gas to give good luminous efficiency for display application. [6] Producing a suitable Cu precursor for deposition of SrS:Cu by ALD has proven difficult.

3.2.5 Post-deposition annealing

The performance of an ACTFEL device is greatly affected by the crystallinity of the phosphor layer. Thermal annealing improves the phosphor layers by removing

strain in the films, enhancing crystallinity, and promoting impurity diffusion. The polycrystalline grain size of the phosphor layer has been found to be critical for obtaining good luminance and efficiency with ACTFEL devices. [57, 58, 59, 60, 61] Post-deposition annealing of the phosphor film is performed in either a traditional furnace or a rapid thermal annealing (RTA) furnace.

Rapid thermal annealing involves heating a sample for a short period of time at an elevated temperature. The temperature in the RTA furnace can be ramped up and cooled down in a few seconds, which is advantageous for films on glass substrates because temperatures 200°C above the substrate softening temperature can be attained for short times without significant warpage to the substrate.

The atmosphere in the furnace during annealing plays an important role in the properties and final quality of the thin-film phosphor. It is often beneficial to use a gas containing the anionic species of the material being annealed, in order to replace anions lost during the deposition of the film. In certain situations it is advantageous to anneal sulfide films in H₂S. Depending on the nature of the film, different gases are used. If a reducing atmosphere is desired, H₂ may be used. An inert atmosphere for annealing sulfide phosphors is often desired, in which case N₂ or Ar is used. Oxides are often annealed in O₂, but N₂/H₂ or Ar may also be used if excessive O content is not desired in the film.

An important issue during the annealing process of ACTFEL phosphors is atomic diffusion within the phosphor. The crystallization and impurity redistribution processes that occur during annealing are both dependent on diffusion. If the concentration of a species, $C(x, t)$, varies within a material, there will be a tendency for the atoms to flow in the direction that creates a reduction in the concentration gradient. [74] The flow J is expressed mathematically by Fick's First Law,

$$J = -D \frac{\partial C(x, t)}{\partial x}, \quad (3.5)$$

where D is the diffusion constant for the atom in the specific material. The diffusion constant D is exponentially dependent on temperature, T , represented by

$$D = D_0 e^{-\frac{E_a}{kT}}, \quad (3.6)$$

where D_0 and E_a are independent of temperature, and k is Boltzmann's constant. The frequency factor D_0 is related to the frequency of lattice vibrations and the activation energy E_a depends on the height of the energy barrier which must be overcome by the atom in order to move within the lattice.

The way in which individual atoms move to bring about diffusion depends on the type of atoms and in what material they are diffusing. One way atoms diffuse is by the vacancy mechanism, where the diffusing atom exchanges places with an adjacent vacancy. Atoms can also diffuse interstitially, by hopping from one interstitial site to another. Interstitial diffusion is likely to be favored by atoms that are relatively smaller than the host atoms, or small atoms in relatively open lattices. [79]

The diffusivity of elements along grain boundaries is ~ 100 times faster than in bulk material. [74] The grain boundaries are composed of disordered atoms and contain a large number of defects due to incomplete bonding. The atoms inside the grains are arranged in a periodic structure, similar to bulk single crystal material. The departure from periodicity at the grain boundaries alters the diffusion characteristics and dopant distribution of the material. Dopants are capable of diffusing more rapidly along grain boundaries than in crystalline regions. Dopant distribution can also be affected by grain boundaries as some dopants segregate from single crystal regions to grain boundaries.

3.3 Luminescent impurities

This section examines some of the luminescent impurities commonly found in ACTFEL devices. The two most utilized, Mn^{2+} and Ce^{3+} , are overviewed first.

Then the Cu^+ system and influences on the luminescent transition are elucidated. The section concludes with an audit of the emission properties of Eu^{2+} .

3.3.1 Mn^{2+}

Divalent Mn (Mn^{2+}) is a transition metal luminescent ion used in many luminescent materials. The Mn^{2+} ion has a broad band emission which can vary from green to deep red in color with a long decay time due to the parity and spin selection rules. Luminescence occurs due to transitions between the energy levels that arise when the $3d^5$ level is split by the crystal field. The emission color is dependent on the host lattice due to the dependence of the magnitude of $3d^5$ level splitting on crystal field.

The best ACTFEL phosphor to date is Mn^{2+} doped ZnS. The emission from Mn^{2+} in ZnS is orange-yellow with a peak around 585 nm, depending on the deposition method employed. The $d \rightarrow d$ transition is parity forbidden, but the selection rule is relaxed by the mixing of opposite-parity wave functions into the d wave functions. [80] The emission is due to the transition from the $^4\text{G}(^4\text{T}_1)$ excited state to the $^6\text{S}(^6\text{A}_1)$ ground state and is broad enough to obtain bright green and red color through filtering out the appropriate component of the ZnS:Mn emission. ZnS:Mn has many of the properties of an ideal ACTFEL phosphor. Mn^{2+} is isovalent with the Zn^{2+} cation it replaces and differs in ionic radius by only 8%. This leads to high Mn solubility in ZnS, resulting in uniform dopant distribution and a large impact cross section. The result of these conditions is the high luminance and high luminous efficiency of ZnS:Mn.

3.3.2 Ce^{3+}

The first alkaline-earth sulfide ACTFEL phosphor investigated was Ce^{3+} doped SrS. [6] The luminance of Ce^{3+} arises from the $5d^1$ to $4f^1$ transition. The $d \rightarrow f$ transition is both parity and spin allowed, resulting in a short decay time of $\sim 10^{-7}$

seconds. The $4f^1$ ground state configuration of Ce^{3+} yields two terminating levels, $^2F_{5/2}$ and $^2F_{7/2}$, due to spin-orbit coupling. [80] The $5d^1$ excited state configuration is split by the crystal field. The double band emission typical of Ce^{3+} results from the transition from the lowest crystal field component of the $5d^1$ level to the two ground state levels. The spectral position of the emission band is affected by the nephelauxetic effect, crystal field splitting of the $5d^1$ level, and the Stokes shift.

The nephelauxetic effect is the term used to describe the effect of covalency on a luminescent transition. As the degree of covalency increases in a compound, the electron clouds spread out over wider orbitals. The increased distance between the electrons reduces the interaction between them, leading to a decrease in emission energy with an increase in phosphor host covalency. Since the nephelauxetic effect is concerned with the local environment of the luminescent activator, the emission spectra of a phosphor with an activator involved in complexing with defects or coactivators can be affected by the activator source. For example, the nephelauxetic effect has been proposed to cause the shift in peak emission wavelength of $\text{SrS}:\text{Ce}$ ACT-FEL devices with Ce source. The Ce complexing with the halogen ions from a CeF_3 or CeCl_3 source results in blue or green emission, respectively, due in part to the nephelauxetic effect. [81]

The crystal field splitting of the excited state of Ce^{3+} decreases as the cation size increases in the alkaline-earth sulfides, resulting in green emission in CaS and blue-green in SrS . The trend does not extend to the case of $\text{BaS}:\text{Ce}$, which emits green light. [82] This has been attributed to the variation in the extent of covalency experienced by the Ce $5d$ orbitals in the host materials. [83] $\text{SrS}:\text{Ce}$ ACTFEL devices have demonstrated good luminous efficiency at 2 lm/W, but the emission is bluish-green. [84] Blue emitting ACTFEL devices can be realized with Ce in the host $(\text{Sr},\text{Ca})\text{Ga}_2\text{S}_4$, but the luminous efficiency is reduced to ~ 0.025 lm/W. [85]

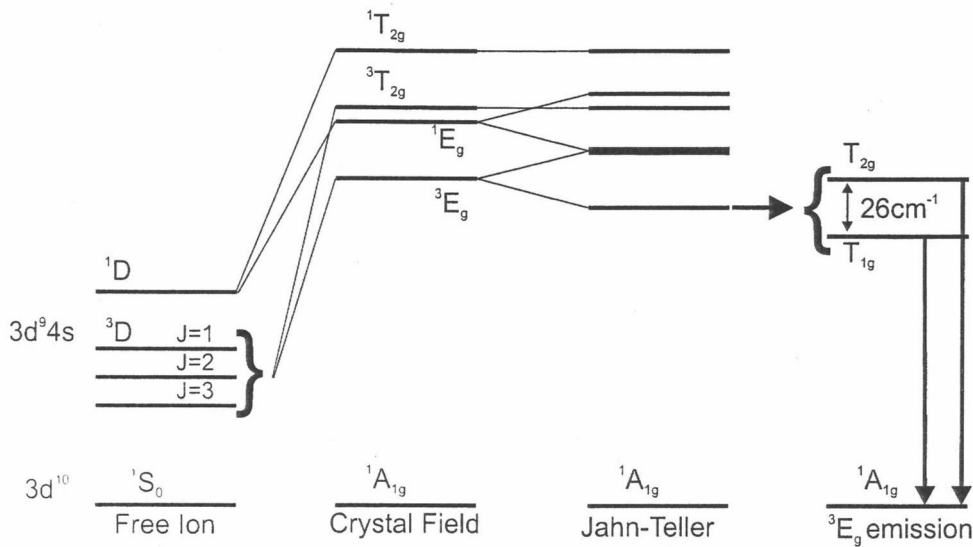


Figure 3.3: Cu^+ energy levels in an alkali halide host. Shown, from right to left, are: free-ion levels, the energy shift due to the crystal-field, Jahn-Teller distortion, and spin-orbit splitting of the lowest level (emitting states). (not to scale)

3.3.3 Cu^+

When considering optical absorption and emission within a single ion or a group of ions in a solid, it is appropriate to treat an optical transition with a localized model, rather than a band model. [86] The localized model treatment leads to two possible mechanisms of luminescence for Cu^+ in SrS: donor-acceptor pair recombination or electronic transition in isolated Cu^+ ions. The former is the luminescence mechanism for $\text{ZnS}:\text{Cu}^+, \text{Cl}^-$. In ZnS type phosphors Cu^+ is incorporated as an acceptor with a donor impurity such as Cl^- or Al^{3+} . The emission originates from the transition of an electron from a donor level close to the edge of the conduction band (Cl^- or Al^{3+}) to an acceptor level that is above the edge of the valence band (Cu^+). This is not the mechanism of luminescence in $\text{SrS}:\text{Cu}^+$.

The luminescence of Cu^+ in SrS is attributed to the $3d^9 4s \rightarrow 3d^{10}$ electronic transition of an isolated ion. It is common to treat the $\text{SrS}:\text{Cu}^+$ system in the context of the crystal field model with $\text{NaF}:\text{Cu}^+$ serving as the model system. [87, 88, 89, 90]

The energy levels of NaF:Cu⁺ are attributed to transitions of the type $3d^9 4s \rightarrow 3d^{10}$ and are illustrated in Fig. 3.3. It is informative to examine the details of the energy level structure of the well studied NaF:Cu⁺ system since the crystal structure is similar to SrS, and the model should give insight into the emission mechanism of SrS:Cu.

When the Cu⁺ ion is incorporated into the NaF lattice, spectroscopic properties such as spectral positions, widths, and intensities of luminescence and absorption bands are considerably changed from those of gaseous free ions. [91] The 3D and 1D free ion levels are split by the octahedral crystal field into the E_g and T_{2g} components. The general increase in energy from free ion to crystal is due to the antibonding interaction of the Cu⁺ 4s orbital with the anions. [92] The additional splitting of the E_g states is caused by dynamic Jahn-Teller distortion. The E_g levels are further split by spin-orbit coupling, where T_{1g} and T_{2g} levels arise from the 3E_g state.

The crystal field effect is the effect of the potential V induced by the surrounding anions on an electron of the Cu⁺ cation and is expressed in the form

$$\langle \Psi_{nlm} | V | \Psi_{nlm} \rangle . \quad (3.7)$$

The potential V is determined from an expression of the form

$$V = \sum_i \frac{Ze^2}{|R_i - r|}, \quad (3.8)$$

where R_i represents the position of the i^{th} anion, r the position of the outer electron, and Z the valence of the anions. The magnitude of the crystal field is dependent on the geometric size and symmetry of the site. Utilization of group theory is useful for obtaining energy level splitting and wavefunctions, calculating level energies, and predicting the selection rule for transitions between energy levels. As the size of the site onto which the luminescent ion is incorporated decreases, the crystal field increases and the energy level shift increases, resulting in optical transitions from the ground state to excited states at higher energies. For example, as the host lattice

is varied from BaS to SrS to CaS to MgS (decreasing cation size), the crystal field splitting of the $3d^9 4s$ states increases, and therefore the emission wavelength of Cu^+ shifts to shorter wavelengths (higher energies). [87]

The Jahn-Teller effect for localized centers is the outcome of a particular quantum mechanical interplay between electrons and atomic nuclei. The work of Jahn and Teller is one of the earliest applications of group theory in solid state physics. The effect is based on the assumption that the nuclear surroundings of an electronic system may have a high-symmetry configuration which is governed by a symmetry group. The basic argument relies on the reversal of the sign of the matrix elements if the nuclear displacements are replaced by their negatives and the instability of the zero displacement configuration. [93] The result of the Jahn-Teller effect on the Cu^+ energy levels is another splitting of the energy levels in addition to the crystal-field splitting.

The final alteration to the energy levels in Fig. 3.3 is due to spin-orbit interaction. The spin-orbit splitting arises from the interaction of the 3E_g state with the $^1T_{2g}$ and $^3T_{2g}$ states,

$$E_{L,2S+1}^{S.O.} = \langle ^{1,3}T_{2g} | (L \cdot S) | ^3E_g \rangle. \quad (3.9)$$

The result of this spin-orbit interaction is the splitting of the 3E_g state into the T_{2g} and T_{1g} components. These two spin-orbit components T_{2g} and T_{1g} are the emitting levels of the 3E_g state.

The $3d^9 4s \rightarrow 3d^{10}$ electronic transitions in the free Cu^+ ion are parity- and J-forbidden but become partially allowed in the crystal by electron-lattice interaction. The two transitions $^1A_{1g} \rightarrow ^1E_g$ and $^1A_{1g} \rightarrow ^1T_{2g}$ are spin allowed. Following the absorption of energy by the $^1A_{1g} \rightarrow ^1E_g$ or $^1A_{1g} \rightarrow ^1T_{2g}$ transition, the energy relaxes to the lowest emitting levels and thermal equilibrium is achieved. The $T_{2g}(^3E_g)$ state acquires a 1-2% singlet character through the spin-orbit coupling with $^1T_{2g}$. The $T_{2g}(^3E_g)$ level cannot interact with the singlets of the $3d^9 4s$ state. Therefore the emission rate of the lowest $T_{1g}(^3E_g)$ excited state is much weaker than that of the

$T_{2g}(^3E_g)$ state. The decays are interpreted in the context of a three-level system consisting of a ground state $^1A_{1g}$ (level 1) and two close thermalized metastable excited states, the lifetime of the lowest one (level 3) being much longer than the upper one (level 2). The following relations for the fast τ_f and slow τ_s components of the emission process can be found. [94]

$$\tau_f^{-1} \approx p_{23} + p_{32} \quad (3.10)$$

$$\tau_s^{-1} \approx \frac{A_{31} + A_{21} \exp(-\frac{\epsilon}{kT})}{1 + \exp(-\frac{\epsilon}{kT})} \quad (3.11)$$

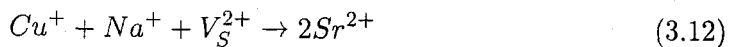
where A_{ij} is the radiative probability and p_{ij} the radiationless probability between two levels i and j . ϵ is the energy separation between the two excited states and has been found experimentally to be $\sim 26 \text{ cm}^{-1}$ in NaF. [94, 95] To explain the temperature dependence of the lifetime and assign the two bands in the emission spectra at room temperature, Moine and Pedrini propose that a strong Jahn-Teller distortion exists in this state. This three level emission model has been investigated in SrS:Cu^+ by Li *et al.* [89]

Like NaF, SrS also has the face-centered cubic rock-salt crystal structure and is characterized by high ionicity. The model for Cu^+ emission in NaF can be applied to SrS:Cu as well. Three different emission bands have been observed in SrS:Cu : intense bands at 470 nm and 520 nm, and a weaker feature at 545 nm. [87, 88, 90, 96] The appearance of a specific band depends on the concentration of Cu, the presence of codopants, preparative conditions, and temperature. Blue luminescence is observed in lightly doped samples, while similar samples with more heavy doping emit green light. [88] The shift in color from blue to green with decreasing temperature has been attributed to Cu^+ occupying an off center position in the sulfur octahedron, which moves to the center with decreasing temperature. [87]

Various explanations have been proposed to explain the emission mechanism of SrS:Cu^+ . Laud and Kulkarni attribute the differing green and blue emission to interstitial and substitutional sites, respectively, in SrS. [96] They also assign a 548

nm emission to a transition from the conduction band to the Cu center and a 520 nm emission from the Cu center to the valence band. Yamashita's group proposes a model based on PL emission from SrS:Cu at 80 K. The highest energy band, peaking at 513 nm, is assigned to emission from isolated Cu^+ centers in substitutional sites (monomer), while the next highest transition at 543 nm is attributed to paired Cu^+ (dimer). [88] Longer wavelength emission bands are assigned to highly aggregated Cu^+ centers. The structure of the dimer and aggregated centers is not presented, and the relation to the blue emission at room temperature is not clear.

A simplified model based on the defect chemistry is proposed by Li and collaborators. [90, 97, 98] In a SrS host, a monovalent Cu^+ ion impurity is substituted for a Sr^{2+} ion, which is divalent. There is a deficiency of positive charge that can be compensated by the formation of S vacancies or the incorporation of other charge compensating ions.



The latter two cases should lead to a Cu ion sitting on an octahedral Sr site, while the former case should lead to a Cu site having a reduced coordination number (i.e. less than 6 nearest neighbors). Li *et al* attribute the blue emission to Cu^+ occupying a Sr substitutional site with the retention of an approximate octahedral environment, and the green emission to a Cu^+ ion on a site near a S vacancy, having a reduced coordination number. Based on this model, the emission spectra of SrS:Cu,Cl and SrS:Cu,Na in Fig. 3.4 can be explained. [97]

SrS:Cu films co-doped with Cl show a strong blue emission with a peak wavelength at ~ 480 nm. Based on Li's model, this emission is attributed to Cu^+ centers in a 6-coordinated octahedral site. Equation 3.13 shows how the incorporation of Cl^- into S^{2-} sites compensates for the deficiency produced by introducing Cu^+ onto

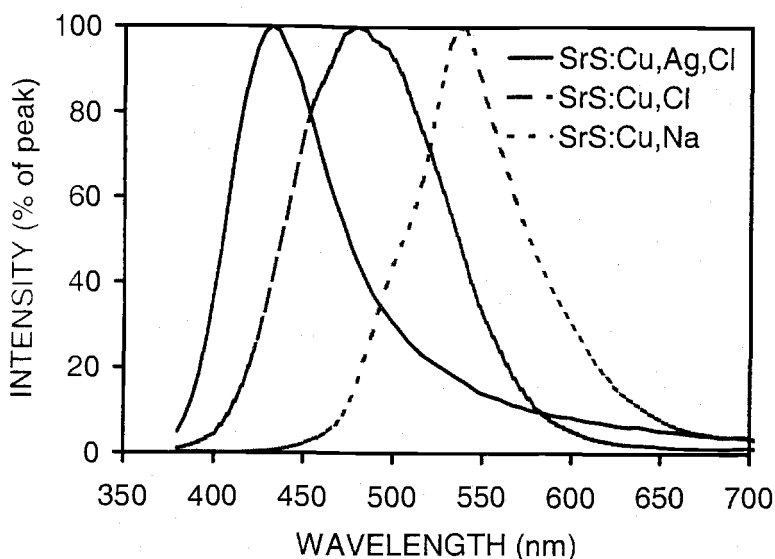


Figure 3.4: Electroluminescence spectra of SrS:Cu,Ag,Cl; SrS:Cu,Cl; and SrS:Cu,Na ACTFEL devices.

Sr^{2+} sites. Thus the formation of S vacancies is suppressed and the higher energy blue emission is dominant. This is also achieved by the substitution of a trivalent cation such as Ga^{3+} in conjunction with Cu^+ . Charge compensation of Cu^+ with a trivalent cation or a monovalent anion in the SrS host preserves the six-coordinated environment for the Cu^+ ion, leading to a blue emission.

The introduction of Na^+ into the SrS:Cu system leads to the formation of S vacancies, as shown in Eq. 3.12. The observed emission from SrS:Cu,Na is a saturated green at a wavelength of ~ 530 nm. In this case, the addition of a monovalent cation in addition to Cu^+ is intended to increase S vacancies. A reduced coordination number, probably 5, results for the Cu^+ ions and green emission is observed.

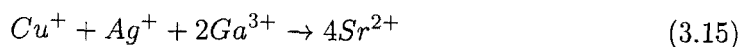
The difference in emission energy between green and blue SrS:Cu is $\sim 2000 \text{ cm}^{-1}$ (~ 50 nm). A shift of this magnitude could be attributed to a difference in the crystal field and/or a difference in the Jahn-Teller effect between the 5- and 6-coordinated

Cu^+ sites. It is likely that this is too large of a shift to be due to a difference in the spin-orbit components of the emitting energy level.

It should be noted here that the decay time has been observed to be much shorter in blue- than in green-emitting SrS:Cu . [88, 89, 90] This can be simply explained by the energy dependence of the radiative decay rate, as follows. The lifetime τ of a state is proportional to the square of the emission wavelength ($\tau \propto \lambda^2$). Blue light, having a shorter wavelength than green light, therefore has a shorter lifetime and faster decay rate.

The SrS:Cu,Ag system emits a deep blue color light. The emission mechanism is less understood than that for the SrS:Cu system. The deep blue emission is likely from a Ag^+ center, but Cu^+ plays a role in the emission as well. The Ag^+ contributes to the blue emission of the phosphor, but the SrS:Ag system itself does not produce light as intensely as SrS:Cu,Ag . An energy transfer model from Cu^+ to Ag^+ has been proposed but the viability of this model is questionable due to the fact that the emission energy in SrS:Cu (470 nm) is lower than that in SrS:Cu,Ag (430 nm). [99] It has also been suggested that the 430 nm emission in SrS:Cu,Ag is due to the formation of Ag^+-Ag^+ and Cu^+-Ag^+ pairs, based on analysis of the decay times over a wide temperature range. [89] It is interesting that the Ag^+-Ag^+ pair emission is not efficient in EL when the Cu is not present.

The defect chemistry of the Li model still applies to the SrS:Cu,Ag system, and the charge compensation mechanism of Eq. 3.15 preserves the sixfold coordination of the Cu^+ and Ag^+ centers.



Without the presence of Ga^{3+} for charge compensation, green emission occurs. This model would seem to suggest the emission mechanism of blue light in SrS:Cu,Ag is through isolated Ag^+ centers and not Ag^+-Ag^+ pairs. Whether or not Cu-Ag and Ag-Ag pairs are involved in the blue shift in SrS:Cu^+ with the addition of Ag^+ remains to

be determined. Currently, there is a lack of information regarding the SrS:Ag system and the relevance of the presence of Ga^{3+} in this system.

3.3.4 Eu^{2+}

Another luminescent impurity ion encountered in the exploration of full-color ACTFEL is Eu^{2+} . The emission energy of divalent Eu varies from UV to red depending on the host material. Eu^{2+} usually gives broad band emission due to the transition between the $4f^65d^1$ excited state to the $4f^7$ ground state. Like Ce^{3+} , the transition is allowed, resulting in a decay time of $\sim 1 \mu\text{s}$, and the excited state is split by the crystal field of the host, resulting in the host lattice dependence of the emission color. With increasing crystal field, the splitting of the $4f^65d^1$ state increases, so the emitting transition produces emission with lower energy and longer wavelength. [100] For weak crystal fields, the splitting is so small that the lowest level of the $4f^65d^1$ state lies above the $^6\text{P}_{7/2}$ level of the $4f^7$ configuration, and sharp line emission occurs due to the $f \rightarrow f$ transition, as shown in Fig. 3.5. [101]

The crystal field of the alkaline-earth sulfides causes emission from Eu^{2+} to occur in the red end of the visible spectrum. Emission from $\text{CaS}:\text{Eu}^{2+}$ ACTFEL devices is deep red with a peak near 650 nm. As the crystal field decreases with increasing cation size, the emission blue shifts, with $\text{SrS}:\text{Eu}^{2+}$ and $\text{BaS}:\text{Eu}^{2+}$ producing peaks around 615 nm and 570 nm, respectively. The emission of Eu^{2+} is further blue shifted in alkaline-earth thiogallate host materials. $\text{SrGa}_2\text{S}_4:\text{Eu}^{2+}$ is a green emitting phosphor with a broad spectrum centered at 532 nm. ACTFEL devices producing saturated blue emission have been realized with the phosphor $\text{BaAl}_2\text{S}_4:\text{Eu}^{2+}$, with an emission peak at 471 nm and CIE coordinates of $x = 0.10$ and $y = 0.12$. [102]

3.4 Conclusion

This chapter reviews issues relevant to the development of ACTFEL materials and devices. The chapter begins with a discussion of the requisite properties of the

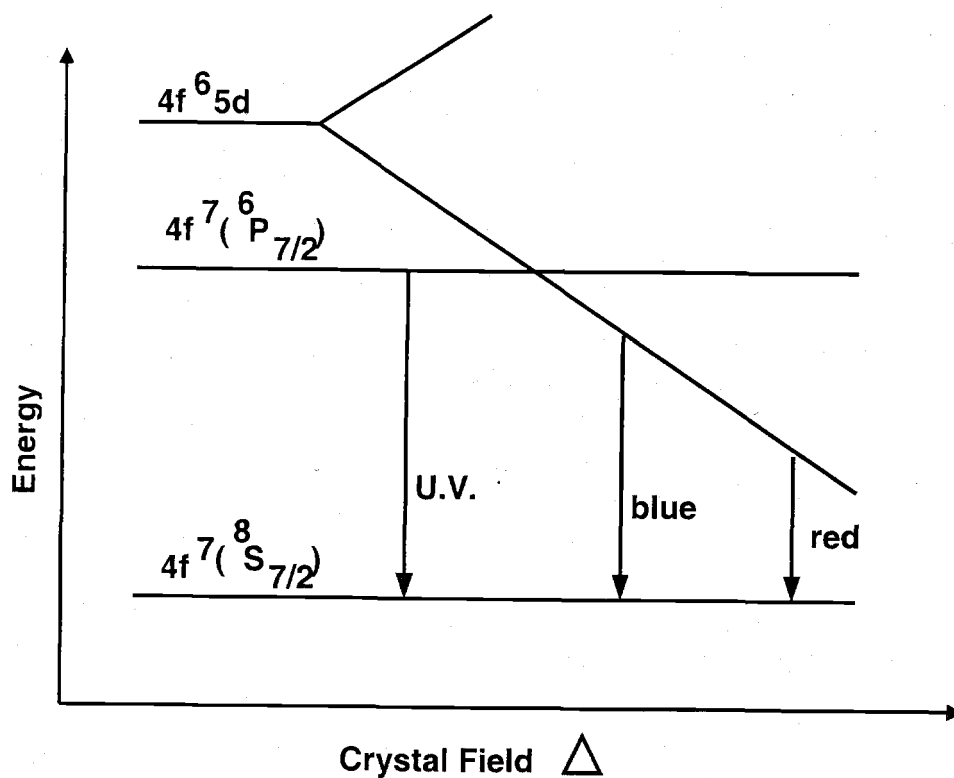


Figure 3.5: Eu^{2+} energy level diagram showing energy level splitting as a function of crystal field strength.

materials employed to build ACTFEL devices. Then various techniques utilized to deposit the thin-films are examined. Finally, the essentials of luminescent impurities commonly found in ACTFEL research are presented.

4. ACTFEL PHOSPHOR FABRICATION

The advancement of ACTFEL technology is dependent on the development of new processing techniques and new phosphor materials. This chapter is concerned with developing various approaches to achieving bright and efficient primary color phosphors for ACTFEL applications. The phosphor materials explored here are exclusively sulfides due to the superiority of sulfides as thin-film electroluminescent phosphors. First, a new approach to doping atomic layer epitaxy (ALE) phosphor films for ACTFEL device applications is examined. Then, various phosphors prepared by electron-beam evaporation are canvassed.

4.1 Source layer diffusion doping of ALE thin-film phosphors

The ALE deposition method of has been successfully employed in the fabrication of ZnS:Mn and SrS:Ce ACTFEL devices. [103] One of the drawbacks of the ALE deposition method is the effort required to develop suitable precursor gases. This has been especially true in the development of a precursor suitable for doping SrS with Cu. An alternate method for doping ALE thin-film SrS and CaS phosphor hosts is Cu doping via diffusion from a thin source layer, termed source layer diffusion doping (SLDD). SLDD was recently employed successfully in electron-beam evaporated SrS. [104] This method has been extended to dope ALE SrS and CaS thin-films. Here, the viability of doping ALE thin-films via SLDD with various luminescent impurities is examined.

The SLDD method involves the diffusion of the desired luminescent impurity and co-activators from one or more source layers into an undoped phosphor host film. In the SLDD technique, the dopant is thermally diffused into the undoped host, as illustrated in Fig. 4.1. The processing steps for implementing this technique begin with deposition of an undoped MS phosphor host ($M=\text{Ca}, \text{Sr}$) by ALE. Precursor gases of $M(\text{thd})_2$ and H_2S are used in the ALE deposition process, as described in Sec. 3.2.4.

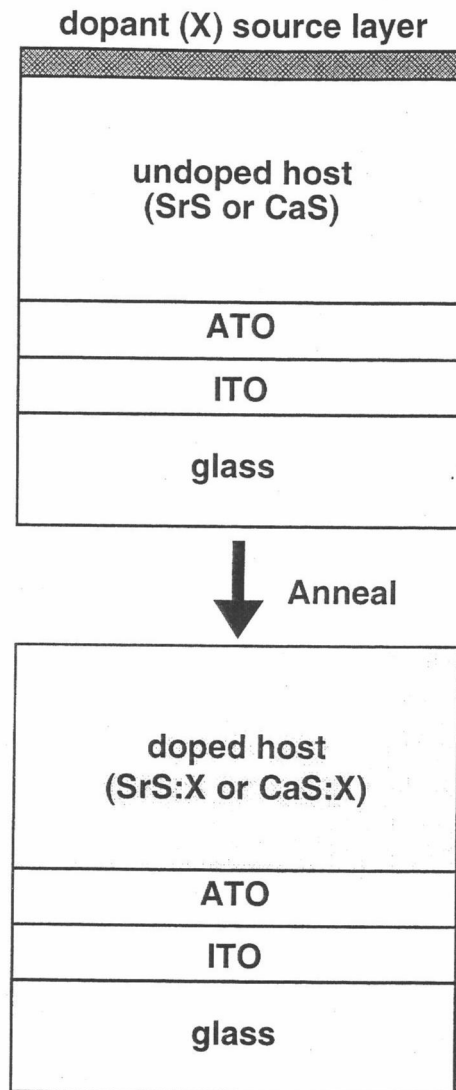


Figure 4.1: Depiction of the source layer diffusion doping (SLDD) process for dopant incorporation into an ALE ACTFEL phosphor host film.

Next, thin layers of the appropriate dopant species are thermally evaporated onto the host film. Rapid thermal annealing in an Ar atmosphere is then performed in order to diffuse the dopants into the phosphor host film and enhance the crystallinity of the phosphor. This technique makes possible the incorporation of dopants into a phosphor host film without the use of a precursor. If the desired dopant readily diffuses into the host film, the processing of ALE ACTFEL devices is simplified by eliminating the

often harrowing task of developing a dopant precursor with the proper chemistry for a thin-film process. This technique also takes advantage of the superior properties of ALE grown films, such as a significant degree of crystallinity as deposited and few pinhole defects. [77] The advantages of the ALE/SLDD process have the potential to lead to low temperature processing of ACTFEL phosphors suitable for commercial fabrication.

An advantage for ACTFEL devices processed by ALE/SLDD is the reduced temperature required during the anneal process. Evaporated and sputtered SrS films are typically annealed at 810°C. The electrical stability of the ALE SrS ACTFEL devices degrades significantly when annealed at temperatures above ~750°C, resulting in frequent burn-outs during electrical operation. It is found that the ideal RTA temperature for SLDD of Cu into ALE SrS is in the vicinity of 700°C.

4.1.1 Cu doping of ALE SrS

SrS:Cu has emerged as a bright and efficient phosphor for blue and green ACTFEL devices. [98, 105, 106, 107] The development of SrS:Cu ACTFEL displays for commercial use could be achieved using an ALE process. A major obstacle in the realization of an ALE SrS:Cu device has been the lack of a suitable Cu precursor. This section presents a process for Cu doping of ALE SrS for thin-film electroluminescent devices using SLDD. Methods of co-doping ALE SrS:Cu to produce blue and green emitting ACTFEL devices are also presented.

Beginning with an undoped SrS thin film deposited by ALE, the addition of Cu dopant is accomplished by thermal evaporation of a Cu-containing source, such as Cu₂S, CuCl₂, or CuF₂, followed by a rapid thermal anneal of the sample. Additional dopants are also sometimes incorporated into the phosphor by evaporating additional layers prior to the anneal step. A SrS:Cu phosphor is produced using SLDD by evaporating a layer of Cu₂S onto a SrS sample and annealing. Following the annealing step, a 200 nm SiO_xN_y top insulator is PECVD-deposited, followed

by thermal evaporation of 100 - 150 nm Al top electrodes. Figure 4.2 shows the EL emission spectrum from an ACTFEL device prepared by evaporating a 3 nm layer of Cu_2S onto an ALE SrS film approximately 900 nm thick and annealing for 150 s at 700°C in an Ar atmosphere. The emission from this non-coactivated SrS:Cu device is bluish-green in color with a peak at a wavelength 524 nm, with a broad shoulder in the blue region, yielding 1931 CIE coordinate values of $x=0.215$, $y=0.406$. The luminance from this device at 40 volts above V_{th} is $L_{40} \approx 12 \text{ cd/m}^2$ at 60 Hz.

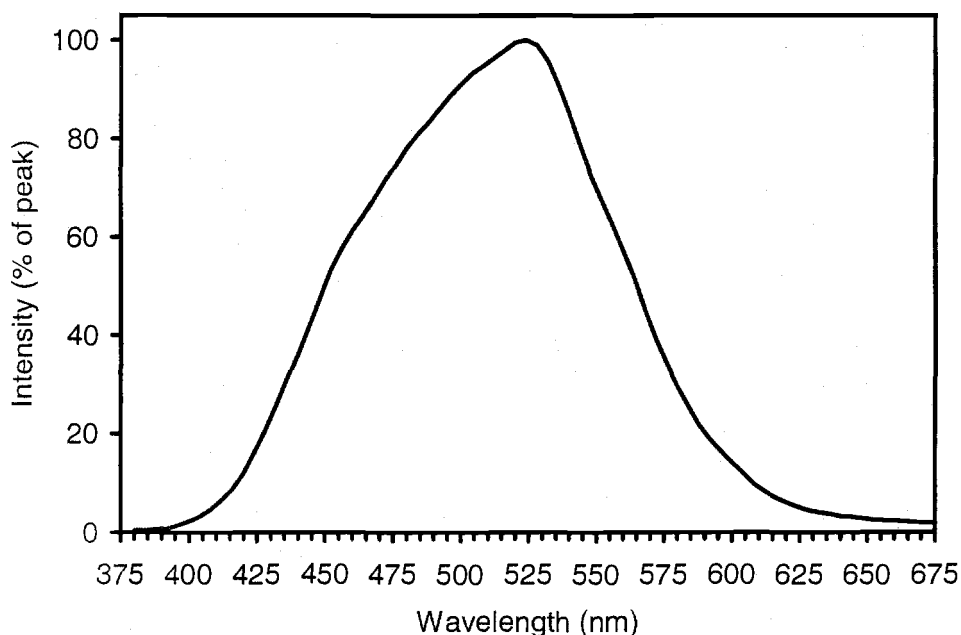


Figure 4.2: Electroluminescence emission spectrum for an ALE SrS film doped with Cu_2S via source layer diffusion doping.

The emission of SrS:Cu may be blue-shifted by incorporating Cl^- ions into the phosphor. This can also be accomplished by the SLDD process by evaporating any of a number of chloride compounds after the Cu_2S deposition. The Cl compound then diffuses into the SrS host along with the Cu atoms during the RTA step. Results of ALE/SLDD SrS:Cu coactivation with various Cl-containing compounds are given

in Table 4.1. Thicknesses on the order of 10 nm are used for each of the chloride materials. The decrease in luminance occurring with coactivator incorporation is due in some part to the color shift from bluish-green to blue because of the human eye's decreased sensitivity to blue light. This is the reason for the general trend of decreasing L_{40} values with increasing blue shift. The alkali chlorides KCl, NaCl, and LiCl produce a blue shift that increases with decreasing cation size. The luminance also increases with decreasing cation size, despite the corresponding increasing blue shift. As discussed in Section 3.3.3, Cl^- ions in SrS act to compensate for S vacancies, which increases blue emission from Cu^+ luminescent centers. The incorporation of K and Na has the effect of creating S vacancies, which enhances green emission from Cu^+ luminescent centers. [97, 98] In light of this, the fact that KCl and NaCl do not produce substantial blue shifts is not surprising. The use of Li in SrS:Cu, unlike K and Na, does not produce a red shift of the emission spectrum. It is likely that Li is not easily substituted into SrS, so the effect of Cl incorporation in the LiCl coactivated device is not cancelled out by the un-incorporated Li^+ cation species.

The coactivation of SrS:Cu with Ag has been found to produce a dramatic blue shift. [105, 106] Therefore, the incorporation of AgCl into the ALE/SLDD SrS:Cu phosphor is expected to produce a substantial blue shift from the emission shown in Fig. 4.2. The result of this particular study, shown in Table 4.1, is that AgCl coactivation alone does not produce the deep blue emission expected. This is likely due to a Ag concentration that is too large, or Ag segregation to grain boundaries. [108, 109] A more detailed study of AgCl coactivation is discussed below. The largest blue shift in this study is produced by coactivating Cu_2S doped ALE SrS with YCl_3 . Both Y^{3+} and Cl^- provide compensation for Cu^+ , thus reducing the S vacancy concentration, resulting in blue emission from SrS:Cu $^+$. The YCl_3 -doped CIE color coordinates of 0.156, 0.251 and peak emission wavelength of 472 nm are slightly blue-shifted relative to the "standard" SrS:Cu CIE chromaticity of $x=0.16$, $y=0.28$, but are not saturated blue. This result is supportive evidence that the defect

Table 4.1: The effect of Cl containing co-activators on the EL properties of SrS:Cu prepared by the ALE/SLD process.

Co-activator	L_{40} (60 Hz) (cd/m ²)	λ_{peak} (nm)	CIE _x	CIE _y
none	12	524	0.215	0.406
KCl	2.2	504	0.193	0.359
NaCl	5.1	496	0.185	0.322
LiCl	7.4	492	0.172	0.312
AgCl	6.1	484	0.179	0.290
SrCl ₂	4.8	484	0.165	0.285
YCl ₃	4.1	472	0.156	0.251

chemistry model proposed by Li (Sect. 3.3.3) is applicable for ALE SrS:Cu ACTFEL devices.

Another implication of the coordination theory of Li *et al* is that saturated green emission from SrS:Cu may be obtained by Na and K coactivation. High quality green SrS:Cu ACTFEL devices have been produced by electron-beam evaporation using NaF and KF coactivation. [98, 104] Doping of ALE SrS with Cu₂S and NaF by SLDD is accomplished by evaporating thin layers of Cu₂S and NaF onto ALE SrS films and performing a 700°C RTA in Ar. The dependence of device operation on Cu₂S concentration is studied by fabricating devices with varying Cu₂S layer thickness. A NaF layer with thickness of ~1.5% of the ALE SrS thickness is deposited on top of the Cu₂S layer. The SrS layer thickness in this study is ~650 nm. After annealing, a 200 nm SiO_xN_y insulator and Al contacts are deposited to complete the device. The results of the Cu₂S concentration study are given in Table 4.2. The optimum concentration is found to be 1.2%, which is the maximum concentration used in this

Table 4.2: The effect of Cu concentration on the operation properties of SrS:Cu,Na ACTFEL devices prepared by the ALE/SLDD process with a 650 nm thick phosphor and NaF layers with thickness $\sim 1.5\%$ of the phosphor thickness.

thickness (% Cu ₂ S)	L ₄₀ (60 Hz) (cd/m ²)	η_{40} (lm/W)	V _{th} (V)	λ_{peak} (nm)	CIE x	CIE y
0.15	30.4	0.29	160	544	0.303	0.595
0.45	44.2	0.48	160	536	0.336	0.582
0.60	40.6	0.47	156	548	0.322	0.583
1.20	49.5	0.57	154	544	0.322	0.577

study. This concentration results in saturated green electroluminescence with L₄₀ and η_{40} values of ~ 50 cd/m² and 0.57 lm/W. A L-V/ η -V plot of this device is shown in Fig. 4.3. The optimum concentration of 1.2% Cu₂S is unexpected, since the optimum Cu concentration in SrS:Cu ACTFEL devices prepared by other techniques is much less than 1%.

Rather than co-activating a Cu₂S doped SrS film with Cl from another source layer to obtain blue EL, Cl and Cu may be introduced together from a CuCl₂ source layer. In this manner, blue SrS:Cu,Cl ACTFEL devices are prepared by evaporating a CuCl₂ layer onto the ALE SrS layer followed by a rapid thermal anneal in Ar at a temperature of 700°C. The thickness and evaporation rate of the CuCl₂ is monitored with a quartz crystal thickness monitor. A CuCl₂ evaporation rate of ~ 0.5 Å/s is used. The substrate is not heated during deposition. The use of CuCl₂ as a Cu source produces a blue shift from the ALE/SLDD SrS:Cu samples prepared with Cu₂S, as shown in the SrS:Cu,Cl spectra in Fig. 4.4. At 40 V above V_{th}, a luminance and luminous efficiency of 14.1 cd/m² and 0.11 lm/W are obtained, as shown in Fig. 4.5.

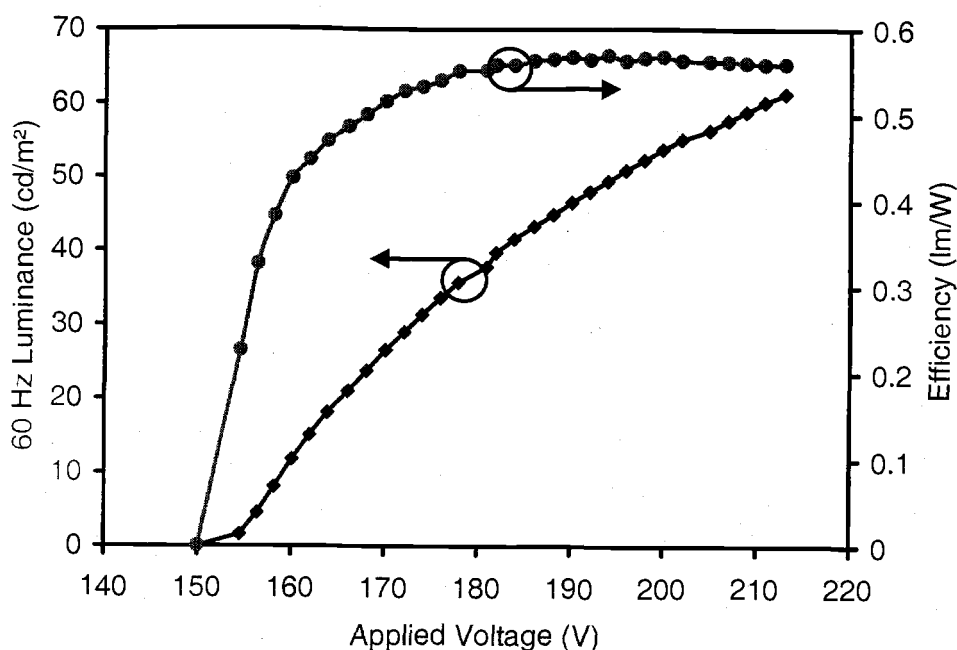


Figure 4.3: L-V and η -V curves for a 650 nm thick ALE SrS ACTFEL device doped with 1.2% Cu_2S and 1.5% NaF via source layer diffusion doping.

The concentration of CuCl_2 in the phosphor is easily changed by varying the thickness of CuCl_2 deposited prior to annealing. The results of varying the thickness of the CuCl_2 layer are given in Table 4.3. The luminance, luminous efficiency, and emission wavelength all increase with the thickness of the CuCl_2 layer up to 0.75 %, while V_{th} decreases. The decrease in V_{th} with CuCl_2 concentration is attributed to an increase in phosphor space charge density with Cu^+ and Cl^- dopant concentration. Above the concentration of 0.75 % CuCl_2 , the luminance and luminous efficiency decrease considerably from their maximum optimum values. The L-V curve tends to smear out around V_{th} with increasing CuCl_2 layer thickness, as shown in Fig. 4.6. This could be due to the effects of the CuCl_2 layer on the phosphor/insulator interface or to the considerable amount of Cl^- donors being incorporated into the SrS phosphor layer.

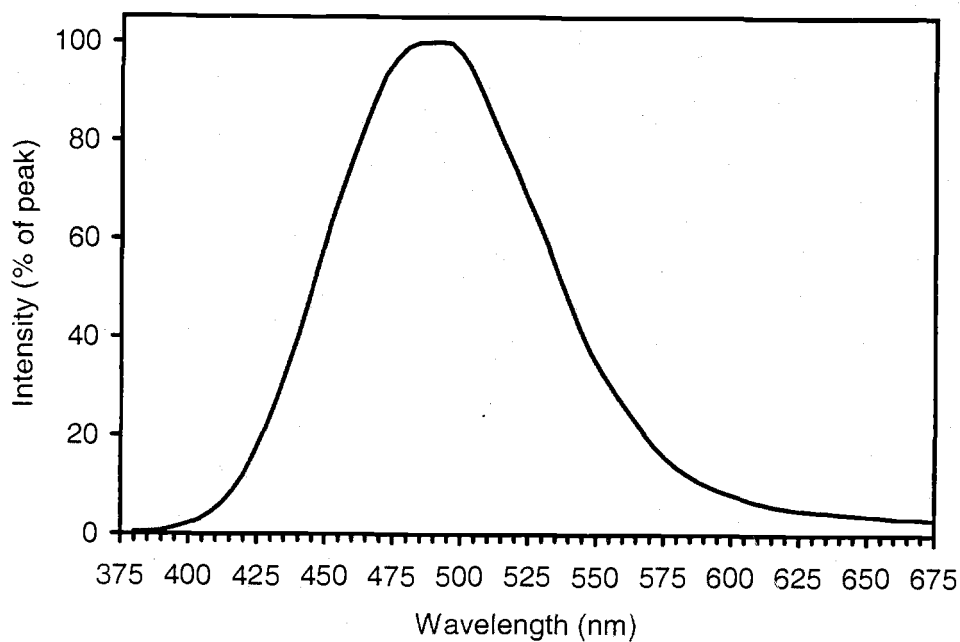


Figure 4.4: EL emission spectra for a 1000 nm ALE/SLDD SrS:Cu,Cl ACTFEL device prepared using a CuCl_2 concentration of 0.75%.

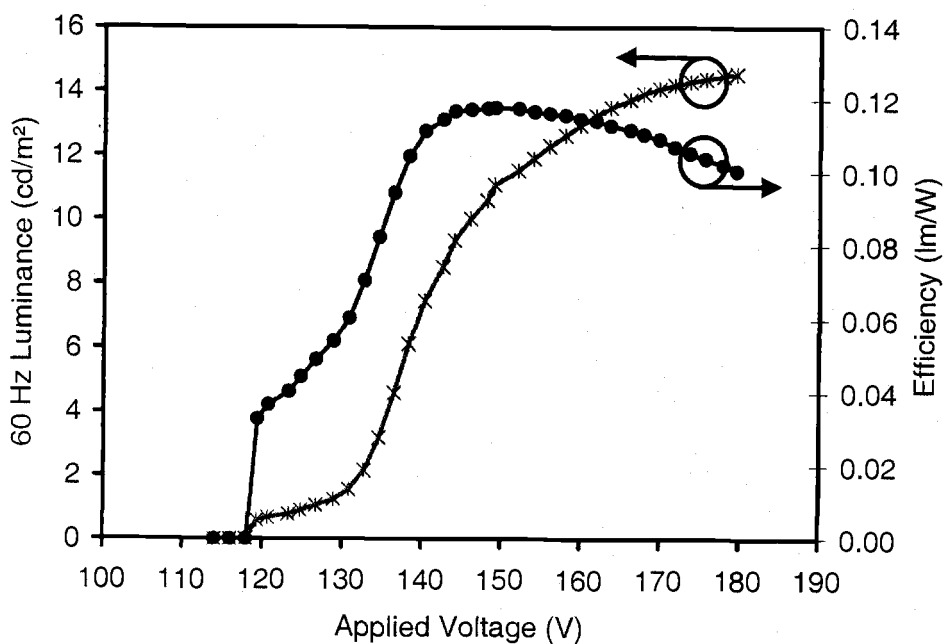


Figure 4.5: L-V and η -V curves for a 1000 nm thick ALE SrS ACTFEL device doped with 0.75% CuCl_2 via source layer diffusion doping.

Table 4.3: The effect of CuCl_2 concentration on the operation properties of $\text{SrS}:\text{Cu},\text{Cl}$ ACTFEL devices prepared by the ALE/SLDD process with a 1000 nm thick phosphor.

thickness (% CuCl_2)	L_{40} (60 Hz) (cd/m^2)	η_{40} (lm/W)	V_{th} (V)	λ_{peak} (nm)	CIE x	CIE y
0.15	3.57	0.021	140	468	0.160	0.214
0.25	9.94	0.064	136.5	472	0.159	0.248
0.50	10.15	0.075	134	492	0.173	0.301
0.75	14.1	0.11	130	492	0.176	0.311
1.0	7.66	0.075	142	492	0.174	0.302
1.5	6.93	0.087	112	484	0.174	0.305
2.5	4.67	0.045	126	484	0.172	0.299

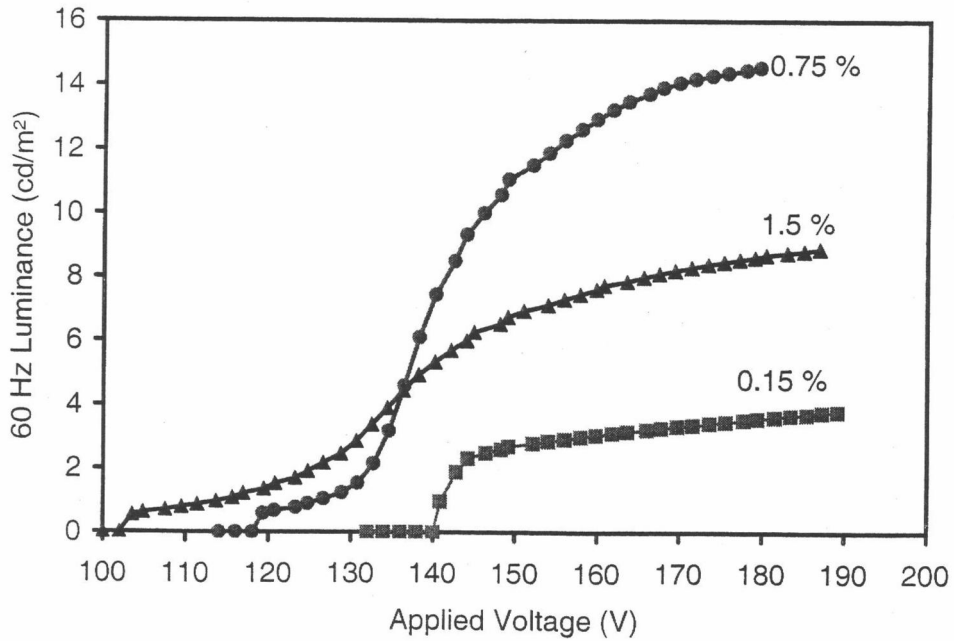


Figure 4.6: L-V and η -V curves for a 1000 nm thick ALE SrS ACTFEL device doped with 0.15%, 0.75%, and 1.5% CuCl_2 via source layer diffusion doping.

Blue SrS:Cu,Ag,Cl phosphors are fabricated by depositing a layer of AgCl in addition to the CuCl₂ layer. The SrS:Cu,Ag,Cl CIE color coordinates are closer to those of an ideal blue, with CIE color coordinates of $x=0.19$, $y=0.14$, but the luminance decreases to $L_{40} = 1.7 \text{ cd/m}^2$. It is interesting to note that the blue shift due to Ag incorporation occurs when CuCl₂ is used as the Cu source layer, but not when Cu₂S is used, as shown above. This is true even when Cl is available from the AgCl source layer. The color of emission is dependent on the CuCl₂ and AgCl₂ concentration. A large amount of AgCl is required, while a very low CuCl₂ concentration ($\sim 0.1\%$) is necessary to obtain deep blue emission. Table 4.4 shows the results of varying CuCl₂ and AgCl thickness on the EL emission. For a 0.1% CuCl₂ thickness, a transition to deep blue emission is observed as the AgCl thickness increases from 0.3% to 1.1%. With thicker CuCl₂ layers, a blue shift is not observed. With more CuCl₂, thicker AgCl layers than those used are required to produce the Ag/Cu ratio necessary in order to obtain deep blue emission. Figure 4.7 shows the emission spectrum from an ALE/SLDD SrS:Cu,Ag,Cl ACTFEL device prepared using 0.1% CuCl₂ and 2.3% AgCl. The emission peaks at 436 nm, with a large tail extending well into the red portion of the visible spectrum. The red emission in the tail increases the CIE coordinate values from what would be saturated blue color coordinates to the values given in Table 4.4.

It is unlikely that the entire amount of Ag present in the AgCl source layer is incorporated into the phosphor film, since the optimal Cu and Ag concentrations have been found to be less than the concentrations used here. [108] The addition of a AgCl layer adversely affects the turn-on properties, as evidenced in the Q - F_p curves shown in Fig. 4.8. The curves shown in Fig. 4.8 are taken at the same voltage on a device where a 0.2% thick AgCl layer is deposited onto one half side of an ALE SrS sample following evaporation of a 0.75% thick CuCl₂ layer on the entire sample. The turn-on transition of the SrS:Cu,Ag,Cl side of the device is more gradual than on the side of the device without AgCl, as seen in the significant amount of conduction charge

Table 4.4: The effect of CuCl_2 and AgCl concentration on the emission properties of $\text{SrS}:\text{Cu},\text{Ag},\text{Cl}$ ACTFEL devices prepared by the ALE/SLDD process.

thickness (% CuCl_2)	thickness (% AgCl)	L_{40} (60 Hz) (cd/m^2)	λ_{peak} (nm)	CIE x	CIE y
0.1	0.1	5.87	472	0.177	0.262
0.1	0.2	2.04	472	0.187	0.273
0.1	0.3	2.22	452	0.168	0.208
0.1	1.1	1.05	432	0.177	0.201
0.1	1.7	1.07	432	0.183	0.202
0.1	2.3	1.48	436	0.190	0.143
0.4	0.6	13.3	500	0.196	0.347
0.75	0.05	5.69	496	0.182	0.325
0.75	0.2	4.19	496	0.194	0.334
0.75	0.4	2.59	496	0.204	0.330

at low phosphor fields. In the $\text{SrS}:\text{CuCl}_2$ device, when the internal charge begins to flow, the field abruptly stops increasing and is clamped at ~ 1.1 MV/cm. In the device containing AgCl , charge begins to flow across the phosphor prior to the onset of field clamping, while the phosphor field continues to increase. This is attributed to some fraction of the AgCl layer not diffusing into the SrS layer and remaining near the top interface, obfuscating the interface state distribution and therefore the injection properties and the turn-on characteristics. The AgCl remaining near the interface could be thought of as a thin metal layer between the SrS and the top SiO_xN_y insulator. This metal interface layer creates a multitude of shallow states, resulting in internal charge that begins conducting at low phosphor fields. The shallow states

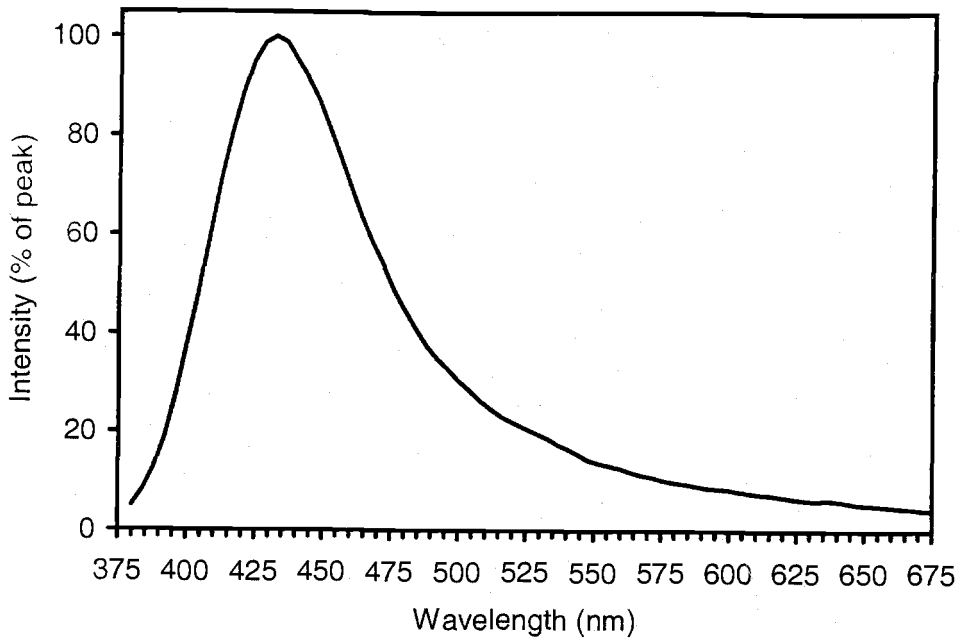


Figure 4.7: Electroluminescence emission spectrum for an ALE SrS ACTFEL device doped with CuCl_2 and AgCl via source layer diffusion doping.

also cause the charge collapse observed in the Q - F_p curve for the SrS:Cu,Ag,Cl device. It is also possible that excess Cl species remain near the top interface, and create a multitude of shallow donor states.

The effects of the AgCl layer are also seen in Q_{max} - V_{max} curves, as shown in Fig. 4.9. Below threshold, more charge is transferred in the SrS:Cu,Ag,Cl device than in the SrS:Cu,Cl device. The emission of electrons from shallow interface states created by the AgCl layer begins at a low voltage, causing an increase in transferred charge below threshold. If the AgCl layer completely diffuses into the SrS layer, there would not be any shallow state emission below threshold. The addition of AgCl to SrS:Cu,Cl also causes an increase in V_{th} by ~ 10 V, a decrease in Q_{max} - V_{max} overshoot, and a decrease in above threshold transferred charge.

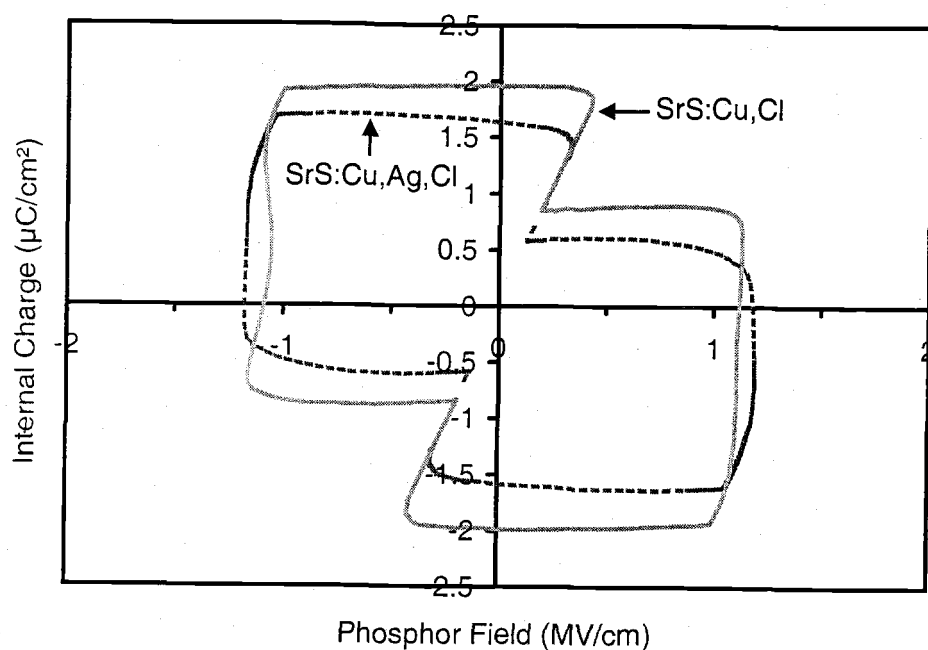


Figure 4.8: Internal charge - phosphor field curves for ALE SrS ACTFEL devices doped with CuCl_2 and AgCl via source layer diffusion doping.

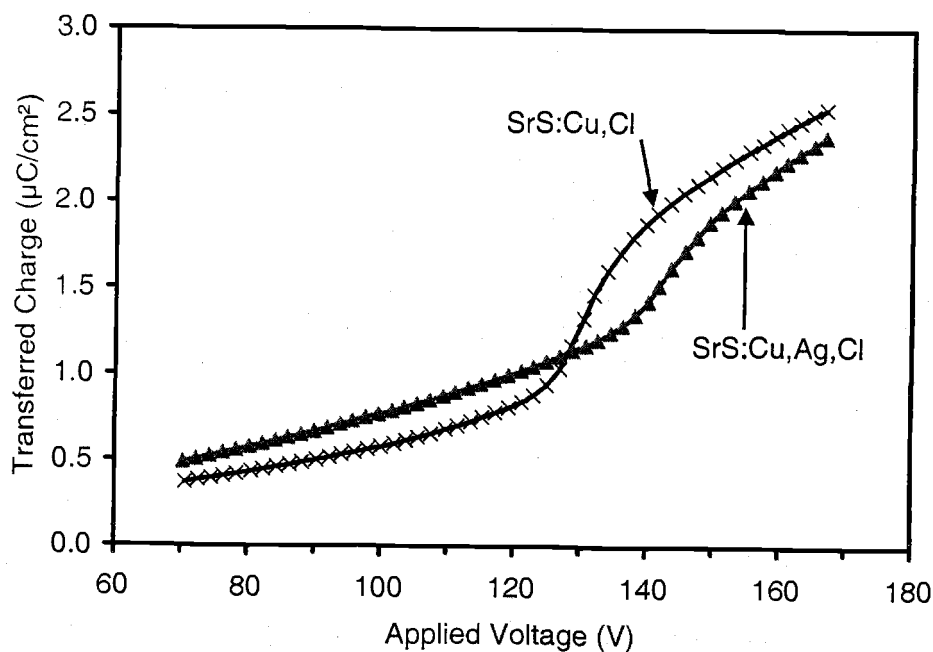


Figure 4.9: Q_{\max} - V_{\max} curves for ALE SrS ACTFEL devices doped with CuCl_2 and AgCl via source layer diffusion doping.

A significant improvement in luminance, efficiency, and color of the blue-emitting ALE/SLDD devices is obtained when a layer of GaF_3 is deposited in addition to the CuCl_2 and AgCl layers. Luminance and efficiency results for SrS:Cu,Cl,GaF_3 and $\text{SrS:Cu,Ag,Cl,GaF}_3$ are shown in Figs. 4.10 and 4.11, respectively. Using the optimum CuCl_2 thickness of 0.75% with a GaF_3 layer of 2.5% of the total phosphor thickness (i.e. 25 nm for a 1 μm SrS layer), the brightness and efficiency obtained for SrS:Cu,Cl,Ga are $L_{40} = 17.4 \text{ cd/m}^2$ and $\eta_{40} = 0.14 \text{ lm/W}$ at $\text{CIE}_x=0.157$ and $\text{CIE}_y=0.248$. The employment of the GaF_3 layer results in an improvement of $\sim 25\%$ in luminance and efficiency over the same device without GaF_3 , while the color is deeper blue ($\text{CIE } y=0.311$ without GaF_3). This result indicates that the effect of GaF_3 produces blue-emitting SrS:Cu in much the same way that NaF or KF produces green-emitting SrS:Cu .

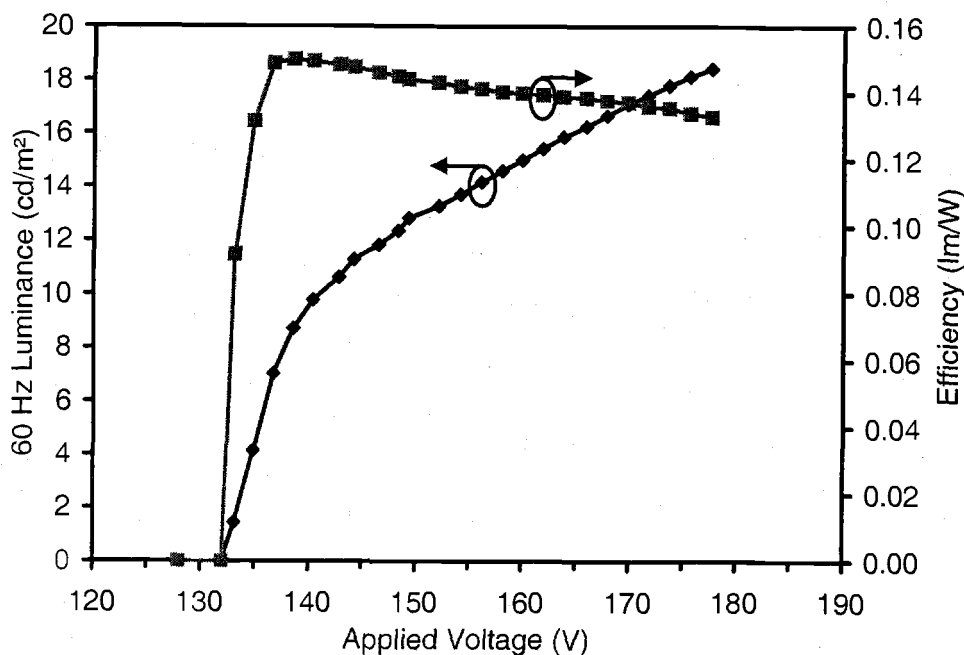


Figure 4.10: L-V and η -V curves for an ALE SrS ACTFEL device doped with CuCl_2 and GaF_3 via source layer diffusion doping.

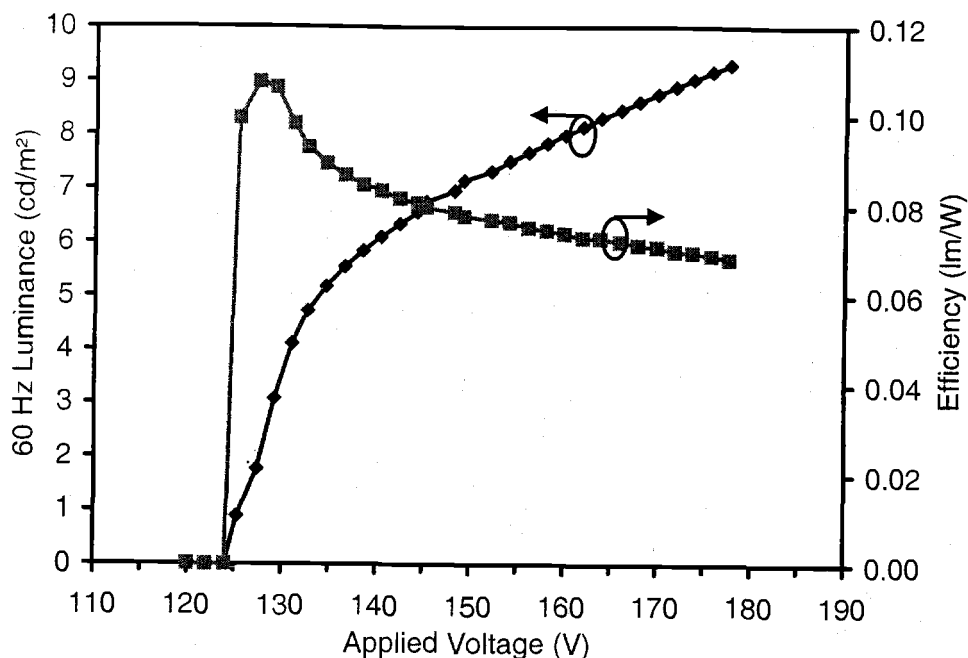


Figure 4.11: L-V and η -V curves for an ALE SrS ACTFEL device doped with CuCl_2 , AgCl , and GaF_3 via source layer diffusion doping.

While 2.3% AgCl is the optimum thickness for the deepest blue color without GaF_3 , a much thinner AgCl layer of only $\sim 0.2\%$ and a smaller Ag/Cu ratio is required to produce deep blue emission when a layer of GaF_3 is subsequently deposited. The ACTFEL emission values obtained for ALE/SLDD $\text{SrS}:\text{Cu}, \text{Ag}, \text{Cl}, \text{Ga}$ are $L_{40} = 8.3 \text{ cd/m}^2$ and $\eta_{40} = 0.072 \text{ lm/W}$ at $\text{CIE}_x = 0.165$ and $\text{CIE}_y = 0.166$. The emission peaks at a wavelength of 448 nm, as shown in Fig. 4.12. Notice in Fig. 4.12 that although the spectrum is red shifted relative to the spectrum for the $\text{SrS}:\text{Cu}, \text{Ag}, \text{Cl}$ device without GaF_3 (Fig. 4.7), the emission tail does not extend deep into the red portion of the spectrum. An increase in the AgCl concentration should produce the desired complete shift in emission to deep blue and saturated blue color coordinates. Note that deep blue emission is accomplished with a greater CuCl_2 thickness of 0.75% (i.e. a smaller Ag/Cu ratio). This is critical because a higher Cu concentration is desirable to increase luminance. Without GaF_3 , a deep blue emission was only possible with

a CuCl_2 thickness of 0.1%. The device structure with 0.75% CuCl_2 and 0.2% AgCl , without GaF_3 , gives CIE coordinates of $x=0.194$, $y=0.334$. Table 4.5 summarizes the effects of GaF_3 on the emission properties of SrS:Cu,Cl and SrS:Cu,Ag,Cl ALE/SLDD ACTFEL devices. Note that there has not been an attempt to optimize the CuCl_2 concentration when GaF_3 co-doping is employed. The optimum CuCl_2 thickness may also be different when AgCl co-doping is performed along with GaF_3 .

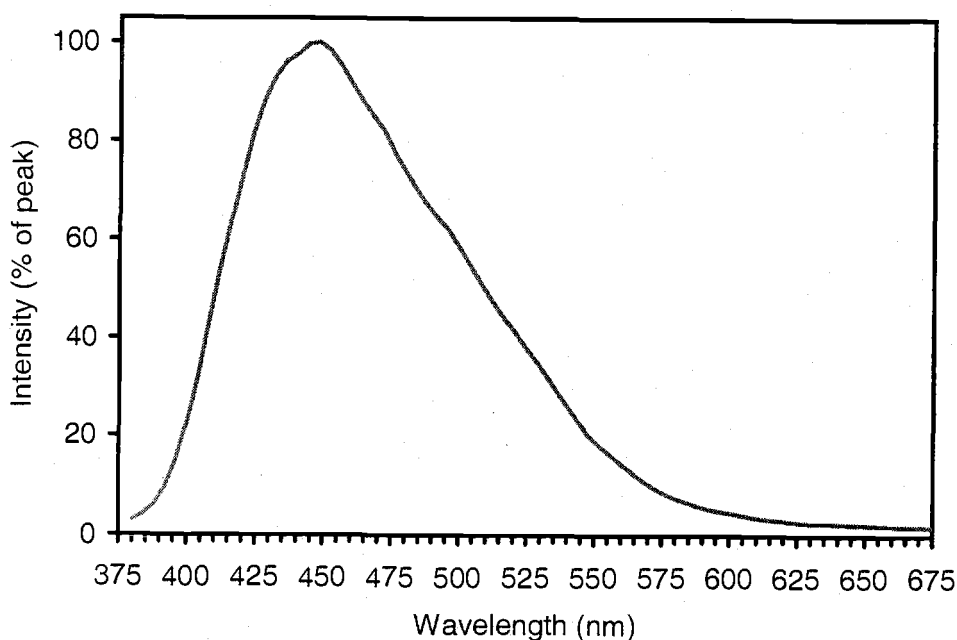


Figure 4.12: EL emission spectrum for an ALE SrS ACTFEL device doped with CuCl_2 , AgCl , and GaF_3 via source layer diffusion doping.

The addition of a GaF_3 layer has an interesting effect on the operation of SrS:Cu,Cl ALE/SLDD ACTFEL devices. The use of GaF_3 results in a reduction of below threshold conduction charge, as evident in the $Q_{\max}\text{-}V_{\max}$ curves in Fig. 4.13. Without GaF_3 , a significant amount of conduction charge is transferred below threshold, during the relaxation portion of the waveform, resulting in a below threshold slope of the $Q_{\max}\text{-}V_{\max}$ curve that is greater than C_{tot} . The slope of the $Q_{\max}\text{-}V_{\max}$ curve

Table 4.5: The EL emission characteristics of ~ 1000 nm ALE/SLDD SrS:Cu,Cl and SrS:Cu,Ag,Cl ACTFEL devices with and without GaF₃.

source layer thickness	L_{40} (60 Hz) (cd/m ²)	λ_{peak} (nm)	CIE x	CIE y
0.75% CuCl ₂	14.1	492	0.176	0.311
0.75% CuCl ₂ & 2.5% GaF ₃	17.4	476	0.157	0.248
0.75% CuCl ₂ & 0.2% AgCl	4.19	496	0.194	0.334
0.75% CuCl ₂ & 0.2% AgCl & 2.5% GaF ₃	8.3	448	0.165	0.166
0.1% CuCl ₂ & 2.3% AgCl	1.48	436	0.190	0.143

below V_{th} for the SrS:Cu,Cl,GaF₃ device is equal to the physical value of C_{tot} . The reduction in sub-threshold charge transfer with GaF₃ causes an increase in V_{th} , since the formation of polarization charge below threshold does not occur without charge transfer. If the sub-threshold conduction is caused by emission from shallow donor states in the bulk of the phosphor, a significant amount of space charge could build up and lower the value of V_{th} . There is also a reduction in the transferred charge above threshold with GaF₃ incorporation. The reduced transferred charge above threshold serves to lower the power consumption of SrS:Cu,Cl,GaF₃ ACTFEL devices and thus increase the efficiency. The elimination of sub-threshold conduction with GaF₃ also occurs in SrS:Cu,Ag,Cl ALE/SLDD ACTFEL devices.

Rather than performing an RTA anneal as the source layer diffusion doping step, traditional furnace or vacuum annealing may be used. A sample with 0.75% CuCl₂ and 2.5% GaF₃ on an 1100 nm ALE SrS layer, annealed overnight in vacuum at $\sim 350^\circ\text{C}$, produces a blue emitting phosphor. After annealing a 200 nm SiO_xN_y insulator is PECVD deposited and 100 - 150 nm Al dots are evaporated as top contacts. The resulting device has a broad emission peak at 472 nm and CIE coordinates of $x=0.16$,

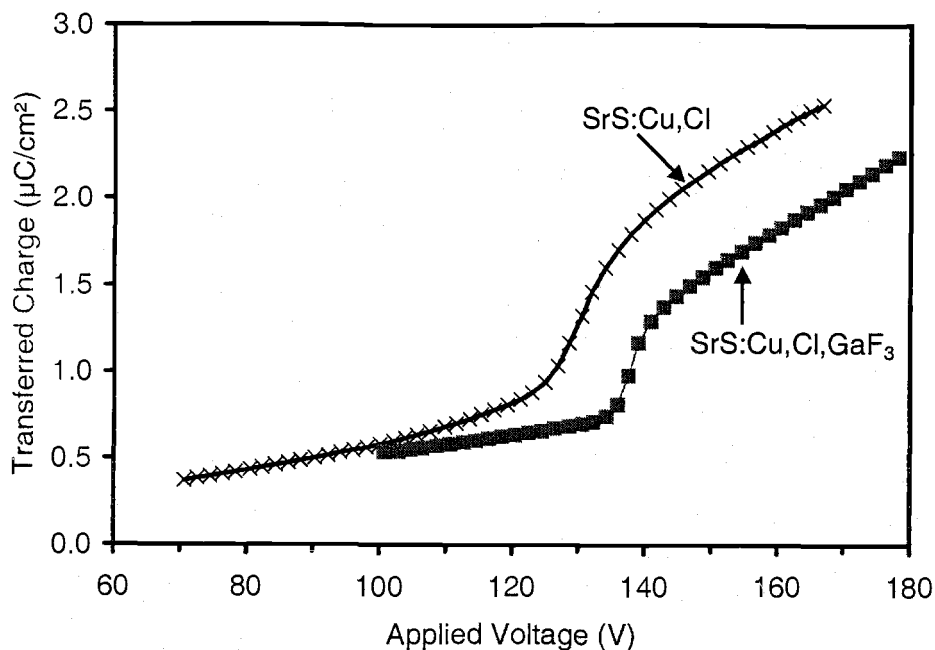


Figure 4.13: Q_{max} - V_{max} curves for ALE/SLDD SrS:CuCl₂ ACTFEL device with and without GaF₃.

$y=0.25$ at 40 V above threshold and 60 Hz. The L_{40} and η_{40} values under these driving conditions are 11.5 cd/m² and 0.1 lm/W. A similar device is prepared and annealed in N₂ at 450°C. The emission from this device gives $L_{40}=3.4$ cd/m², $x=0.16$, $y=0.23$ (60 Hz). The use of vacuum annealing on ALE/SLDD SrS:Cu,Cl,GaF₃ completes an entire ACTFEL device process flow where the substrate is never exposed to temperatures above 500°C. Optimization of the drive-in anneal temperature, anneal time, and source layer thickness should produce devices with luminance and efficiency suitable for commercial use.

4.1.2 CeCl₃ doping of ALE SrS

Fabrication of ALE SrS:Ce is also possible by the SLD method. CeCl₃ is diffused into ALE SrS during a 700°C RTA process. A layer of NaF is also added on top of the CeCl₃ layer as a coactivator/charge compensator. The emission from an ALE/SLDD SrS:Ce,Cl,NaF ACTFEL device consists of the two level recombination characteristic

of Ce^{3+} , as shown in Fig. 4.14. The peak wavelength is 484 nm with a shoulder in the green region near 550 nm, and the CIE x, y coordinates are 0.21, 0.43. L-V and η -V curves for this device, driven by a 60 Hz waveform, are shown in Fig. 4.15. At 60 Hz, the $V_{th}+30\text{V}$ luminance and luminous efficiency values are 36 cd/m^2 and 0.27 lm/W , respectively. It should be noted that the ALE/SLDD SrS:Ce,Na,Cl ACTFEL devices fabricated here suffer electrical instability around 30 V above V_{th} . It is believed that this instability is due to prolonged exposure to atmosphere of the ALE SrS layer before the SLD step, or a poor quality top insulator, and not an inherent fault of the phosphor material.

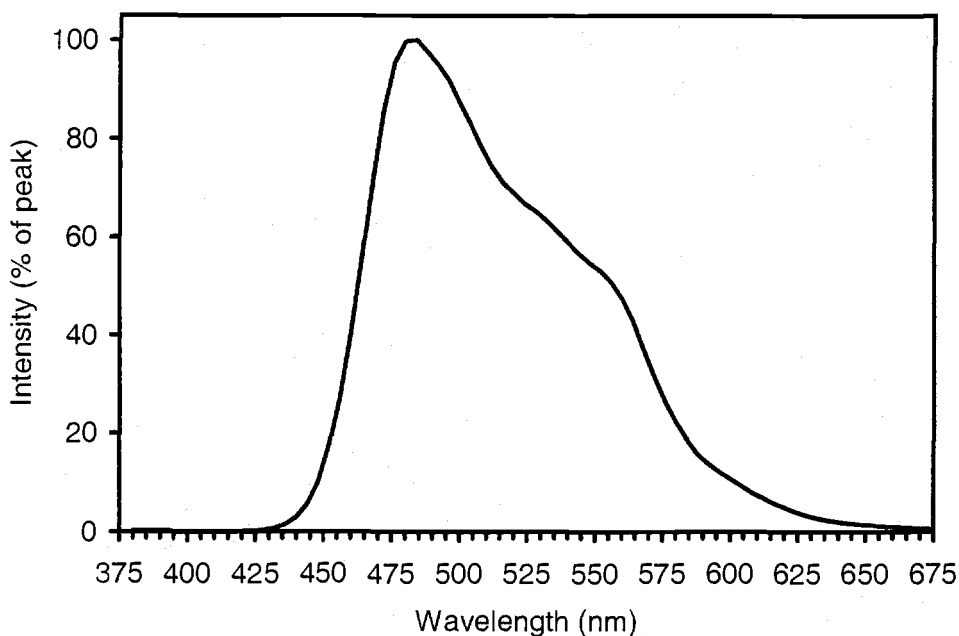


Figure 4.14: Electroluminescence emission spectrum for an ALE SrS film doped with CeCl_3 and NaF via source layer diffusion doping.

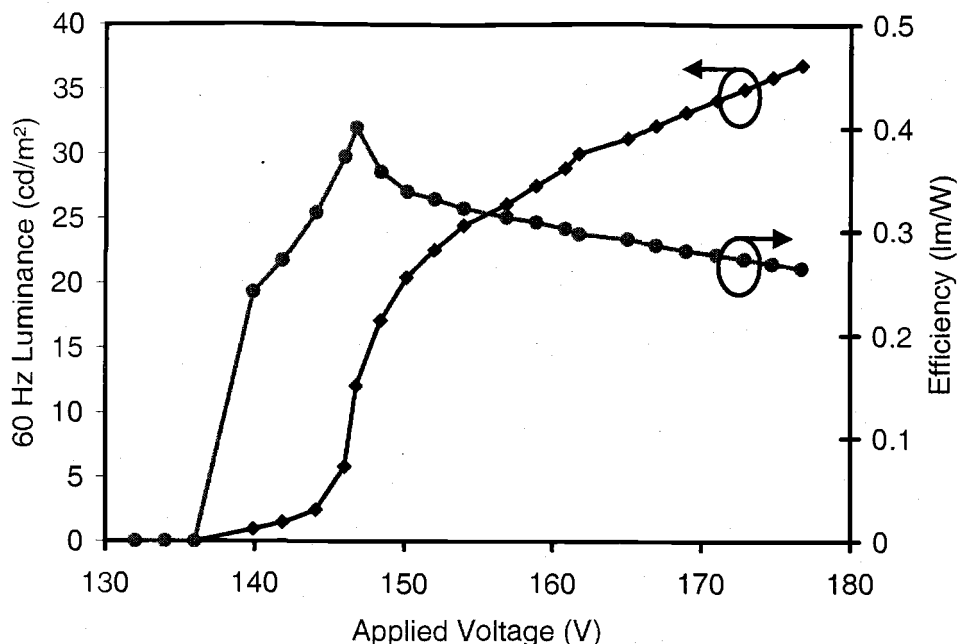


Figure 4.15: L-V and η -V curves for an ALE SrS film doped with CeCl₃ and NaF via source layer diffusion doping.

4.1.3 Eu doping of ALE SrS and CaS

The progress in SLDD of SrS films grown by ALE to produce bright blue and green phosphors has motivated the development of a red phosphor using the same processing technique. [110] A suitable red phosphor would make full-color active matrix electroluminescence (AMEL) possible using a patterned pixel approach. ALE SrS and CaS films are doped with Eu to evaluate their use as red alternating-current thin-film electroluminescent ACTFEL phosphors. [111] A red SrS phosphor is especially attractive as a means to realize a single-host, full-color system when used with blue and green SrS:Cu ACTFEL phosphors, particularly when considering that Cu acts as a sensitizer for Eu emission in SrS.

SrS and CaS films are grown by ALE and doped with Eu to produce phosphor layers in ACTFEL devices. Eu dopant incorporation is accomplished via diffusion from a dopant source layer using rapid thermal annealing. The ALE/SLDD dop-

ing approach promises improved manufacturability since it is accomplished at lower processing temperatures than when phosphor layers are deposited by sputtering or evaporation.

The ACTFEL devices under study are fabricated as follows. An un-doped SrS or CaS film is deposited onto a glass substrate coated with layers of indium tin oxide and aluminum-titanium oxide, which serve as the bottom transparent contact and the bottom insulator, respectively, of the ACTFEL device. The MS (M=Ca, Sr) layer is ALE deposited using H_2S and $\text{M}(\text{thd})_2$ precursors, where thd stands for 2,2,6,6-tetramethyl-3,5-heptanedionate. Next, thin layers of the appropriate dopant species, in this case EuCl_3 , are thermally evaporated onto the MS film. Rapid thermal annealing in an Ar atmosphere is then performed in order to diffuse the dopants into the MS film. The anneal temperatures used are 700°C for SrS and 810°C for CaS. A top insulating layer of silicon oxynitride is deposited by plasma-enhanced chemical vapor deposition, and aluminum dots are thermally evaporated as the top contact.

The emission spectra of Eu^{2+} in ALE CaS and SrS thin films are shown in Fig. 4.16. The incorporation of divalent Eu into the host lattice is evident from the broad band emission. The absence of any line emission characteristic of trivalent Eu indicates that most of the Eu ions are reduced upon incorporation from the EuCl_3 source into the host sulfide film. Emission from Eu in CaS is red shifted relative to SrS due to the crystal field effect.

SrS:Eu ACTFEL devices yield a near-saturated red color with a peak emission wavelength of 608 nm and CIE color coordinates of $x=0.619$, $y=0.379$. The peak position and color coordinates vary with Eu concentration. At 40 V above threshold a luminance of over 20 cd/m^2 and an efficiency of 0.14 lm/W is obtained, as shown in Fig. 4.17. ALE CaS:Eu ACTFEL devices emit a saturated red color at a wavelength of 648 nm. The CIE color coordinates are $x=0.686$ and $y=0.312$ with a luminance of 2 cd/m^2 driven at a frequency of 60 Hz and a voltage 40 volts above threshold.

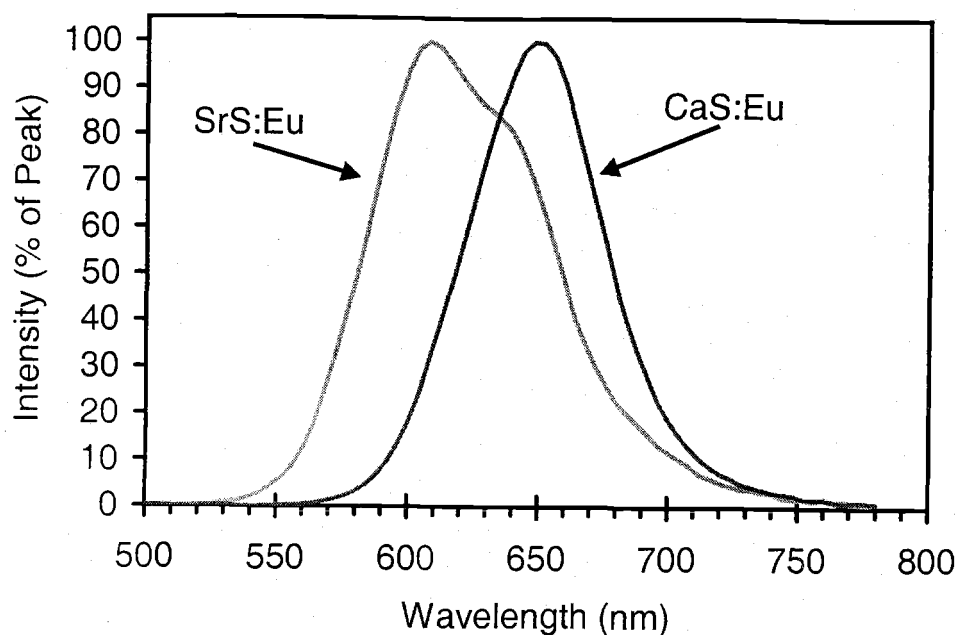


Figure 4.16: Electroluminescence emission spectra of ALE SrS:Eu and CaS:Eu ACT-FEL devices.

Electrical and electro-optical measurements are performed on SrS:Eu and CaS:Eu ACTFEL devices. Figure 4.18 shows Q - F_p curves for each type of device at an applied voltage 40 V above the threshold voltage. The curves show that the SrS device has more transferred charge and a lower phosphor field than the CaS device. The steady-state phosphor field in SrS:Eu is approximately 1.1 MV/cm versus 1.4 MV/cm in CaS:Eu. The smaller field is likely due to the fact that SrS has a smaller band gap than CaS (4.4 versus 4.8 eV), and therefore electron injection into the phosphor occurs at a lower field. It is possible that the phosphor field difference also depends on differences in the electron effective mass and on the dopant concentration levels in the different devices. [104] The SrS:Eu Q - F_p curve also shows an increase in transferred charge at low fields during the negative pulse polarity of the waveform (when the phosphor field is positive), just as seen in SrS:Cu,Ag,Cl devices. This is likely due to the EuCl_3 source layer disrupting the phosphor/top insulator interface. Further work is necessary to understand this phenomenon.

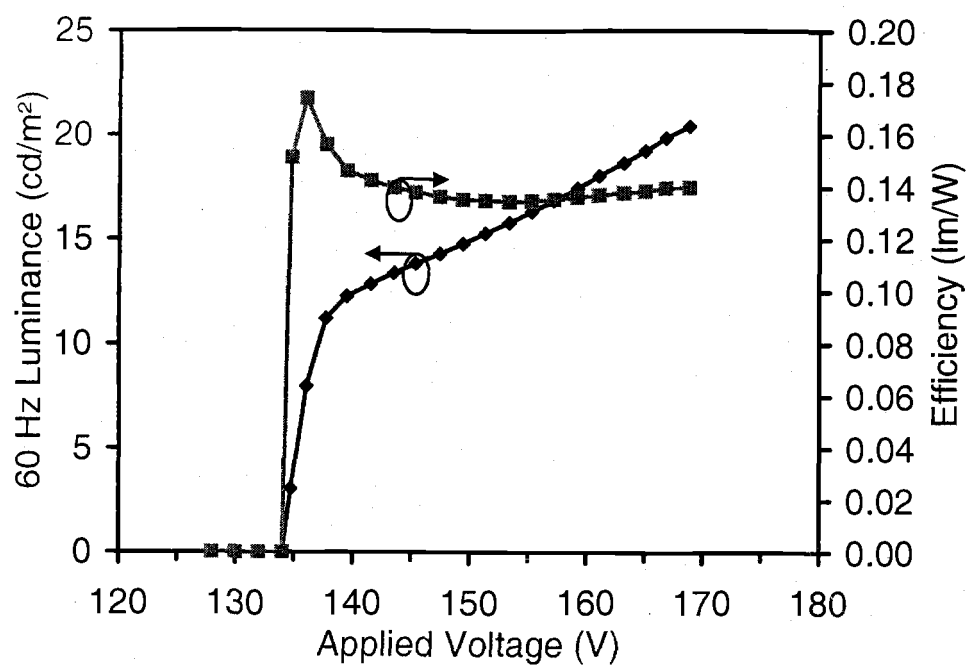


Figure 4.17: L-V and η -V curves obtained at a frequency of 60 Hz for an ALE SrS:Eu ACTFEL device.

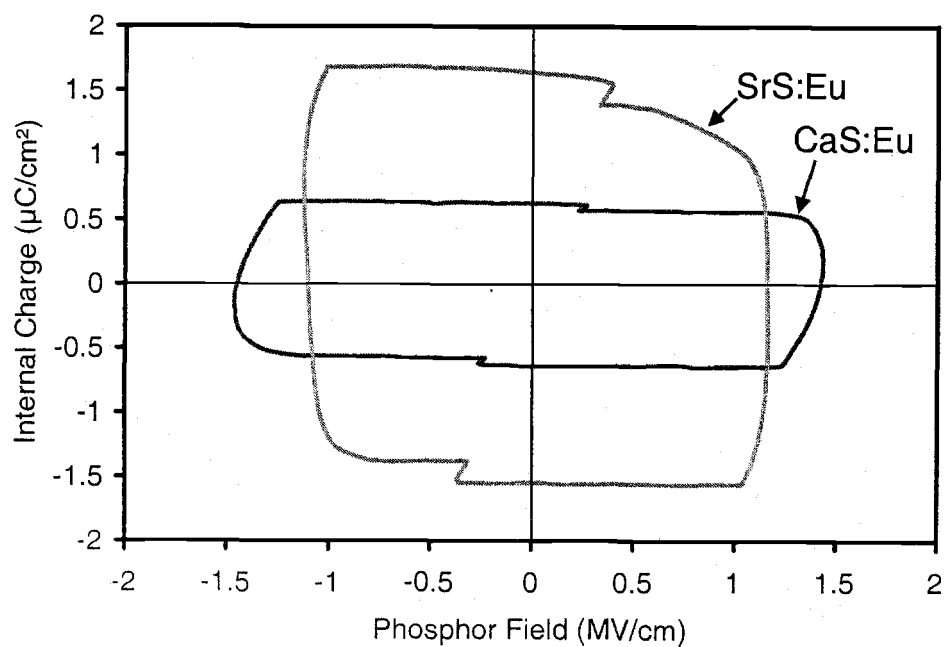


Figure 4.18: Q - F_p curves for ALE SrS:Eu and CaS:Eu ACTFEL devices taken at 40 V above the threshold voltage.

Transient brightness curves also show further similarities and differences between the SrS:Eu and CaS:Eu devices. The curves taken at 40 V above threshold are shown for both the positive and negative polarity pulse (applied to the Al contact) in Fig. 4.19 and Fig. 4.20. Each device emits light during both the rising and trailing edges of the applied voltage pulse. The light emission is essentially symmetric with respect to pulse polarity for the SrS:Eu device, but is not for the CaS:Eu device. The lack of symmetry in the CaS:Eu transient brightness curves suggests that the Eu distribution in the CaS host is not uniform. Eu^{2+} diffusion may occur more readily in SrS than in CaS, where the host cation is much smaller than the dopant ion. Ionic radii are known to be 131, 114, and 132 pm for Eu^{2+} , Ca^{2+} , and Sr^{2+} , respectively, in a 6-fold coordinated lattice environment.[112]

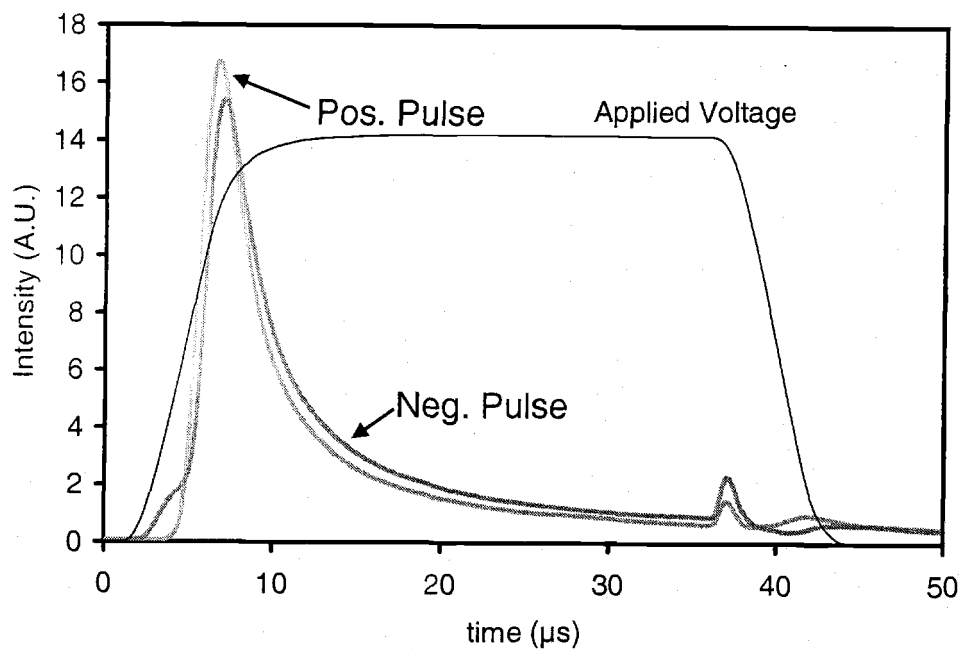


Figure 4.19: Transient brightness curves for ALE SrS:Eu ACTFEL devices taken at 40 V above the threshold voltage. Curves for both positive and negative pulse polarities are shown.

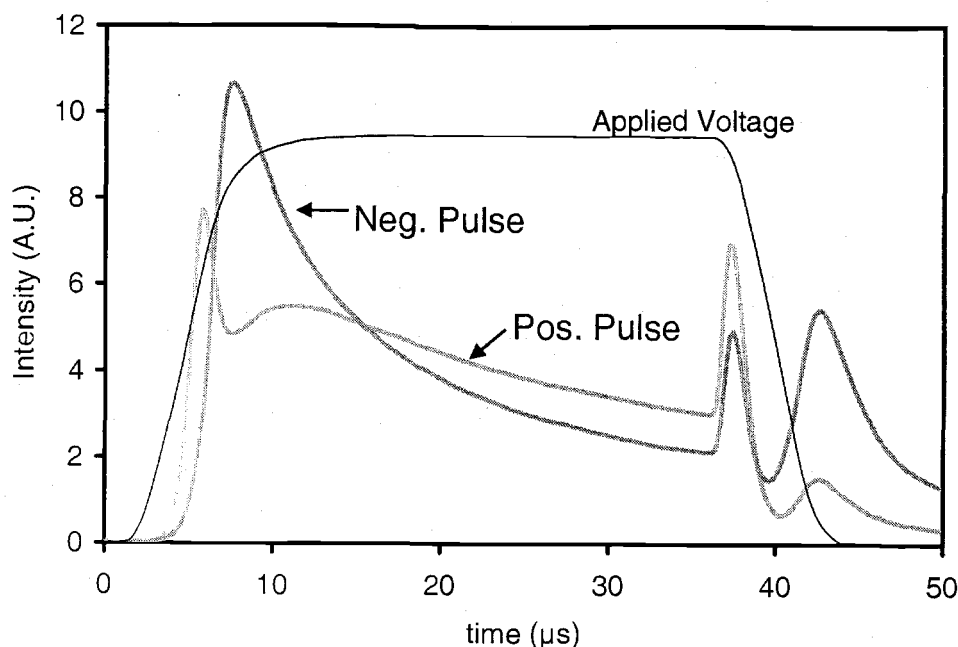


Figure 4.20: Transient brightness curves for ALE CaS:Eu ACTFEL devices taken at 40 V above the threshold voltage. Curves for both positive and negative pulse polarities are shown.

4.2 $\text{Sr}_x\text{Ca}_{1-x}\text{S:Eu,Cu}$

The Eu doping of ALE SrS and CaS in Section 4.1.3 indicates that a more ideal red ACTFEL phosphor would arise from doping an alloy of SrS and CaS with Eu. SrS:Eu does not produce red emission of suitable chromaticity for true full-color displays, while CaS:Eu is deep red, but is not bright enough or efficient enough. The investigation of $\text{Sr}_x\text{Ca}_{1-x}\text{S:Eu}$ is carried out through the deposition of phosphors from $\text{Sr}_x\text{Ca}_{1-x}\text{S}$ pellets by electron-beam evaporation. Pellets are prepared by synthesizing the desired compound from a mixture of SrCO_3 and CaCO_3 , or by directly mixing SrS and CaS powders, cold pressing the powder into pellets and sintering at $\sim 1000^\circ\text{C}$ in N_2 . $\text{Sr}_x\text{Ca}_{1-x}\text{S:Eu}$ phosphors are evaporated onto glass/ITO/ATO substrates using the “phosphor sandwich” technique, where dopant is introduced to the undoped phosphor host through source layer diffusion from source layers on both sides of the phosphor host. This technique is accomplished by thermally evaporating

a thin-film of EuCl_3 , electron-beam deposition of the phosphor host $\text{Sr}_x\text{Ca}_{1-x}\text{S}$, and then depositing a cap layer of EuCl_3 to approximately the same thickness as the initial EuCl_3 layer in the hopes of achieving dopant uniformity. The substrate temperature for all depositions in this study is 250°C , as measured by the thermocouple contacting the substrate holder. When Cu is desired as a co-activator, a CuCl_2 source layer is deposited above the EuCl_3 cap layer. It is also helpful to thermally co-evaporate KCl with the host pellet, or flux the pellet with KCl during the synthesis process. The KCl flux is found to enhance the stability of the phosphor thin-film in the final ACTFEL device. The dopants diffuse into the host during the rapid thermal annealing step at 810°C in an Ar atmosphere performed after evaporation is completed. After annealing, a 200 nm SiO_xN_y insulating layer is grown by PECVD and 100 - 150 nm Al contacts are evaporated on top of the phosphor layer to complete the ACTFEL device fabrication.

As shown in Fig. 4.21 and Table 4.6, decreasing the Sr:Ca ratio causes a red shift in the emission spectrum of $\text{Sr}_x\text{Ca}_{1-x}\text{S}:\text{Eu}$. As the value of x decreases, the crystal field experienced by the Eu^{2+} luminescent center increases, which causes the splitting of the Eu^{2+} excited state to increase, and lowers the energy of the emission transition. The change in crystal field causes the CIE x coordinate to increase and the y coordinate to decrease as the Sr:Ca ratio decreases and the emission moves to values of lower energy. A value of $x=0.4$ gives red chromaticity coordinates that reach the goal of $\text{CIE}_x=0.65$, $\text{CIE}_y=0.35$ for a red ACTFEL phosphor. Increasing the value of x further decreases the amount of Ca in the pellet to the point that the amount in the film is too small to induce a significant shift in the emission spectrum.

Photoluminescence excitation spectra of $\text{Sr}_x\text{Ca}_{1-x}\text{S}:\text{Eu}$ reveal that the excitation energy of Eu^{2+} overlaps the emission energy of $\text{Sr}_x\text{Ca}_{1-x}\text{S}:\text{Cu}^+$. Therefore, Cu^+ impurities in $\text{Sr}_x\text{Ca}_{1-x}\text{S}:\text{Eu}$ phosphors could act as sensitizers to red emitting Eu^{2+} luminescent centers. If a Cu^+ ion becomes impact excited by an energetic electron and decays, the emitted photon will be of the correct energy to excite a Eu^{2+} center,

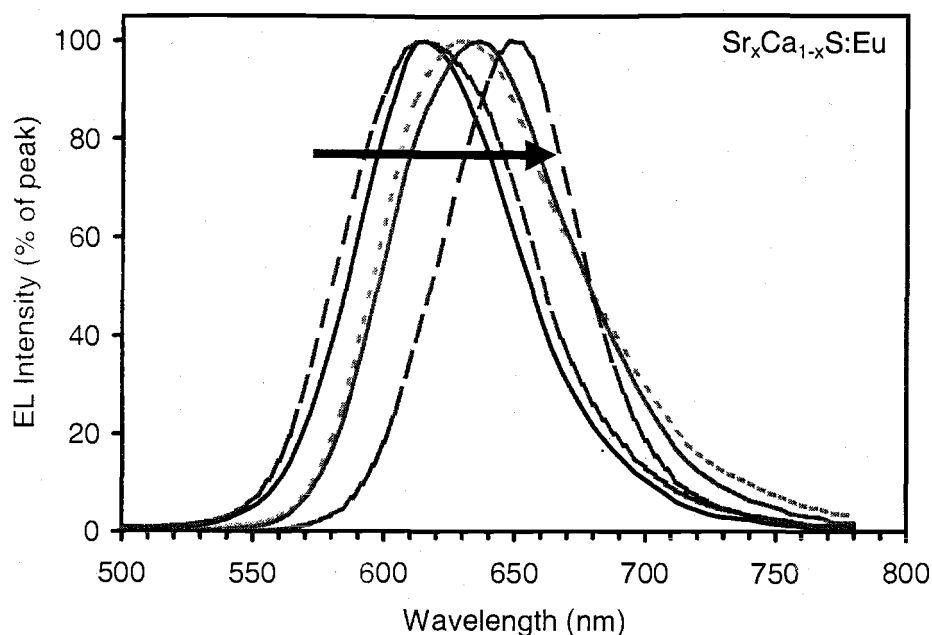


Figure 4.21: EL emission spectra of $\text{Sr}_x\text{Ca}_{1-x}\text{S:Eu}$ ACTFEL devices for $x=0, 0.2, 0.4, 0.7$ and 1 (the arrow indicates decreasing x).

so long as an ground state Eu^{2+} is available. In this way, the energy in hot electrons that is too high to excite Eu^{2+} , but not too high to excite Cu^+ , can be converted to red photons. The energy would otherwise be lost to the lattice, so the luminous efficiency should increase with the incorporation of Cu^+ . L-V and η -V curves for $\text{Sr}_{0.5}\text{Ca}_{0.5}\text{S:Eu}$ ACTFEL devices with and without Cu are shown in Figs. 4.22 and 4.23, respectively. The curves in Figs. 4.22 and 4.23 are taken with a 60 Hz bipolar trapezoidal waveform on a $\text{Sr}_{0.5}\text{Ca}_{0.5}\text{S:Eu}$ device with Cu doped onto one-half of the phosphor layer by SLDD, with a shadow mask covering half the sample during CuCl_2 deposition. By doping half of the sample with Cu, direct comparisons may be made without questioning the consistency of other process parameters. The most noticeable effect of Cu co-activation is the increase in brightness by $\sim 60\%$ and efficiency by $\sim 150\%$. The only effect of Cu co-doping on the color is a slight broadening of the

Table 4.6: EL emission from $\text{Sr}_x\text{Ca}_{1-x}\text{S}:\text{Eu}$ ACTFEL devices as a function of x .

x	λ_{peak} (nm)	CIE _x	CIE _y
0	648	0.686	0.312
0.2	636	0.655	0.339
0.4	628	0.653	0.344
0.5	624	0.639	0.354
0.7	616	0.615	0.365
1	616	0.615	0.380

emission peak, resulting in a decrease in the CIE x coordinate by 0.008 and an increase in the y coordinate by 0.002. The increase in luminous efficiency by 2.5 times the increase in luminance indicates that the increase in brightness is due to more than a simple increase in the amount of charge transferred through the device. The addition of CuCl_2 also causes a 10 V decrease in V_{th} and a softening of the threshold step in the L-V curve. The change in these characteristics leads to the conclusion that CuCl_2 incorporation into $\text{Sr}_x\text{Ca}_{1-x}\text{S}:\text{Eu},\text{Cl}$ significantly alters the charge trap state density in the ACTFEL device. One possible cause of change in the trap density is at the interface where the CuCl_2 was deposited. Another cause of charge state modification is through the incorporation of CuCl_2 into the phosphor bulk, which could cause states to be created or annihilated within the $\text{Sr}_x\text{Ca}_{1-x}\text{S}$ grains or at grain boundaries. The fact that the threshold voltage decreases concomitant with the overshoot decrease adds weight to the idea that the interface states are modified by the addition of CuCl_2 .

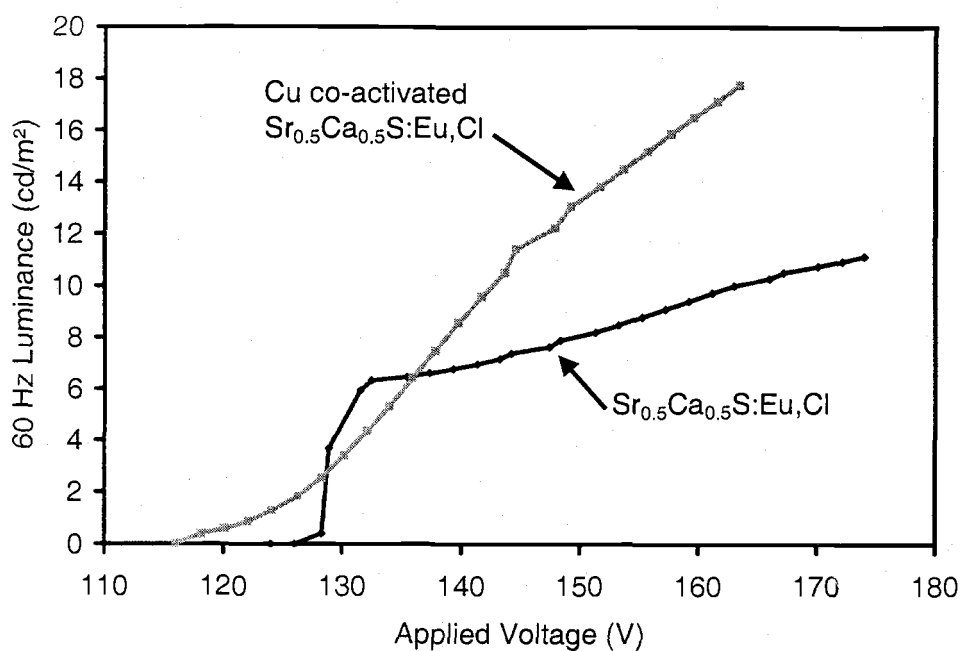


Figure 4.22: L-V curves of $\text{Sr}_{0.5}\text{Ca}_{0.5}\text{S:Eu,Cl}$ ACTFEL devices with and without Cu co-activation.

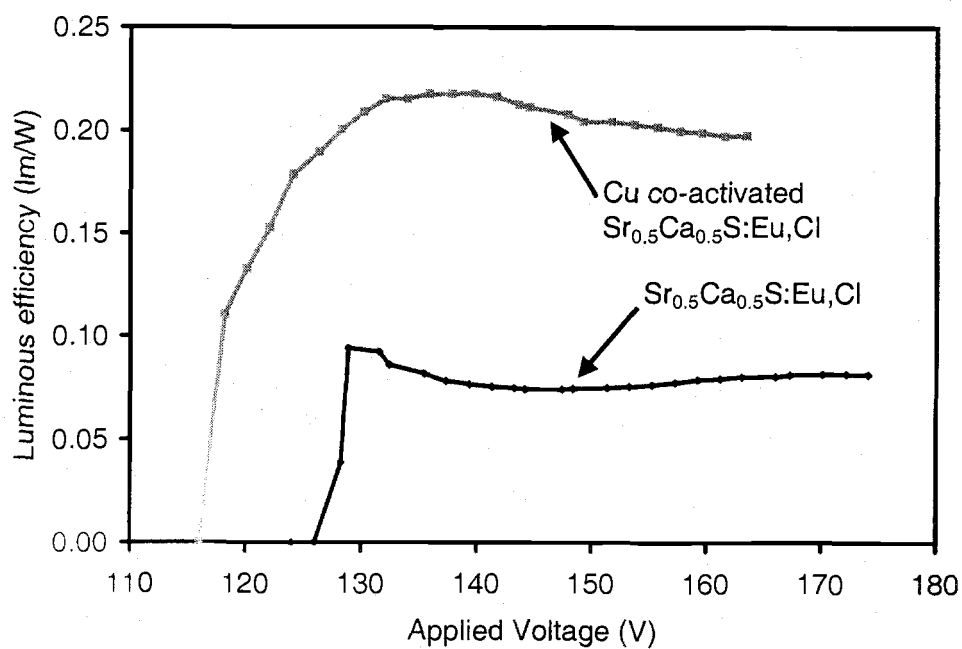


Figure 4.23: η -V curves of $\text{Sr}_{0.5}\text{Ca}_{0.5}\text{S:Eu,Cl}$ ACTFEL devices with and without Cu co-activation.

4.3 (Ba,Zn)S:Mn

The best known ACTFEL phosphor is ZnS:Mn; however, one of its drawbacks is the emission color. ZnS:Mn emits an amber color, which requires filtering for use as a red and green phosphor in full-color applications. The use of color filters is undesirable because it decreases the amount of light out-coupled to the viewer. The ability to tune the emission color of a phosphor to a suitable wavelength is advantageous because it removes the requirement for filters if the proper color can be obtained. With this in mind, a novel red emitting ACTFEL phosphor is investigated using Mn luminescent centers in a (Ba,Zn)S phosphor host.

The (Ba,Zn)S:Mn phosphor layers studied here are deposited by electron-beam evaporation of undoped (Ba,Zn)S pellets with thermal co-evaporation of Mn. (Ba,Zn)S pellets are prepared by mixing the desired ratio of BaS and ZnS powders, pressing the mixture into a pellet and sintering at $\sim 1000^\circ\text{C}$ in N_2 . It is likely that the stoichiometry obtained in the deposited film is significantly altered from that of the pellet, due to differences in the sticking coefficients and vapor pressures of Ba and Zn. The films are deposited on glass/ITO/ATO substrates, held at a temperature, T_S of 150°C . A deposition is also performed using a substrate temperature of 75°C to demonstrate the substrate temperature dependence. The devices are completed by depositing a 200 nm SiO_xN_y insulator by PECVD and thermally evaporating 100 - 150 nm thick Al contacts.

The EL emission wavelength and 1931 CIE color coordinates for the samples deposited, along with the value of T_S , are given in Table 4.7. The ratios given in the first column are the ratios of the weights of the powders as weighed out prior to pellet formation and sintering. The results shown in Table 4.7 do not exhibit a definite dependence on the BaS:ZnS ratio. Note however that there is a significant red shift from the emission of Mn in ZnS and BaS when the (Ba,Zn)S host is used. Note that the emission shifts to a wavelength that is not intermediate of the emission wavelengths of ZnS and BaS. The large red shift in emission is most probably due

Table 4.7: EL emission from (Ba,Zn)S:Mn ACTFEL devices of varying Ba:Zn ratios.

BaS:ZnS ratio (wt%)	T_S (K)	λ_{peak} (nm)	CIE _x	CIE _y
3:2	150	616	0.645	0.346
2:1	150	612	0.628	0.371
3:1	150	640	0.658	0.337
4:1	150	628	0.652	0.345
4:1	75	636 & 550	0.548	0.439
ZnS	75	584	0.538	0.460
BaS	250	596	0.495	0.456

to the formation of a crystal structure different from either ZnS or BaS, such as Ba₂ZnS₃. Further work, such as x-ray crystallography of the films, is necessary to clarify the poly-crystalline structure of the films deposited from evaporating (Ba,Zn)S pellets. Figure 4.24 shows the shift in the emission spectrum from ZnS:Mn for the 4:1 BaS:ZnS pellet deposited on a 150°C substrate.

4.4 Conclusions

Presented in this chapter are results of investigations aimed to develop improved ACTFEL phosphors for full-color applications. A high-luminance, high-efficiency, full-color ACTFEL phosphor system, capable of being processed at temperatures below the glass substrate melting temperature, has been developed through source layer diffusion doping of ALE deposited SrS thin-films. This processing technique should prove useful for manufacturing a full-color ACTFEL product with a single phosphor host material that does not require color filtering. Work has also been accomplished to develop new ACTFEL phosphor materials. The viability of a Sr_xCa_{1-x}S phosphor

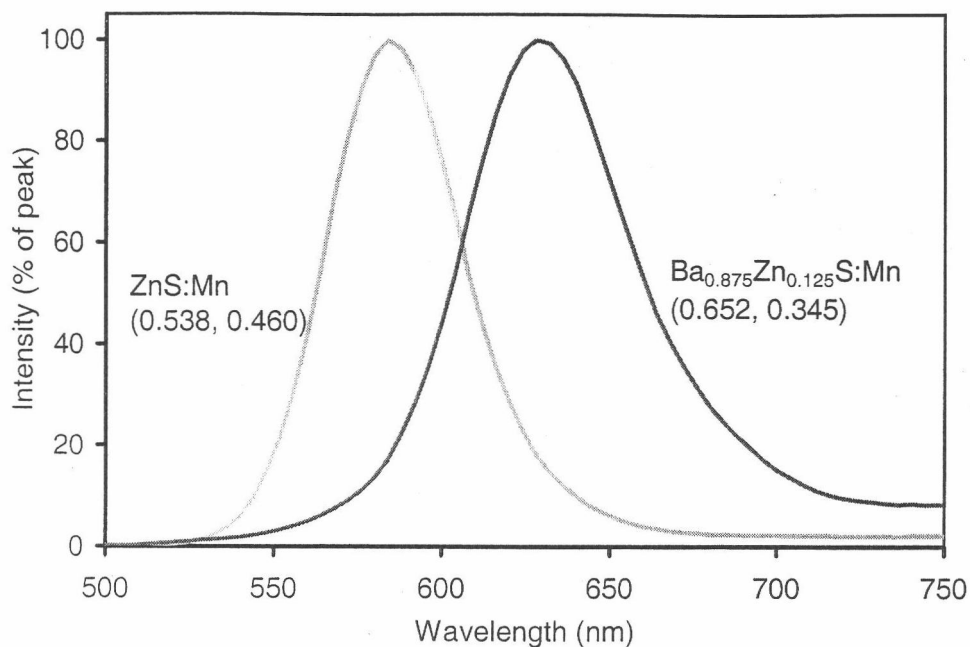


Figure 4.24: EL emission spectra of ZnS:Mn and Ba_{0.875}Zn_{0.125}S:Mn, with the CIE coordinates given in parentheses.

host doped with Eu has been investigated to achieve red emitting ACTFEL devices. Preliminary results from electron-beam evaporated Sr_xCa_{1-x}S:Eu,Cu ACTFEL devices show that a red phosphor with good luminance, efficiency, and chromaticity can be achieved by alloying SrS and CaS. It has also been demonstrated that red emitting ACTFEL devices may be fabricated from (Ba,Zn)S doped with Mn.

5. ACTFEL DEVICE CHARACTERIZATION

5.1 EL thermal quenching

The ability to operate over a wide temperature range (from $\sim -20^{\circ}\text{C}$ to $\sim 80^{\circ}\text{C}$) is an essential advantage of ACTFEL flat-panel displays. [6] Thus, the existence of electroluminescence (EL) thermal quenching in blue SrS:Cu and SrS:Cu,Ag ACTFEL devices is considered to be a serious impediment to the commercialization of such phosphors. [105, 106, 110, 113, 114] EL thermal quenching refers to a reduction in the luminance with increasing temperature, which is in excess to that of normal thermal quenching and is concomitant with a reduction in the transferred charge.

This section begins with an examination of EL thermal quenching trends for ZnS:Mn, SrS:Ce, and SrS:Cu ACTFEL devices. Then the SrS:Cu ACTFEL system is examined in greater detail to determine the exact nature of EL thermal quenching. Finally, it is shown that the insertion of one or more interface layers of SrS:Ce is an effective means to dramatically reduce the extent of EL thermal quenching in SrS:Cu. [114]

Optical and electrical measurements are performed at 25°C and 50°C on ACTFEL devices in order to observe EL thermal quenching properties, especially the increase in threshold voltage and decrease in luminance at increased temperature. The substrates are placed in a controlled Sun Systems environmental chamber in order to monitor and control the ambient temperature. L-V, η -V, Q_{max} - V_{max} , dQ_{max}/dV_{max} - V_{max} , Q-V, Q- F_p , and C-V measurements are taken to assess the effects of temperature on threshold voltage (V_{th}), luminance, luminous efficiency, transferred charge, and transferred charge capacitance. L-V and Q_{max} - V_{max} experiments are performed using a 60 Hz bipolar trapezoidal waveform with rise and fall times of $5\ \mu\text{s}$ and a $30\ \mu\text{s}$ pulse width. Q-V, Q- F_p , and C-V measurements are taken with the bipolar waveform at 40 V above the 25°C threshold voltage.

The confluence of factors that influence the operation of ACTFEL devices makes it difficult to determine the nature of ACTFEL device operation over the entire temperature range. In order to pragmatically identify the nature of EL thermal quenching as it pertains to ACTFEL applications, most experiments described in this section are performed only in the temperature range from 25°C to 50°C and are not necessarily applicable when extended far beyond this range.

5.1.1 ZnS:Mn

It has been found that evaporated ZnS:Mn ACTFEL devices perform, in many respects, in a nearly ideal manner. [11, 23] Thus, an examination of the EL thermal quenching tendencies of this type of device can help to establish an ideal performance base-line for EL thermal quenching. Figure 5.1 shows L-V and η -V curves for an evaporated ZnS:Mn ACTFEL device at 25°C and 50°C. The L-V curves show that there is only a slight change in V_{th} or the luminous intensity of the ZnS:Mn device over this temperature range. Although the η -V curves shown in Fig. 5.1 exhibit a slight decrease with increasing temperature, this decrease is very small. Similarly, the electrical characteristics of this device (not shown) exhibit almost no temperature dependence. Thus, the electrical and electro-optic properties of evaporated ZnS:Mn ACTFEL devices show very little temperature dependence between 25°C and 50°C.

The temperature dependence of the operation of an ALE ZnS:Mn ACTFEL device are also studied. Luminance-voltage and efficiency-voltage curves at room temperature ($\sim 25^\circ$) and 50°C are shown in Fig. 5.2. The L-V curves show that there is no decrease in electroluminescence as the temperature is increased over this range. This is surprising since some decrease is expected due to the thermal quenching of luminescence from Mn centers that is observed with UV excitation in photoluminescence. There is also no shift in the threshold voltage as the temperature is increased. A slight decrease in efficiency as temperature increases is observed in the η -V curves. Since the luminance is constant with respect to temperature, the decrease in efficiency

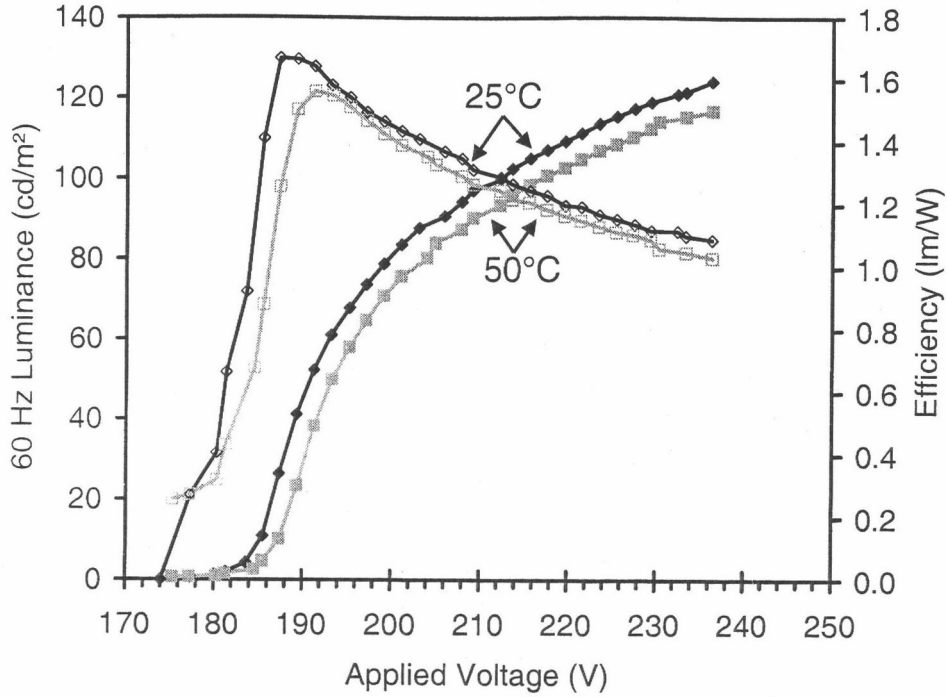


Figure 5.1: L-V and η -V curve comparison for an evaporated ZnS:Mn ACTFEL device at 25°C and 50°C.

must therefore be caused by an increase in power consumption in the device. This is consistent with Q_{max} - V_{max} measurements taken at both temperatures, as shown in Fig. 5.3. The small increase in transferred charge at 50°C appears to compensate for the normal thermal quenching that is expected due to an increase in non-radiative recombination with temperature, resulting in no change in the electroluminescence and a decrease in the luminous efficiency.

The Q_{max} - V_{max} curves shown in Fig. 5.3 show that there is very little change in the maximum transferred charge as the temperature is increased. Only a small increase in transferred charge above threshold is observed. There is no threshold voltage shift in either the Q_{max} - V_{max} or the L-V curves. The slope of the curve just above threshold, an indicator of the amount of space charge in the device, does not change with increasing temperature. As the voltage increases, the slope of the Q_{max} - V_{max} curve is slightly greater at 50°C than at 25°C. This results in more transferred

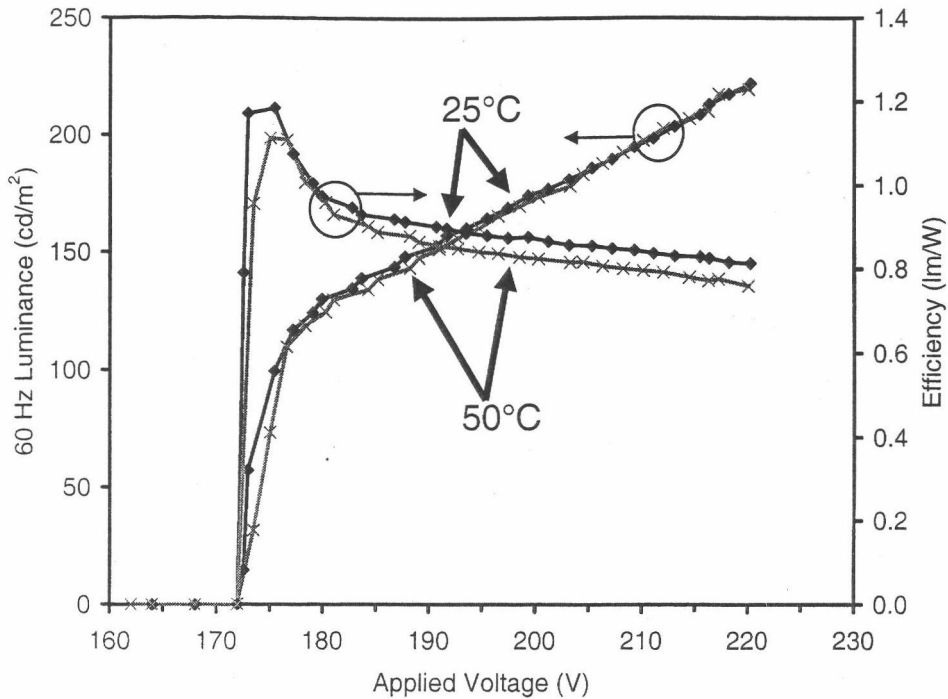


Figure 5.2: L-V and η -V curve comparison for an ALE ZnS:Mn ACTFEL device at 25°C and 50°C.

charge and a slight increase in power consumption. The increase in transferred charge with temperature is also observed in the Q - F_p curves shown in Fig. 5.4. There is a negligible change in the steady-state phosphor field with temperature. The polarization charge and relaxation charge both increase with temperature, which results in an increase in the conduction charge.

The lack of a substantial shift in V_{th} indicates that, in the neighborhood of room temperature, the electric field at the cathodic phosphor-insulator interface at a given voltage is not strongly temperature dependent in ZnS:Mn ACTFEL devices. Since the temperature dependence of the threshold voltage is weak in this temperature range, it is concluded that the phosphor field also remains nearly constant with respect to temperature. The threshold voltage is reached when a phosphor field is established that is large enough to cause electron injection into the phosphor from the cathodic phosphor-insulator interface states. The phosphor field is established by the applied

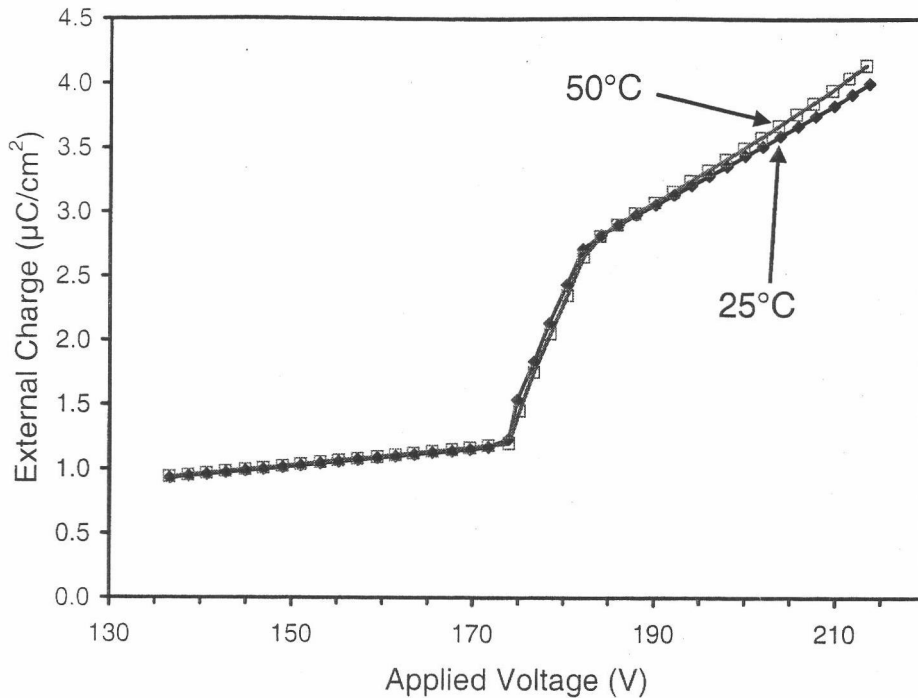


Figure 5.3: Q_{max} - V_{max} curves for an ALE ZnS:Mn ACTFEL device at 25°C and 50°C.

voltage and by bulk space charge in the phosphor. [16, 27] If the threshold voltage does not change with temperature, then the amount and distribution of bulk space charge must also be unchanged, and there is no change in the turn-on voltage and the phosphor field remains constant, as is observed in Fig. 5.4.

5.1.2 SrS:Ce

Another extensively studied ACTFEL phosphor is SrS:Ce, whose EL thermal quenching properties are also of interest in helping to establish an ideal performance base-line for EL thermal quenching. As shown in Fig. 5.5, ALE SrS:Ce ACTFEL devices exhibit some temperature-dependence in their L-V and η -V characteristics between 25°C and 50°C. In the L-V curves shown, the threshold voltage increases slightly with increasing temperature. However, the most dramatic L-V curve trend is the significant decrease in luminance with increasing temperature. This is attributed

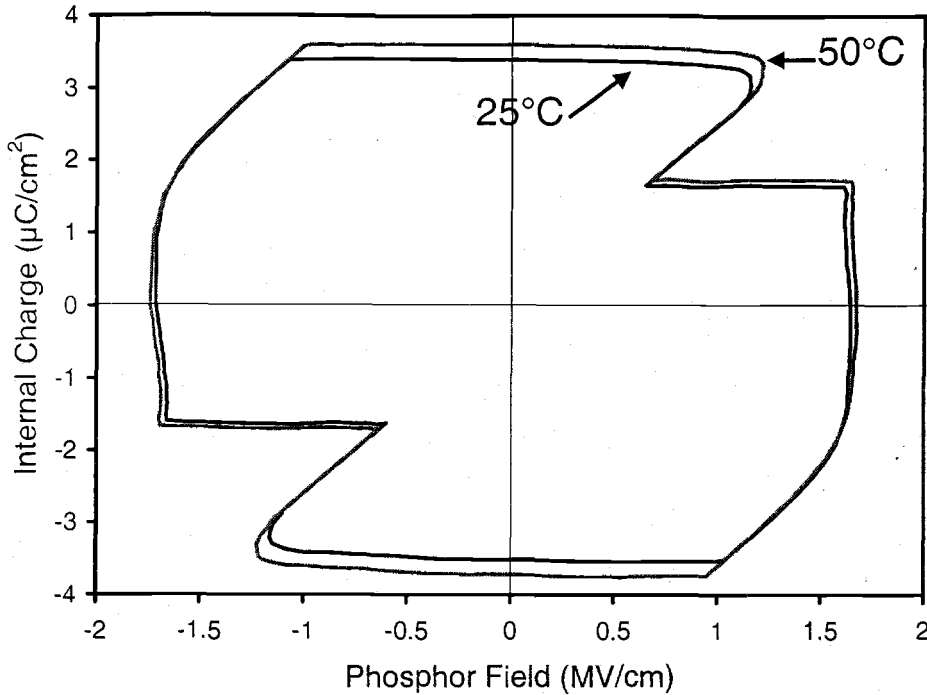


Figure 5.4: Q - F_p curves (at ~ 40 V above V_{th}) for an ALE ZnS:Mn ACTFEL device at 25°C and 50°C .

to normal thermal quenching in which higher temperatures result in an increase in the rate of non-radiative recombination of excited luminescent impurities. Note that this decrease in luminance with increasing temperature is ascribed to normal thermal quenching instead of EL thermal quenching since there is actually a slight increase in the transferred charge (not shown) above threshold at 50°C compared to 25°C . The decrease in luminance and increase in transferred charge combine to reduce the efficiency of SrS:Ce ACTFEL devices as temperature increases. There is also no decrease in overshoot in transferred charge capacitance curves (not shown) in SrS:Ce from 25°C to 50°C . This is evidence that the space charge density is not significantly reduced with increasing temperature in SrS:Ce ACTFEL devices.

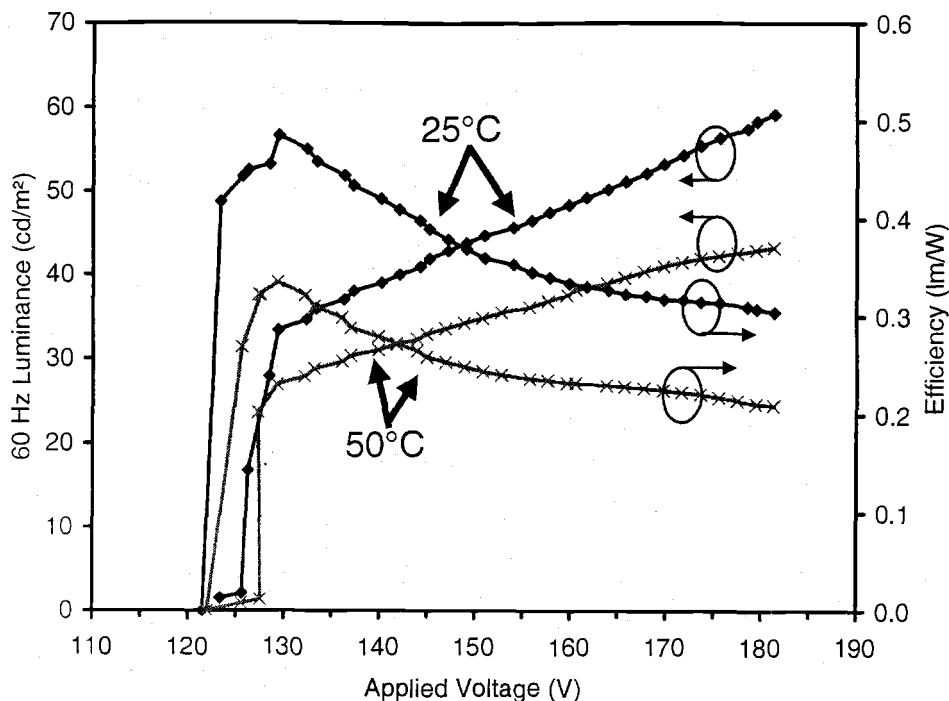


Figure 5.5: L-V and η -V curves for an ALE SrS:Ce ACTFEL device at 25°C and 50°C.

5.1.3 SrS:Cu

A significant decrease in the luminance of SrS:Cu ACTFEL devices is observed with increasing temperature. The severity of the decrease in luminance with temperature in SrS:Cu ACTFEL devices is evident in the L-V curves in Fig. 5.6. As the temperature increases, the threshold voltage increases and the luminance drops dramatically. The effect of temperature on SrS:Cu ACTFEL devices is considered to be a serious impediment to the commercialization of such phosphors. [89, 105, 106, 110, 113, 114] The reduction in the luminance with increasing temperature in excess to that of “normal” thermal quenching, which is concomitant with a reduction in the transferred charge, is referred to as EL thermal quenching. “Normal” thermal quenching refers to the increase in non-radiative relaxation of excited luminescent centers with an increase in temperature. EL thermal quenching as observed in SrS:Cu ACTFEL devices in the vicinity of room temperature is attributed

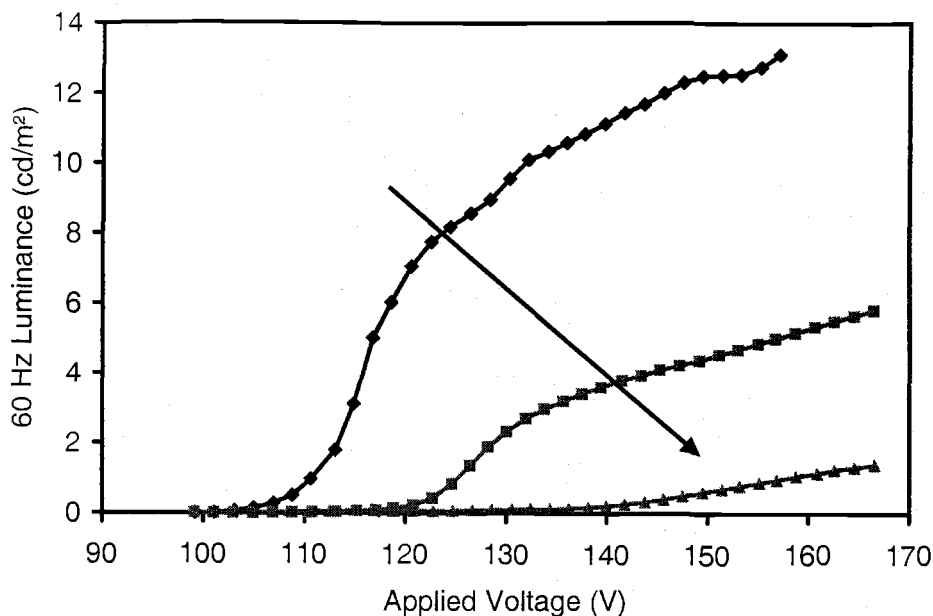


Figure 5.6: L-V curves for a sputtered SrS:Cu ACTFEL device at -40, 20, and 80°C (arrow indicates increasing temperature).

to a thermally activated annihilation of positive space charge and a corresponding increase in the threshold voltage.

Thermal quenching is traditionally thought of as an increase in the rate of non-radiative relaxation of excited luminescent centers with an increase in temperature. [80] This is due to a thermally activated increase in non-radiative excited state relaxation to the ground state via crossing over the intersection of the configurational coordinate curve. The configurational coordinate diagram shown in Fig. 5.7 presents the total energy of a luminescent center in its ground and excited states as a function of the configurational coordinate. Optical absorption and emission processes proceed as indicated by the arrows $A \rightarrow B$ and $C \rightarrow D$, respectively. If sufficient thermal energy is available, the electron in the excited state may be raised to the intersection of the two configurational coordinate curves, indicated by point E in Fig. 5.7. Once the intersection is reached, the electron may transfer to the ground state non-radiatively.

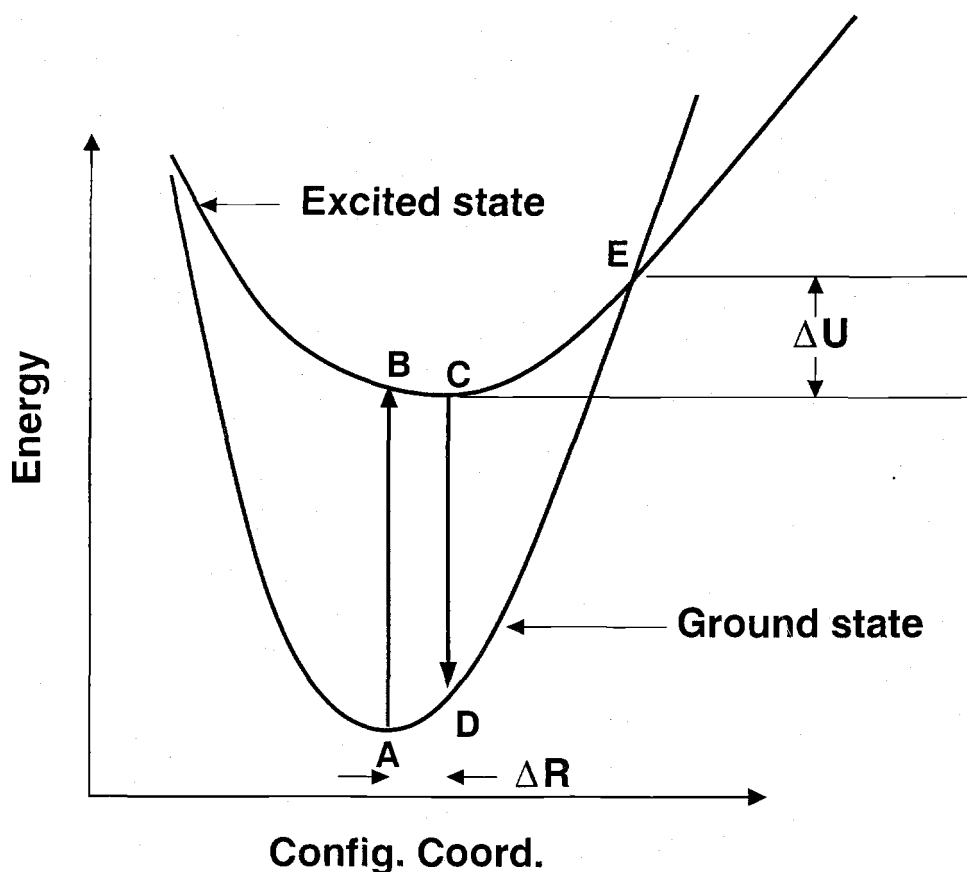


Figure 5.7: A configurational coordinate diagram of a luminescent center.

The process may be assumed to be an exponential process with an activation energy of ΔU . [86]

Both SrS:Cu and SrS:Cu,Ag single-layer ACTFEL devices exhibit a significant amount of EL thermal quenching. [89] For example, Fig. 5.8 shows the L-V and η -V curves at 25°C and 50°C for a sputtered SrS:Cu,Ag ACTFEL device. This figure demonstrates a threshold voltage increase of 14 V and a decrease in luminance of 40%, with increasing temperature; these results are typical for ACTFEL devices fabricated using SrS:Cu or SrS:Cu,Ag phosphors. These temperature trends are attributed to EL thermal quenching since it has been demonstrated that transferred charge and L-V trends correlate quite well. [110] In particular, the threshold voltages estimated from transferred charge and from L-V measurements are found to be very similar and

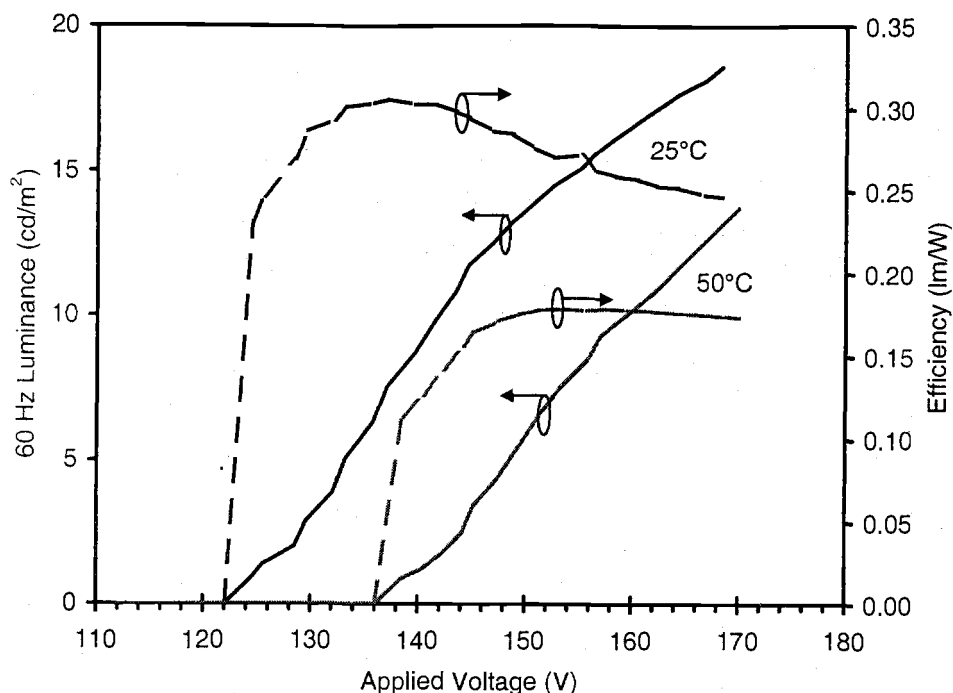


Figure 5.8: L-V and η -V curves for a sputtered SrS:Cu,Ag ACTFEL device at 25°C and 50°C.

to increase with increasing temperature, resulting in less transferred charge at a given voltage above V_{th} at higher temperature, as seen in Fig. 5.9. Note also from Fig. 5.9 that the above-threshold rise in the transferred charge is less steep for the 50°C curve compared to the 25°C curve and, equivalently, the transferred charge capacitance overshoot is less for the 50°C curve compared to the 25°C curve; both of these trends are consistent with having less positive space charge in the phosphor at the higher temperature.

EL thermal quenching as observed in SrS:Cu ACTFEL devices in the vicinity of room temperature is attributed to an increase in the threshold voltage caused by the thermally activated annihilation of positive space charge. [110] The decrease in the magnitude of transferred charge capacitance overshoot is interpreted as a decrease in the amount of positive phosphor space charge. Band bending due to positive space charge in the bulk increases the field at the cathodic interface at a given voltage.

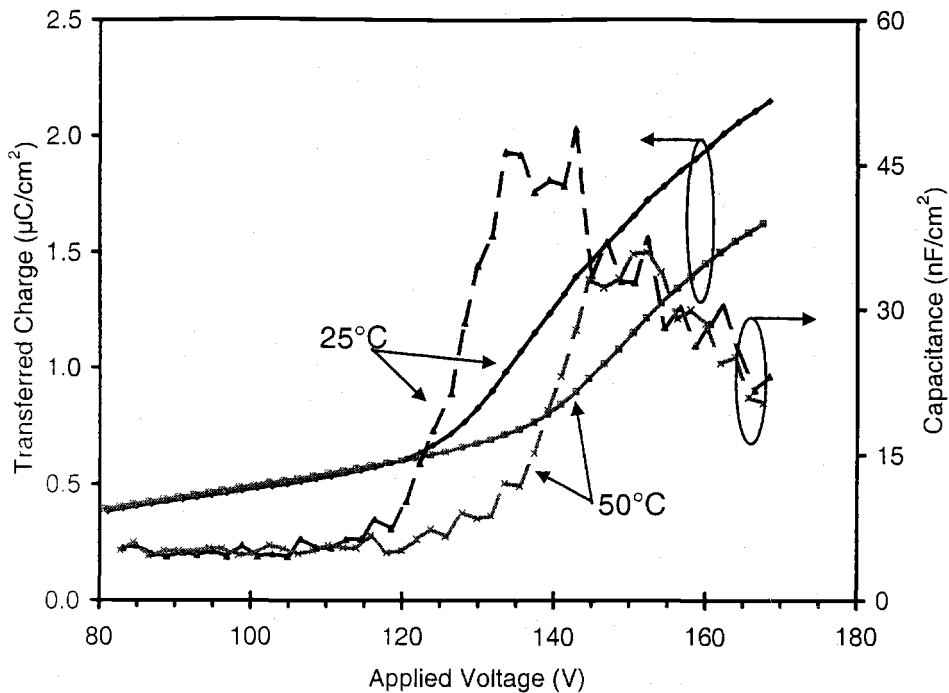


Figure 5.9: Q_{max} - V_{max} and transferred charge capacitance curves for a sputtered SrS:Cu,Ag ACTFEL device at 25°C and 50°C.

The decrease in space charge results in less enhancement of that field. Thus, when the temperature is increased, a larger voltage is necessary to establish the phosphor cathode field required for electron injection. The cathode field required for electron injection is reached at a smaller voltage at 25°C than at 50°C because more positive space charge is present in the phosphor at 25°C. The origin of phosphor space charge in SrS:Cu ACTFEL devices is attributed to the trapping of holes generated by band-to-band impact ionization, where an energetic electron excites a valence band electron to the conduction band, leaving a hole in the valence band. Emission of trapped holes increases with temperature, which results in a decrease of positive space charge with temperature. With less positive space charge in the phosphor, a larger voltage must be applied to achieve electron injection from the phosphor/insulator interface, resulting in an increase of the threshold voltage with temperature.

Further insight into the temperature dependence of the operation of SrS:Cu,Ag ACTFEL devices is gained from Q-V and Q-F_p curves. The Q-V curves, given in Fig. 5.10, are obtained at 40 V above the 25°C threshold voltage; in other words, these curves are obtained at the same maximum applied voltage at both temperatures. The Q-V curves show that with increasing temperature, there is a decrease in transferred charge, as well as an increase in the turn-on voltage (V_{to}). The turn-on voltage is the voltage across the ACTFEL device corresponding to the onset of emission of electrons from interface states or bulk traps. The increase in turn-on voltage indicates that more voltage is required to obtain a field at the cathodic interface that is large enough to inject electrons into the phosphor. An increase in turn-on voltage is caused by a decrease in polarization charge, a decrease in positive bulk space charge, or a combination of the two. Figure 5.11 shows the Q-F_p curves corresponding to the Q-V curves in Fig. 5.10. Note from Fig. 5.11 that the amount of conduction charge flowing across the phosphor decreases, the polarization charge decreases, and the average phosphor field increases with increasing temperature. An increase in the phosphor field corresponds to a decrease in positive bulk space charge. [55] An increase in positive space charge in the bulk of the phosphor at a given voltage increases the field at the cathodic interface and causes V_{th} to decrease, while a decrease in positive space charge lowers the cathodic field and increases V_{th} . While a decrease in positive space charge causes the *cathodic* field to decrease, the *average* phosphor field, which is the quantity plotted in a Q-F_p curve, increases.

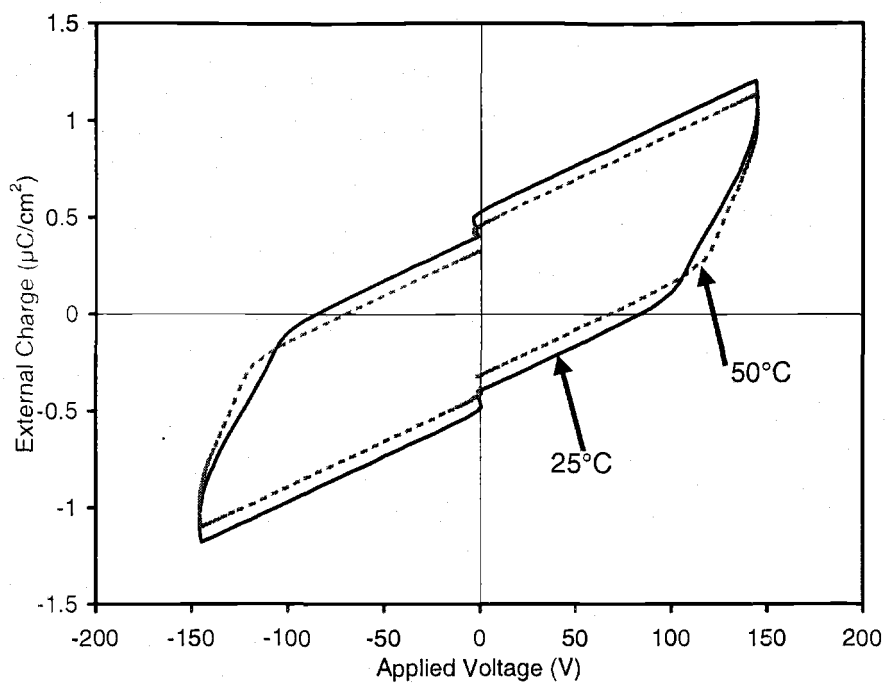


Figure 5.10: Q-V curves for a sputtered SrS:Cu,Ag ACTFEL device at 25°C and 50°C.

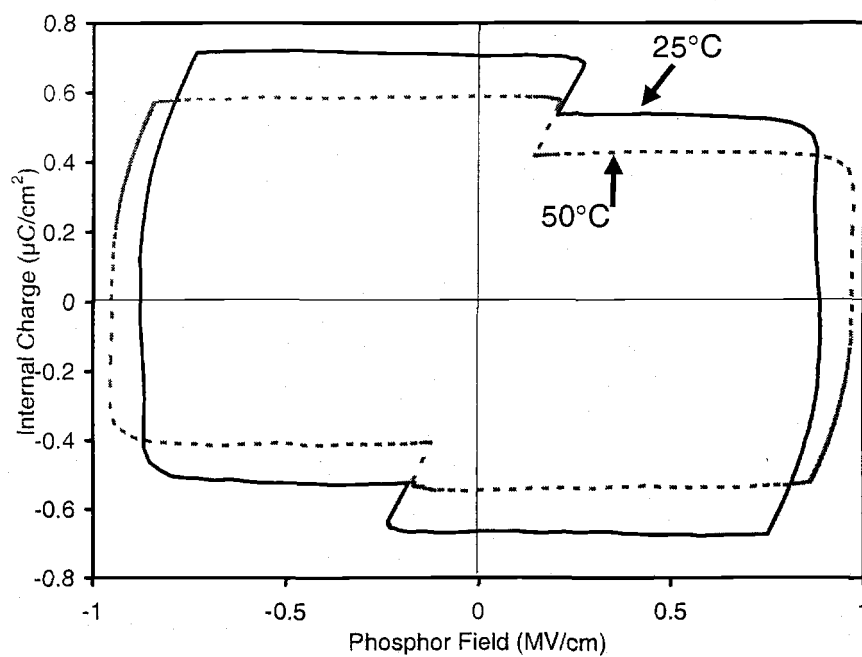


Figure 5.11: Q- F_p curves for a sputtered SrS:Cu,Ag ACTFEL device at 25°C and 50°C.

5.1.4 SrS:Cu,Ag with SrS:Ce interface layers

Figure 5.12 illustrates the L-V and η -V curves at 25°C and 50°C for a sputtered, multi-layer SrS:Cu,Ag ACTFEL device with SrS:Ce interface layers. The SrS:Ce layers consist of a 100 nm ALE deposited film on the bottom interface and a 200 nm sputtered film on the top interface. The SrS:Cu,Ag layer is 1000 nm thick and is deposited by RF sputtering. The significant improvement in EL thermal quenching properties of this device is clearly evident in the L-V and η -V curves shown in Fig. 5.12, when compared to those shown in Fig. 5.8 for a single-layer SrS:Cu,Ag ACTFEL device. In particular, the temperature-dependent change in the threshold voltage has been reduced from a 14 V shift to a shift of 4 V and the temperature-dependent luminance reduction at +40 V above threshold has been improved from a decrease of 40% to a decrease of 14%. Moreover, the introduction of SrS:Ce interface layers results in much less temperature-dependence in the transferred charge characteristics,

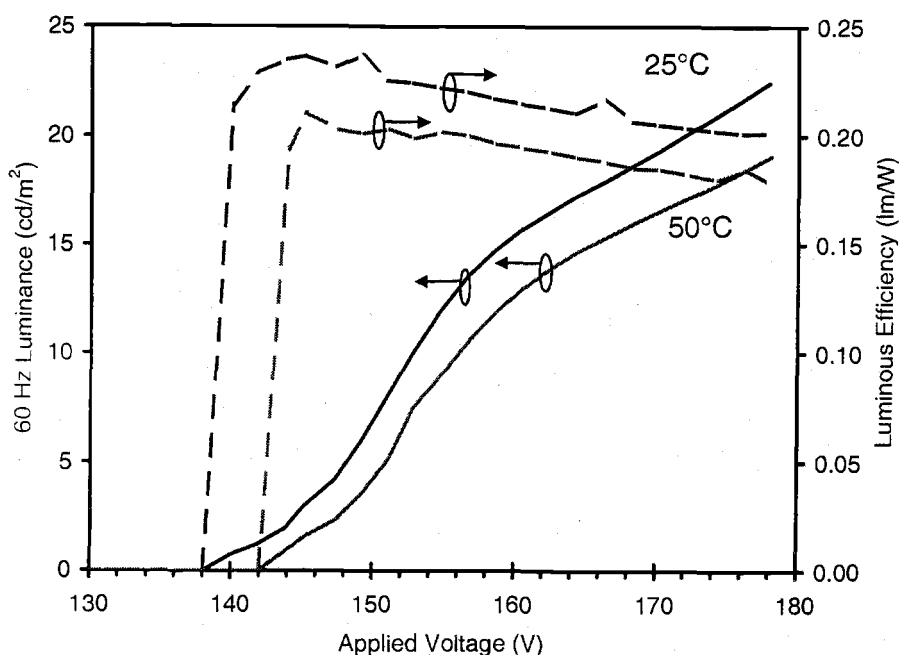


Figure 5.12: Luminance-voltage and efficiency-voltage curves for a sputtered SrS:Cu,Ag ACTFEL device containing SrS:Ce interface layers at 25°C and 50°C.

as shown in Fig. 5.13; in particular, there is much less change in the threshold voltage and transferred charge capacitance overshoot with temperature. The multi-layer SrS:Cu,Ag device maintains good luminance and luminous efficiency performance with values at +40 V above threshold of 22 cd/m² and 0.2 lm/W, respectively.

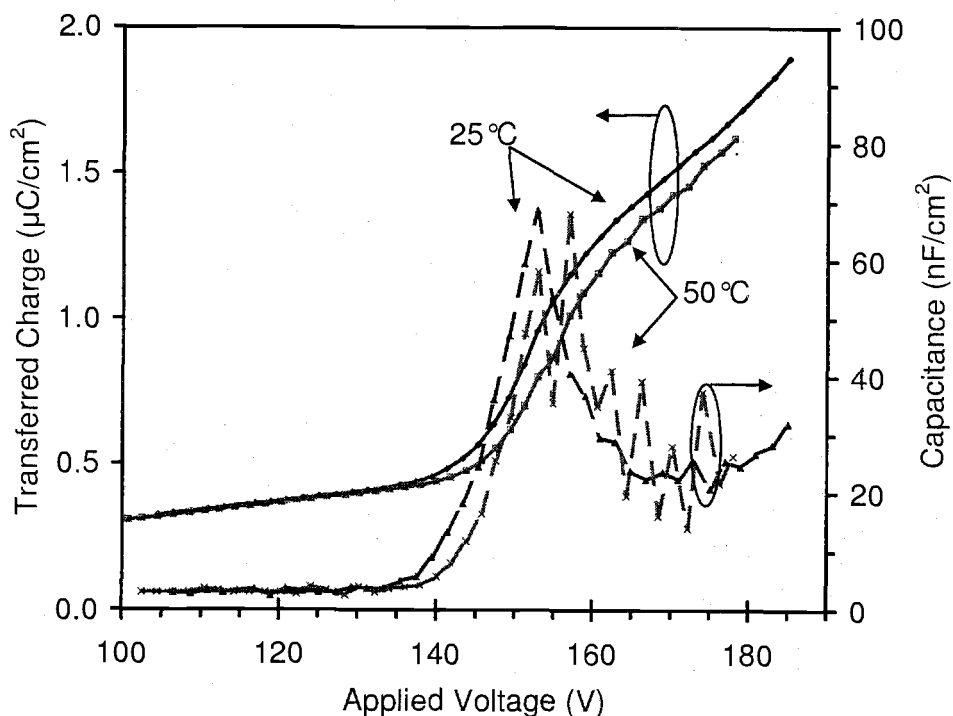


Figure 5.13: Q_{max} - V_{max} and transferred charge capacitance curves for a sputtered SrS:Cu,Ag ACTFEL device containing SrS:Ce interface layers at 25°C and 50°C.

Additional confirmation of the significant reduction of EL thermal quenching for multi-layer SrS:Cu,Ag ACTFEL devices with SrS:Ce interface layers is evident from an analysis of the Q - V and Q - F_p curves at 25°C and 50°C, as shown in Figs. 5.14 and 5.15; these curves should be compared to those shown in Figs. 5.10 and 5.11. Although these Q - V and Q - F_p curves change slightly with temperature, the differences are much less pronounced than those observed in Figs. 5.10 and 5.11 for the single layer SrS:Cu,Ag device. The decrease in transferred charge with temperature

observed in the Q_{max} - V_{max} curve is also evident in the Q - V curve in Fig. 5.14. The magnitude of V_{to} is equal at both temperatures for the positive pulse and increases only slightly during the negative pulse. The multi-layer SrS:Cu,Ag Q - F_p curves are much more similar at the two temperatures than those for the device without SrS:Ce layers. At the increased temperature, the steady-state phosphor field is unchanged from room temperature in the multi-layer device. Also, the field overshoot in this device is observed to increase during the negative pulse, which coincides with electron emission from the top interface, where the SrS:Ce layer thickness is 200 nm.

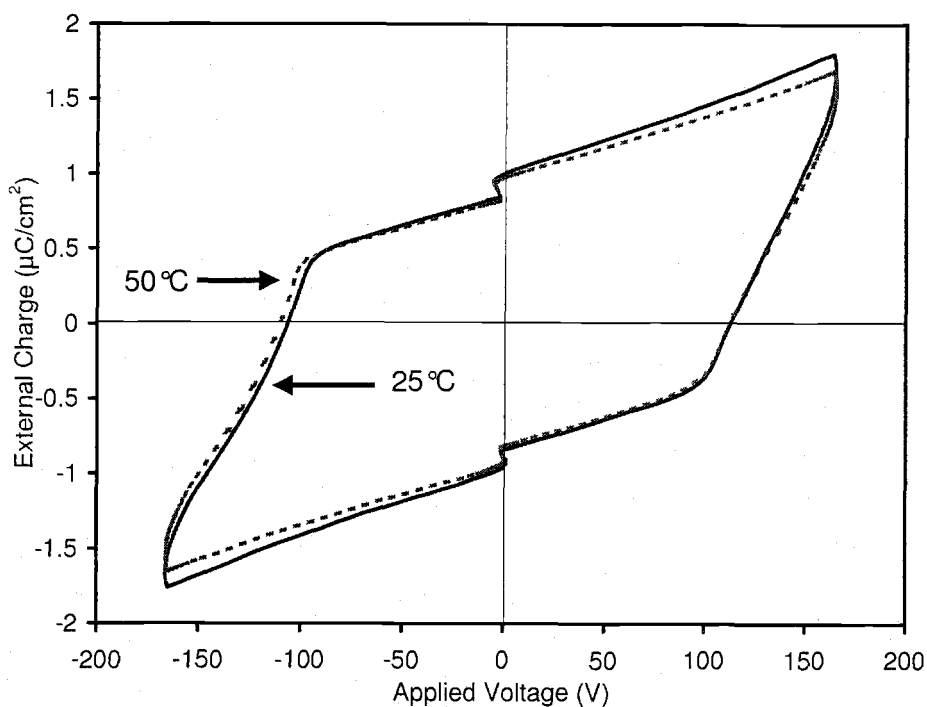


Figure 5.14: Q - V curves for a sputtered SrS:Cu,Ag ACTFEL device containing SrS:Ce interface layers at 25°C and 50°C.

The insertion of SrS:Ce interface layers into a SrS:Cu,Ag ACTFEL device also affects the emission spectrum from the device. The result is a green shift of the EL emission spectrum, as shown in Fig. 5.16. The addition of SrS:Ce interface layers

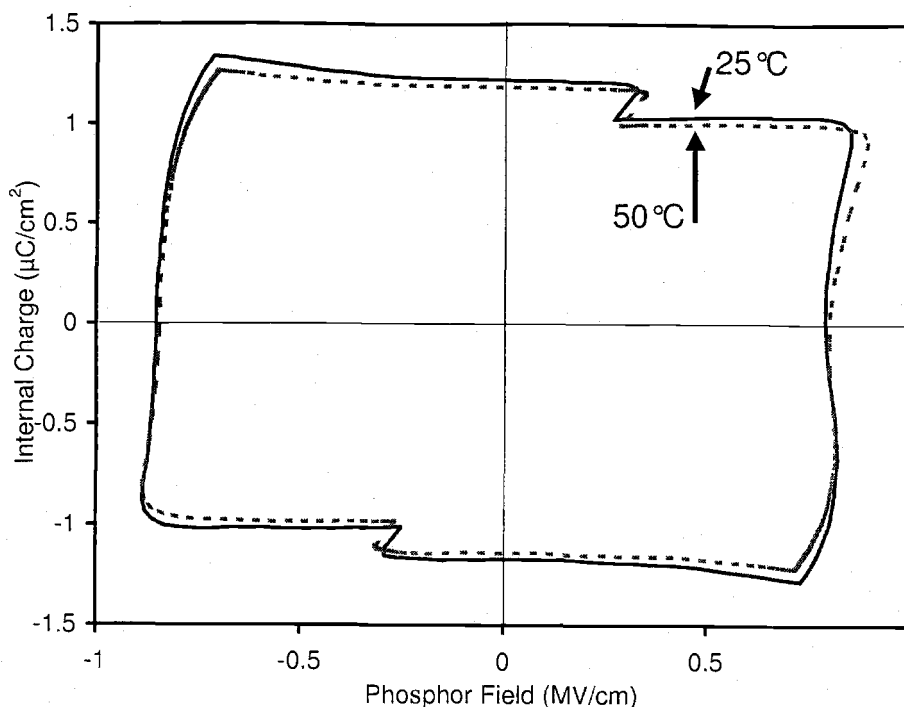


Figure 5.15: Q - F_p curves for a sputtered SrS:Cu,Ag ACTFEL device containing SrS:Ce interface layers at 25°C and 50°C.

causes Ce emission to occur, along with the emission from the SrS:Cu,Ag layer. The resulting spectrum is the superposition of the SrS:Ce and SrS:Cu,Ag emission. The CIE coordinates are shifted from $x=0.182$, $y=0.200$ to $x=0.186$, $y=0.264$ with the insertion of SrS:Ce interface layers.

A result of the superposition of emission from the constituent layers of a SrS:Cu,Ag ACTFEL device with SrS:Ce injection layers is a change in the EL emission spectrum with temperature. The peak position of the spectrum does not change drastically with temperature, but the relative magnitudes of the peaks in the spectrum vary with temperature, as seen in Fig. 5.17. The intensity of the 430 nm peak, attributed to SrS:Cu,Ag emission, decreases with temperature much more than the peaks at 480 nm and 530 nm, which are due to emission from Ce^{3+} . This decrease in the relative intensity of the 430 nm peak is a result of more traditional thermal quenching occurring in Cu^+ or Ag^+ luminescent centers than in Ce^{3+} centers. The

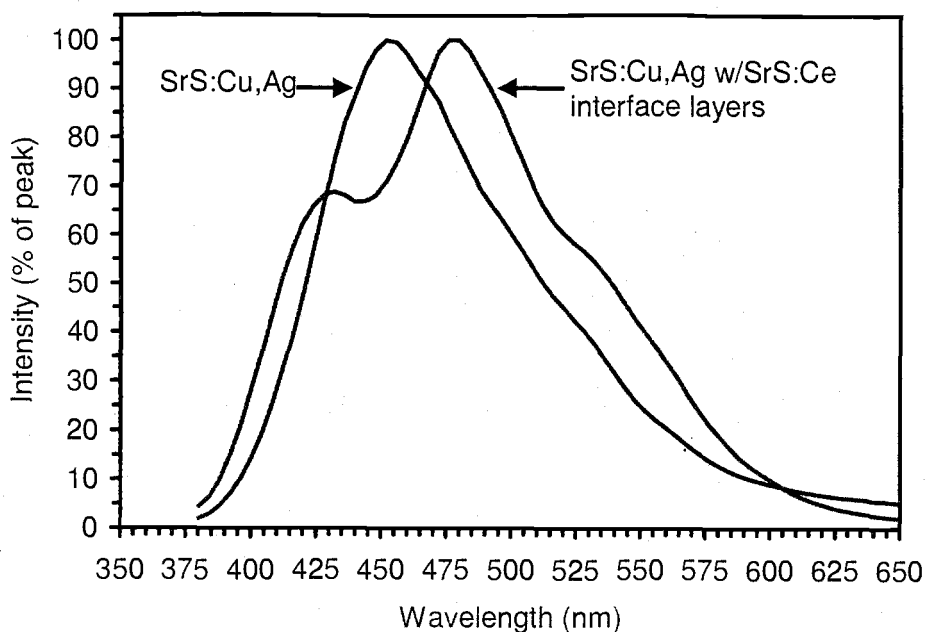


Figure 5.16: Electroluminescence emission spectra of a sputtered SrS:Cu,Ag ACTFEL device with and without SrS:Ce interface layers.

result is a shift in the CIE coordinates from $x=0.186$, $y=0.264$ at 25°C to $x=0.194$, $y=0.299$ at 50°C .

5.1.5 Summary

A comparison of EL thermal quenching trends observed for various ACTFEL devices considered in this section is summarized in Table 5.1. The first column of Table 5.1 is a comparison of the percent reduction in luminance at 40 V above threshold, $L_{40}\%$. It is evident that evaporated ZnS:Mn ACTFEL devices perform nearly ideally with respect to $L_{40}\%$, exhibiting the least amount of reduction of all of the devices tested. In contrast, SrS:Cu and SrS:Cu,Ag ACTFEL devices show a very strong reduction in $L_{40}\%$, while SrS:Ce and multi-layer SrS:Cu,Ag / SrS:Ce ACTFEL devices are intermediate. Note that a reduction in $L_{40}\%$ may result from either normal or EL thermal quenching. The last three columns of Table 5.1 refer to temperature-dependent electrical properties of the ACTFEL device and thus provide some insight

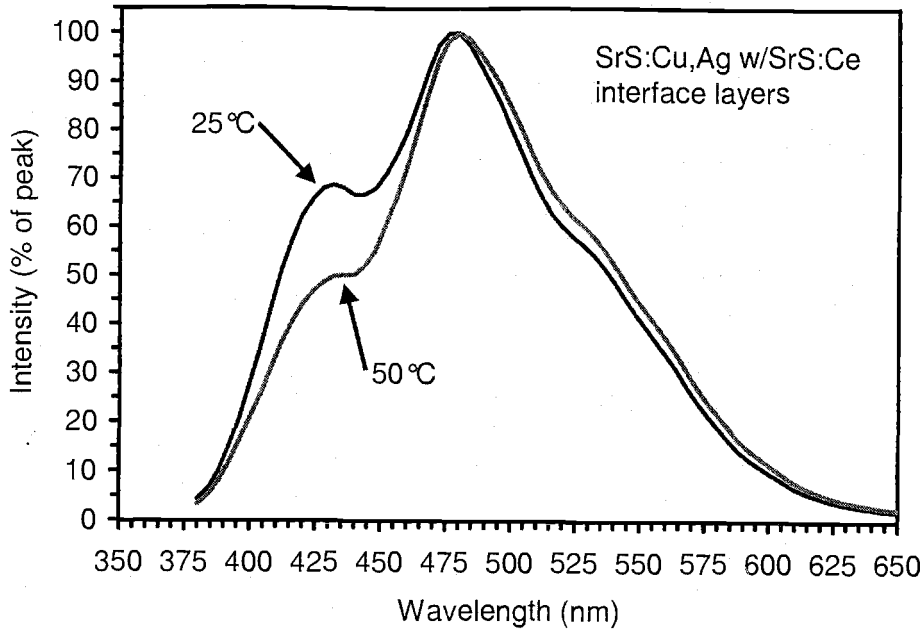


Figure 5.17: Electroluminescence emission spectra of a sputtered SrS:Cu,Ag ACTFEL device with SrS:Ce interface layers at 25 and 50°C.

into how much of the thermal quenching is normal and how much is EL thermal quenching in origin; the larger the change in threshold voltage (V_{th}), transferred charge at 40 V above threshold (Q_{40}^{ext}), or transferred charge capacitance overshoot (i.e. dQ_{max}/dV_{max} overshoot) with temperature, the larger the contribution of EL thermal quenching. With this in mind, the trend shown in the last three columns of Table 5.1 clearly indicates that SrS:Cu and SrS:Cu,Ag ACTFEL devices are dominated by EL thermal quenching, whereas SrS:Ce and multi-layer SrS:Cu,Ag / SrS:Ce ACTFEL devices are dominated by normal thermal quenching. Finally, the results in Table 5.1 indicate that single-layer SrS:Cu and SrS:Cu,Ag ACTFEL devices exhibit a large amount of EL thermal quenching, whereas the extent of EL thermal quenching is significantly reduced in the multi-layer SrS:Cu,Ag / SrS:Ce ACTFEL device.

In SrS:Ce ACTFEL devices, space charge generation occurs via trap-to-band impact ionization and EL thermal quenching is negligible. In SrS:Cu, space-charge

Table 5.1: Summary of electroluminescence thermal quenching properties for several types of ACTFEL device. Values represent differences between measurements at 25°C and 50°C.

Phosphor	L_{40} % change	V_{th} change (V)	Q_{40}^{ext} % change	$\frac{dQ_{max}}{dV_{max}}$ overshoot change
ZnS:Mn (evaporated)	-6	2	-<1	slight decrease
ZnS:Mn (ALE)	0	0	0	slight increase
SrS:Ce (ALE)	-15	2	+2	no change
SrS:Cu	-45	10	-12	decreases
SrS:Cu,Ag	-40	14	-25	decreases
SrS:Ce/SrS:Cu,Ag /SrS:Ce	-15	4	-1	no change

generation occurs in the bulk via band-to-band impact ionization and hole trapping. EL thermal quenching is strong in SrS:Cu because hole trap emission increases with increasing temperature. The decrease in space charge with increasing temperature results due to decreased hole trap occupation. In the SrS:Ce / SrS:Cu,Ag hybrid device, electron injection is not decreased at higher temperature because a temperature independent mechanism is provided by the SrS:Ce layers. The SrS:Ce layers provide a suitable amount of space-charge generation and compensate for the space-charge reduction that would occur in a single SrS:Cu layer device, so that the space charge density is not radically reduced at higher temperature.

5.2 Spectral shift with temperature of SrS:Cu ACTFEL devices

There is a green shift with decreasing temperature in the EL spectrum of blue emitting SrS:Cu ACTFEL devices, as shown in Fig. 5.18. On the basis of lifetime data and the relative strength of the excitation transition $^1A \rightarrow ^1E_g$, it is generally

agreed that the green emission band resulting from cooling the room-temperature blue-emitting samples is associated with an off-center positional distortion of the Cu^+ ion. [88, 89] It is also agreed that in order for the observed temperature-dependent excitation phenomena to occur in $\text{SrS}:\text{Cu}$, the Cu must sit at an off-center lattice site position at low temperature and shift to an on-center position as the temperature increases. [115] Thus, the green shift with decreasing temperature in the emission of $\text{SrS}:\text{Cu}^+$ ACTFEL devices is a result of Cu^+ moving off-center from an on-center position.

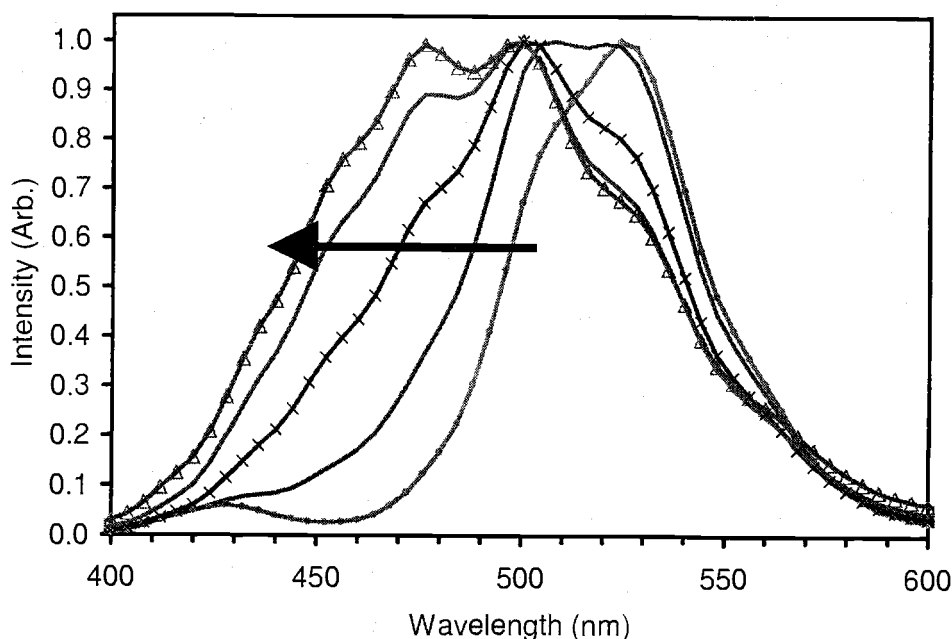


Figure 5.18: EL spectra for a sputtered $\text{SrS}:\text{Cu}$ ACTFEL device at temperatures of 30, 100, 175, 250, and 325 K (arrow indicates increasing temperature).

When a $\text{SrS}:\text{Cu}$ ACTFEL device is co-doped with Ag, the low temperature EL emission spectrum is dominated by a peak at ~ 430 nm, blue shifted from the room temperature spectrum, as shown in Fig. 5.19. A second peak is also present at ~ 530 nm. The lower wavelength (higher energy) peak is attributed to Ag^+ emission and the

higher wavelength (lower energy) peak is due to Cu^+ emission. As the temperature increases, the Ag^+ emission is quenched, while the Cu^+ emission blue shifts. The Ag^+ peak does not shift appreciably, since the ionic size of Ag^+ does not permit a large off center positional distortion to occur on a Sr^{2+} site in SrS. The EL emission spectrum resulting at higher temperatures is a mixture of the blue Cu^+ and deep blue Ag^+ emission.

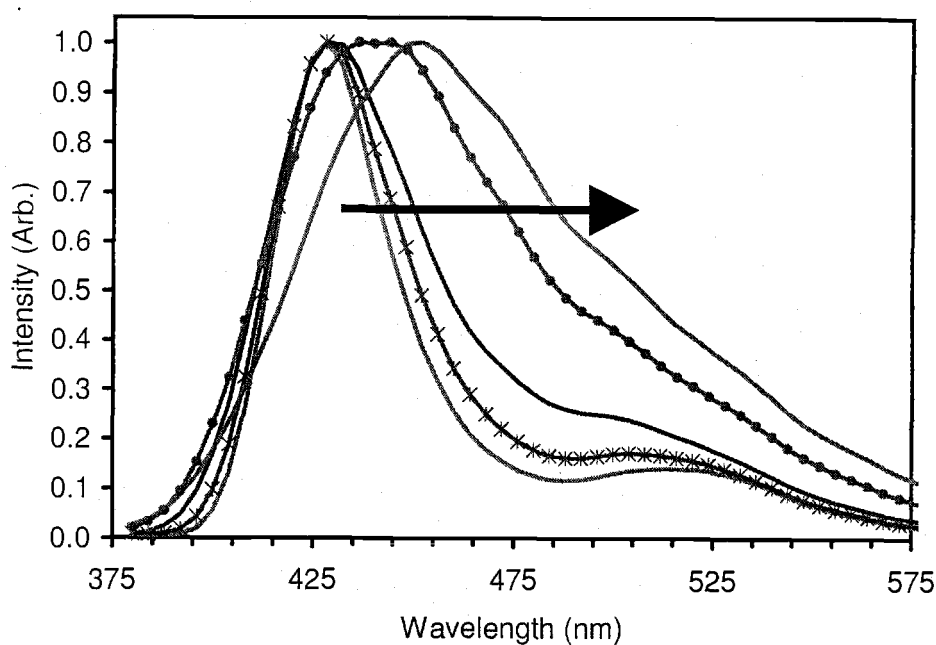


Figure 5.19: EL spectra for a sputtered SrS:Cu,Ag ACTFEL device at temperatures of 30, 100, 175, 250, and 325 K (arrow indicates increasing temperature).

5.3 Space charge in SrS:Cu ACTFEL devices

Some space charge related effects on the operation of SrS:Cu ACTFEL devices are examined in this section. The first effect examined is the dependence of the space charge density on temperature in SrS:Cu ACTFEL devices. The space charge

density dependence on temperature is found to vary differently in different temperature regimes. The effect of co-dopants on the space charge density of SrS:Cu is also examined.

5.3.1 Temperature dependence of space charge density in SrS:Cu ACTFEL devices

In Section 5.1.3, the threshold voltage of SrS:Cu ACTFEL devices is shown to increase with increasing temperature. Consider the effect of space charge on the threshold voltage. The threshold voltage is reached when the cathode field is high enough to inject electrons from deep traps at the phosphor/insulator interface. If positive space charge exists in the phosphor bulk, the cathode field is enhanced, and the threshold voltage is reached at an applied voltage lower than it would be if no space charge were present, as discussed in Section 2.1.2. Now consider the transferred charge curves for a SrS:Cu ACTFEL device exhibiting EL thermal quenching, as shown in Fig. 5.20. The sample studied is a sputtered SrS:Cu,Ga ACTFEL device that is 1.1 μm thick, with a 200 nm ATO bottom insulator and 300 nm BTO top insulator. The device is aged at room temperature for an hour at 40 V above V_{th} with a 3 kHz waveform prior to characterization. Measurements are performed with a 60 Hz bipolar trapezoidal waveform. The portion of the 25°C curve just above threshold undergoes a sharp rise before leveling off and increasing with a slope near the insulator capacitance value. The same portion of the 50°C curve undergoes a more gradual increase than the 25°C curve. Since it is assumed that the slope of the step immediately above V_{th} in a Q_{max} - V_{max} curve is proportional to the phosphor space charge density, the decrease in step size with temperature is assumed to be due to a decrease in space charge in the phosphor.

An estimate of the space charge density in an ACTFEL phosphor can be made from a Q_{max} - V_{max} curve. The density of space charge in the phosphor may be

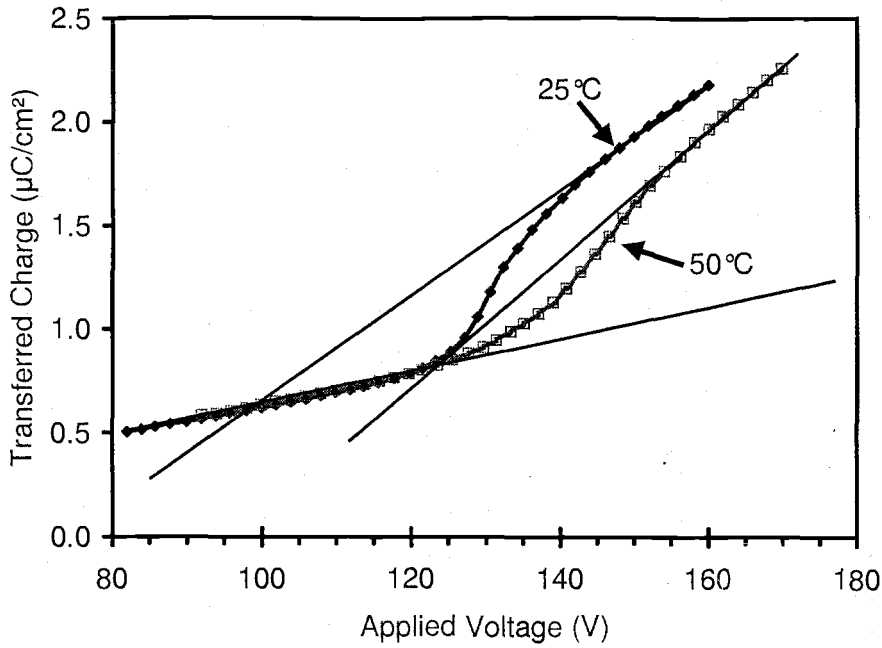


Figure 5.20: Q_{max} - V_{max} curves for a sputtered SrS:Cu,Ga ACTFEL device at 25 and 50°C.

estimated by

$$\rho = 2C_{tot} \frac{\Delta V}{d_p} \quad (5.1)$$

where C_{tot} is the total capacitance of the ACTFEL device, d_p is the thickness of the phosphor layer, and ΔV is the difference in V_{th} and the effective space charge threshold voltage V_{th}^α . [116] The effective space charge threshold voltage V_{th}^α is the voltage that would be the threshold voltage if space charge was established in the phosphor at low applied voltages, rather than at higher sub-threshold voltages, where it is believed to be generated. [116] The value of V_{th}^α may be estimated by extrapolating the slope of the Q_{max} - V_{max} curve above V_{th} back to the intersection with the Q_{max} - V_{max} curve below threshold. The space charge density estimate obtained in this manner is highly sensitive to the extrapolation of the above-threshold slope and the threshold voltage values.

Applying the space charge density estimation procedure described above to the Q_{max} - V_{max} curves in Fig. 5.20 gives a quantitative assessment of the decrease in space charge with temperature. The threshold voltages estimated from Fig. 5.20 and resulting space charge density estimates are given in Table 5.2. The estimated values show that the space charge density is reduced from $1.8 \times 10^{16} \text{ cm}^{-3}$ to $1.1 \times 10^{16} \text{ cm}^{-3}$ upon increasing the temperature from 25 to 50°C .

Table 5.2: Estimated threshold voltage values and space charge density estimates for a 1100 nm sputtered SrS:Cu,Ga ACTFEL device at 25 and 50° .

T ($^\circ\text{C}$)	V_{th} (V)	V_{th}^α (V)	ρ_{sc} (10^{16} cm^{-3})
25	125	100	1.8
50	139	123	1.1

The decrease in space charge density results in less cathode field enhancement at the higher temperature, which causes the threshold voltage to increase with temperature. The threshold voltage increases since the decrease in cathode field enhancement must be compensated by a larger applied voltage. If a uniform distribution of space charge in the phosphor is assumed, the magnitude of the cathode field may be calculated using the expression

$$F_p^{ave} = F_p^{cathode} - \frac{\rho d_p}{2\epsilon_p} \quad (5.2)$$

where F_p^{ave} is the measured, average field, $F_p^{cathode}$ is the cathode field at the cathode phosphor/insulator interface, ϵ_p is the phosphor dielectric constant, d_p is the phosphor layer thickness, and ρ is the space charge density. If ρ is assumed from the Q_{max} - V_{max} estimate and the average phosphor field F_p^{ave} is measured in a Q - F_p experiment, then $F_p^{cathode}$ may be found for 25 and 50°C . The cathode field values calculated with Eq.

5.2, along with the values of ρ estimated from the Q_{max} - V_{max} curves in Fig. 5.20 and the measured values of F_p^{ave} , are given in Table 5.3. Note that the decrease in space charge density and cathode field enhancement at 50°C is accompanied by an increase in F_p^{ave} . The cathodic phosphor field values at 25 and 50°C are effectively equal, within the experimental error arising from the estimation of ρ . As the temperature increases, in order to reach the higher average field required to obtain a cathodic field high enough for injection, the threshold voltage increases. Note that this 1.3 MV/cm estimate of the SrS cathode field is significantly smaller than the 2.2 MV/cm estimate of the ZnS cathode field. [22, 55] Thus, electron emission occurs from energy levels that are significantly more shallow in SrS than in ZnS. Assuming pure tunnel emission from a cathode trap at a cathode field of 2.2 MV/cm leads to an estimated trap depth of 1.5 eV for ZnS. A similar calculation for SrS at a cathode field of 1.3 MV/cm results in an estimated trap depth of 1.0 eV for $m^*=0.18$ (i.e. the electron effective mass for ZnS) or 0.73 eV for $m^*=0.5$ (i.e. a typical conductivity effective mass for electrons in SrS based on band structure calculations). [117] Thus, even though the energy depth of the trap responsible for injection in SrS cannot be precisely specified due to an uncertainty in the tunneling effective mass, it can be confidently concluded that this trap is significantly more shallow than the corresponding trap in ZnS.)

Table 5.3: Estimated cathode field values for a 1100 nm sputtered SrS:Cu,Ga ACT-FEL device at 25 and 50°C, along with experimentally determined average phosphor field and space charge density.

T (°C)	ρ_{sc} (10^{16} cm^{-3})	F_p^{ave} (MV/cm)	$\frac{\rho d_p}{2\epsilon_p}$ (MV/cm)	$F_p^{cathode}$ (MV/cm)
25	1.8	1.10	0.197	1.30
50	1.1	1.15	0.122	1.27

The phenomenon of EL thermal quenching in SrS:Cu ACTFEL devices just above room temperature has spawned the investigation of SrS:Cu ACTFEL device operation over a broader temperature range. The device studied above is cooled in a closed-cycle He refrigerator system. Subsequent measurements taken at higher temperatures are performed ~ 45 minutes after the system has warmed to the set temperature.

The dependence on temperature of the SrS:Cu ACTFEL device is apparent in the Q_{max} - V_{max} curves, shown in Fig. 5.21, taken with a 60 Hz bipolar trapezoidal waveform at 50, 100, 200, 250, and 300 K. Note that the effects of EL thermal quenching do not influence the device operation until the temperature increases above 250 K. Up to 250 K, the threshold voltage is relatively constant while the above threshold transferred charge increases with temperature. Also increasing with temperature is the Q_{max} - V_{max} step just above V_{th} , attributed to the formation of positive space charge in the phosphor layer. From 250 to 300 K, V_{th} increases significantly, causing a p-shift in the Q_{max} - V_{max} curve, the signature of the effect known as EL thermal quenching, discussed in Section 5.1.

The Q_{max} - V_{max} step immediately above V_{th} increases from 75 K up to 250 K, while the magnitude of V_{th} is relatively constant. The step height increase with temperature is assumed to be the effect of an increase in the phosphor space charge density. In theory, an increase in phosphor space charge would enhance the cathode field and lower the threshold voltage. However, if the increasing space charge is dynamic space charge, which is only created at or above threshold, the threshold voltage would not change. Also, it is possible that the magnitude of the space charge density created below threshold in this case is too small to cause the threshold voltage to decrease. An estimate of the space charge density can be made from the Q_{max} - V_{max} curve using the slope extrapolation method explained previously in this subsection. The threshold voltages and resulting space charge densities are shown in Table 5.4. These estimates yield space charge densities that are constant from 50 to

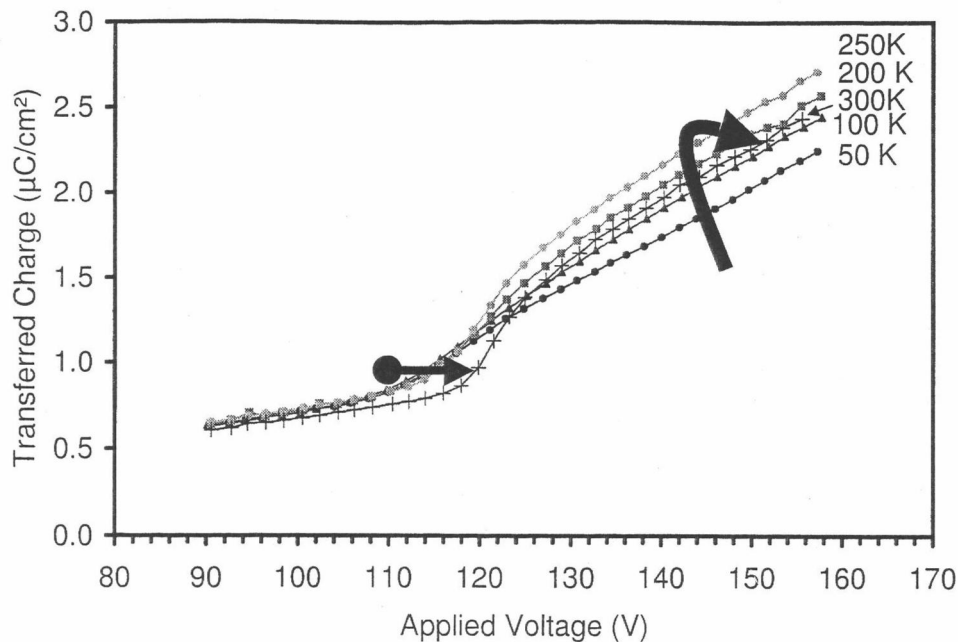


Figure 5.21: Q_{max} - V_{max} curves for a sputtered SrS:Cu ACTFEL device at temperatures of 50, 100, 200, 250, and 300 K (arrow indicates increasing temperature).

75 K, increase over the range of 75 to 250 K, and decrease above 250 K. The decrease above 250 K is accompanied by an increase in V_{th} . Below 250 K, the threshold voltage is relatively unchanged as ρ_{sc} increases. The space charge density below 200 K is on the order of 10^{15} cm^{-3} , which according to Eq. 5.2 results in a cathode field enhancement on the order of 0.01 MV/cm. This is likely too small of an enhancement to significantly change V_{th} .

An Arrhenius plot of the space charge density estimates in Table 5.4 over the temperature range of 75 to 250 K is given in Fig. 5.22. The Arrhenius analysis of ρ_{sc} yields an activation energy of 0.02 eV. The value of $E_a = 0.02 \text{ eV}$ is found assuming a purely exponential space charge generation mechanism having the form

$$\rho_{sc} = C e^{-E_a/k_B T}. \quad (5.3)$$

This suggests that the increase in the Q_{max} - V_{max} step height above threshold is due to an increase in space charge generation that is thermally-activated. This is not to

Table 5.4: Phosphor space charge density and threshold voltage estimates at various temperatures for an 1100 nm sputtered SrS:Cu,Ga ACTFEL device.

T (K)	V_{th} (V)	V_{th}^a (V)	ρ_{sc} (10^{15} cm^{-3})
50	108	106	1.44
75	108	106	1.44
100	109.5	105	3.24
150	108	100	5.76
200	110	95	10.9
250	112	92.5	14.0
300	116	98.5	12.6

say that there is an energy level 0.02 eV below the conduction band, since the effect of the electric field on the emission rate (e.g. phonon assisted tunneling) is ignored in this simple Arrhenius assessment. Rather, this assessment indicates that a very modest amount of extra thermal energy is required in order to increase the space charge density.

5.3.2 Effect of Na coactivation on space charge density in SrS:Cu ACTFEL devices

The coactivation of SrS:Cu with Na produces dramatic changes in the optical, electrical, and electro-optical ACTFEL device characteristics. [97, 98, 104] The most obvious effect is the drastic color shift from blue to green caused by the influence of S vacancies on the local Cu^+ environment. [90, 97] A more subtle and less understood effect is the reduction of space charge generation in the phosphor with Na coactivation. [98, 104] The almost complete elimination of space charge effects in SrS:Cu,Na ACTFEL devices reduces the power consumption and likely improves the efficiency of these devices. The change in space charge density manifests itself in the

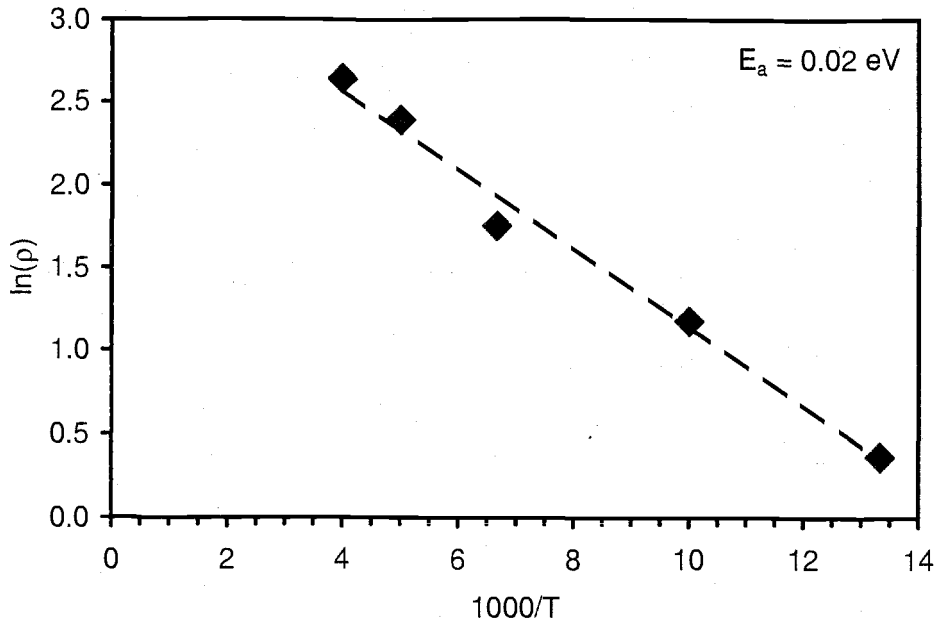


Figure 5.22: Arrhenius plot of space charge density estimate.

Q_{max} - V_{max} curves shown in Fig. 5.23. The phosphor in the device under study is prepared by electron-beam evaporation of undoped SrS with simultaneous thermal co-evaporation of CuF_2 . NaF is evaporated onto one-half of the sample and diffuses into the phosphor during the subsequent RTA process. Space charge generation is evident in Q_{max} - V_{max} curves by the appearance of a large-slope region of the curve just above the threshold voltage, which changes to a smaller slope at higher applied voltages. A large-slope region is evident in the Q_{max} - V_{max} curve of the SrS:Cu,F device in Fig. 5.23, while it is absent for the Q_{max} - V_{max} curve of the SrS:Cu,Na,F device. As a result, it can be concluded that NaF fluxing reduces the amount of space charge in the phosphor layer of a SrS:Cu ACTFEL device.

The Q_{max} - V_{max} step size method for estimating the space charge density used previously in Sec. 5.3.1 is again employed. From the curves shown in Fig. 5.23, the values of ΔV may be estimated and used to calculate an estimated value of the space charge density in SrS:Cu with and without Na coactivation. For these devices,

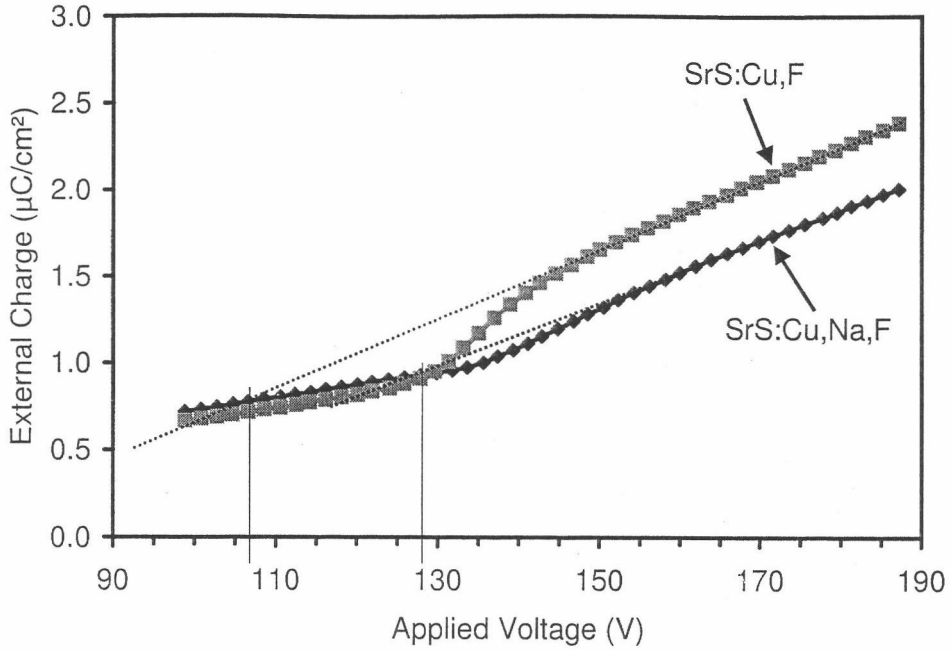


Figure 5.23: Q_{max} - V_{max} curve comparison of a SrS:Cu,F ACTFEL device with and without NaF fluxing.

the values of d_p and C_{tot} are 750 nm and 7.5 nF/cm², respectively. Using a value of $\Delta V = 25$ V in Eq. 5.1 gives a value for the space charge density in SrS:Cu of $\rho_{SrS:Cu} = 3.1 \times 10^{16} \text{ cm}^{-3}$. The addition of NaF to the SrS:Cu phosphor results in a reduction of space charge and an increase in threshold voltage, as observed in Fig. 5.23. With a value of $\Delta V = 5.7$ V, the space charge density of SrS:Cu,Na is found to be $\rho_{SrS:Cu,Na} = 7.1 \times 10^{15} \text{ cm}^{-3}$.

This estimate of phosphor space charge density leads to the conclusion that the addition of NaF to SrS:Cu eliminates $\sim 75\%$ of the space charge present in the phosphor. The elimination of space charge in SrS:Cu,Na devices results in a larger average phosphor field, which is observed in Q - F_p curves of these devices (not shown). A larger average phosphor field leads to a hotter electron distribution and more efficient impact excitation of Cu⁺ luminescent impurities. The addition of NaF also results in less charge transfer, which improves the luminous efficiency since less power

is consumed during ACTFEL device operation. It should be noted that NaF is likely to enhance the crystallinity of the SrS:Cu phosphor, which also leads to a hotter electron distribution, and serves to improve the luminous efficiency.

6. CONCLUSIONS AND RECOMMENDATIONS FOR FUTURE WORK

6.1 Conclusions

One aspect of this thesis has focused on ACTFEL phosphor fabrication. A high-luminance, high-efficiency, full-color ACTFEL phosphor system, capable of being processed at temperatures below the glass substrate melting temperature, has been developed through the use of source layer diffusion doping of ALE deposited SrS thin-films. This processing methodology should prove useful for manufacturing full-color ACTFEL products using a single phosphor host material that does not require color filtering. The development of ACTFEL phosphors has also been advanced through the exploration of alternative phosphor materials. The viability of a $\text{Sr}_x\text{Ca}_{1-x}\text{S}:\text{Eu}$ phosphor as a red-emitting ACTFEL phosphor has been investigated. Preliminary results from electron-beam evaporated $\text{Sr}_x\text{Ca}_{1-x}\text{S}:\text{Eu},\text{Cu}$ ACTFEL devices show that a red phosphor with good luminance, efficiency, and chromaticity can be achieved by alloying of SrS and CaS. It has also been demonstrated that red-emitting ACTFEL devices may be fabricated from $(\text{Ba},\text{Zn})\text{S}$ doped with Mn.

This thesis work has also sought to provide a better understanding of ACTFEL device operation, especially $\text{SrS}:\text{Cu}$ ACTFEL devices. A comparison of "EL" thermal quenching trends for evaporated $\text{ZnS}:\text{Mn}$, ALE $\text{ZnS}:\text{Mn}$, ALE $\text{SrS}:\text{Ce}$, sputtered $\text{SrS}:\text{Cu},\text{Ag}$, and sputtered multi-layer $\text{SrS}:\text{Cu},\text{Ag} / \text{SrS}:\text{Ce}$ ACTFEL devices is presented. $\text{ZnS}:\text{Mn}$ ACTFEL devices exhibit the least amount of EL thermal quenching, which is attributed to traditional thermal quenching. $\text{SrS}:\text{Cu}$ and $\text{SrS}:\text{Cu},\text{Ag}$ ACTFEL devices possess the greatest amount of thermal quenching, which is primarily EL thermal quenching. $\text{SrS}:\text{Ce}$ and multi-layer $\text{SrS}:\text{Cu},\text{Ag} / \text{SrS}:\text{Ce}$ ACTFEL devices exhibit a small amount of thermal quenching, which is mainly normal thermal quenching. The extent of EL thermal quenching is significantly reduced in a multi-

layer SrS:Cu,Ag / SrS:Ce ACTFEL device, compared to that of a single-layer SrS:Cu or SrS:Cu,Ag ACTFEL device. The phenomenon of EL thermal quenching in SrS:Cu is investigated using electrical characterization techniques. The effects of EL thermal quenching are attributed to an annihilation of phosphor space charge with increasing temperature above room temperature. The operation of SrS:Cu is examined as a function of temperature and it was found that the space charge density increases with temperature up to ~ 250 K with an activation energy of ~ 0.02 eV. The space charge density in SrS:Cu ACTFEL devices is estimated as $\sim 1.8 \times 10^{16}$, which yields estimates of the cathode phosphor field and the interfacial trap depth of ~ 1.3 MV/cm and ~ 0.73 eV, respectively.

6.2 Recommendations for future work

The research conducted during the course of this work has uncovered new questions that remain unanswered. The purpose of this section is to give an overview of recommendations for further advancement of the studies presented in this thesis. Recommendations are made concerning future ACTFEL phosphor processing research, followed by suggestions for future ACTFEL device characterization experiments.

6.2.1 Recommendations for future ACTFEL fabrication

Several areas of the SrS ALE/SLDD full-color phosphor development research initiated remain in need of further development. One area of interest is the development of a photolithography process to pattern sub-pixels in an active-matrix electroluminescent (AMEL) display. To make a full-color AMEL display, the dopant needs to be patterned to form each sub-pixel. A technique should be developed to mask each sub-pixel, deposit the required dopants, and etch the mask material.

A higher quality blue phosphor, suitable for commercial full-color applications, can be achieved through optimization of the annealing of SrS:Cu,Ag,Cl,GaF₃. The low temperature processing of SrS:Cu,Cl,GaF₃ by the ALE/SLDD technique should

be further developed through the optimization of furnace and/or vacuum annealing process conditions. The ideal annealing conditions for blue ALE/SLDD SrS phosphor films would also likely be appropriate for green and red SrS phosphors as well, so that a single drive-in diffusion step could be performed for all three pixels in a full-color SrS system. The dopant concentrations in ALE/SLDD SrS:Cu,Ag,Cl,GaF₃ should also be optimized for saturated blue emission. The research presented in Section 4.1.1 suggests that a saturated blue ACTFEL device with good luminance and efficiency is possible by slightly increasing the Ag concentration from that used. It would also be interesting to try other co-activators similar to GaF₃ like AlF₃ or InF₃, in an attempt to improve on the effect that occurs with GaF₃.

With the development of Sr_{1-x}Ca_xS doped with Eu for a red ACTFEL phosphor underway, green and blue Sr_{1-x}Ca_xS phosphors are necessary to create a single host, full-color ACTFEL system. It should be possible to obtain a more saturated blue color than that of SrS:Cu with Sr_xCa_{1-x}S:Cu. The most attractive approach to achieve green is to co-activate Sr_{1-x}Ca_xS:Cu with KF or NaF and assess the luminance, efficiency, and especially color coordinates. A green Sr_xCa_{1-x}S phosphor is possible with Cu doping and KF or NaF co-doping, if the emission shifts far enough to give good green color. It is of interest to determine the Cu peak position as a function of x, and to relate the chromaticity to luminance, since blue shifting the emission decreases the luminance because of the photopic response of the human eye. Such results would also serve to determine the optimal Sr/Ca ratio for co-activating Sr_{1-x}Ca_xS:Eu with Cu.

It would also be interesting to perform an optimization of the Ce source material and concentration for SLDD of ALE SrS. The preliminary investigation of preparing SrS:Ce by the ALE/SLDD technique shows promising results. Further optimization of this technique may produce ACTFEL devices superior to conventional ALE SrS:Ce devices. A Ce concentration study could easily be performed by varying the source layer thickness. The use of a source material other than CeCl₃, such as CeF₃, or the

combination of CeH_3 ($\text{H}=\text{F}, \text{Cl}$) with GaF_3 or KF , may enhance Ce incorporation into SrS and produce superior phosphor layers. It would also be interesting to study the effects of co-doping ALE SrS:Ce by SLDD on the emission spectra and electrical characteristics. Various “flux” materials, such as NaF and GaF_3 , have been shown to significantly alter and improve the performance of ALE/SLDD SrS:Cu ACTFEL devices. It may be possible to further improve the already good performance of ALE SrS:Ce with such coactivation.

The vast number of unexplored phosphor host materials remains a tempting call to any researcher seeking improved ACTFEL devices. Materials such as BaS , $\text{Y}_2\text{O}_2\text{S}$, Y_2SiO_5 , SrGa_2S_4 , and Ba_2ZnS_3 could potentially make good ACTFEL phosphor hosts, but have not been sufficiently investigated.

In light of the reduction in EL thermal quenching of SrS:Cu ACTFEL devices with the introduction of SrS:Ce interface layers, a thorough investigation of interface layers in SrS:Cu ACTFEL devices should be undertaken. Simulation suggests that the threshold voltage shift observed in SrS:Cu ACTFEL devices caused by increasing the temperature can be reduced by altering the phosphor space charge distribution so that it exists some distance away from the phosphor-insulator interface. Therefore, it may be possible to achieve a reduction in EL thermal quenching using materials other than SrS:Ce as the interface layer; such possibilities include undoped ZnS, SrS, BaS, etc. An investigation into the effect of the interface layer thickness on the electrical and optical properties of ACTFEL devices could also reveal information about the space charge distribution and the dependence of the luminescence mechanism on the phosphor field.

6.2.2 Recommendations for future ACTFEL characterization

Several effects of Ag and GaF_3 on the operation of SrS:Cu,Cl ACTFEL devices have been observed, as introduced in Section 4.1.1. An investigation into the dependence of transferred charge, V_{th} , and space charge generation on Ga and Ag

concentration is warranted. A careful study including standard ACTFEL electrical characterization (Q-V, Q-F_p, C-V) and thermally stimulated luminescence (or similar) experiments should reveal the nature of Ga and Ag impurities, and lead to a conclusion on the source of their effect on SrS:Cu device operation. It is also possible that the observed effects are related to grain growth and the residence of impurities on grain boundaries. A scanning electron microscopy (SEM) study of the effects of annealing and of different dopant layers, especially KF and GaF₃, on the grain growth of ALE/SLDD SrS is certainly warranted and would be useful in helping to interpret the observed behavior and in relating grain size and polycrystallinity to ACTFEL device characteristics.

It would also be useful to have a better understanding of the dopant distribution in ALE/SLDD SrS:Cu ACTFEL devices. An initial Rutherford backscattering (RBS) profile of an ALE/SLDD SrS:Cu,Cl device shows a majority of the Cu dopant diffusing completely through the SrS host and collecting at the bottom phosphor-insulator interface. It may be possible to obtain a qualitative or relative dopant concentration depth profile using Auger electron spectroscopy (AES). The dopant concentrations are probably too low to give an accurate estimate, but a relative concentration as a function of distance into the phosphor might be obtainable with AES. A more accurate impurity concentration characterization method should be sought out to obtain a better estimate. Correlation of the source layer thickness and the dopant concentration in the phosphor film would prove beneficial to the understanding of Cu diffusion in SrS.

When phosphor films such as Sr_xCa_{1-x}S:Eu, Sr_xCa_{1-x}S:Cu, and Sr_xBa_{1-x}S:Cu are deposited by electron-beam evaporation, differences between the film composition and that of the pellet source material are apparent in the differences between the emission spectra. An accurate estimate of the film stoichiometry should be possible using AES. Therefore, it is recommended to perform AES on alloyed phosphor host materials to determine the relation of film stoichiometry to that of the pellet or target.

The Q_{max} - V_{max} space charge estimation method is an interesting analysis technique that deserves further utilization. Applying this method to a series of Q_{max} - V_{max} curves taken with applied voltage waveforms of different frequencies should be undertaken to estimate the lifetime of space charge in the phosphor bulk. This should serve to resolve any debate about differences between static and dynamic space charge, and reveal further information about the origins of phosphor space charge. Information about the origin of space charge and about ACTFEL device operation is also obtainable by performing TSL and TTL experiments on SrS:Cu to determine the trap depth due to various impurity or interface states in the devices.

BIBLIOGRAPHY

1. E. N. Harvey, *A History of Luminescence*. The American Philosophical Society, 1957.
2. A. G. Fischer, R. E. Shrader, and S. Larach, "Luminescence of solids (with emphasis on electroluminescence)," in *Photoelectronic materials and devices* (S. Larach, ed.), ch. 1, pp. 1-99, Princeton, New Jersey: D. Van Nostrand Company, Inc., 1965.
3. G. Destriau, "Recherches sure les scintillations des sulfures de zinc aux rayons," *J. Chim. Physique*, vol. 33, pp. 587-625, 1936.
4. N. A. Vlasenko and Y. A. Popkov, "The electroluminescence of sublimate phosphor zns mn," *Optika i Spektroskopiya*, vol. 8, no. 1, pp. 81-8, 1960.
5. T. Inoguchi, M. Takeda, Y. Kakihora, and M. Yoshida, "Stable high luminance thin-film electroluminescent panels," *SID Digest*, vol. 5, p. 84, 1974.
6. Y. A. Ono, *Electroluminescent displays*. Singapore: World Scientific, 1995.
7. W. E. Howard, "Memory in thin-film electroluminescent devices," *J. Lumin.*, vol. 23, pp. 155-173, 1981.
8. W. E. Howard, O. Sahni, and P. M. Alt, "A simple model for the hysteretic behavior of ZnS:Mn thin-film electroluminescent devices," *J. Appl. Phys.*, vol. 53, pp. 639-647, Jan. 1982.
9. K.-W. C. Yang and S. J. T. Owen, "Mechanisms of the negative-resistance characteristics in ac thin-film electroluminescent devices," *IEEE Trans. Electron Devices*, vol. ED-30, pp. 452-459, May 1983.
10. E. Bringuier, "Charge transfer in ZnS-type electroluminescence," *J. Appl. Phys.*, vol. 66, pp. 1314-1325, Aug. 1989.
11. J. F. Wager and P. D. Keir, *Electrical characterization of thin-film electroluminescent devices*, vol. 27, pp. 223-248. Annual Review of Materials Science, 1997.
12. V. Marrello, L. Samuelson, A. Onton, and W. Reuter, "Probe layer measurements of electroluminescence excitation in ac thin film devices," *J. Appl. Phys.*, vol. 51, pp. 3590-3599, May 1980.
13. J. M. Jarem and V. P. Singh, "A computationally simple model for hysteretic thin-film electroluminescent devices," *IEEE Trans. Electron Devices*, vol. ED-35, pp. 1834-1841, Nov. 1988.

14. K. A. Neyts, D. Corlatan, P. D. Visschere, and J. V. den Bossche, "Observation and simulation of space-charge effects and hysteresis in ZnS:Mn ac thin-film electroluminescent devices," *J. Appl. Phys.*, vol. 75, pp. 5339–5346, May 1994.
15. A. Goldenblum, A. Oprea, and V. Bogatu, "Time behavior of currents in ZnS:Mn metal-insulator-semiconductor-insulator-metal structures," *J. Appl. Phys.*, vol. 75, pp. 5177–5185, May 1994.
16. P. D. Keir, W. M. Ang, and J. F. Wager, "Modeling space charge in alternating-current thin-film electroluminescent devices using a single-sheet charge model," *J. Appl. Phys.*, vol. 78, pp. 4668–4680, Oct. 1995.
17. P. D. Keir, "Modeling phosphor space charge in alternating-current thin-film electroluminescent devices," M.S. thesis, Oregon State University, 1996.
18. T. D. Thompson and J. W. Allen, "Electroluminescence from minority carrier injection produced by deep-level impact ionization," *J. Crystal Growth*, vol. 101, pp. 981–984, 1990.
19. S.-P. Shih, P. D. Keir, and J. F. Wager, "Space charge generation in ZnS:Mn alternating-current thin-film electroluminescent devices," *J. Appl. Phys.*, vol. 78, pp. 5775–5781, Nov. 1995.
20. E. Bringuier, "Tentative anatomy of ZnS-type electroluminescence," *J. Appl. Phys.*, vol. 75, no. 9, pp. 4291–4312, 1994.
21. E. Bringuier, "Charge transfer in ZnS-type electroluminescence revisited," *Appl. Phys. Lett.*, vol. 60, no. 10, pp. 1256–1258, 1992.
22. J. C. Hitt, "Static space charge in evaporated ZnS:Mn alternating-current electroluminescent devices," M.S. thesis, Oregon State University, 1998.
23. J. C. Hitt, J. P. Bender, and J. F. Wager, *Thin-film electroluminescent device physics modeling*, vol. 25, pp. 29–85. Critical Reviews in Solid State and Material Sciences, 2000.
24. J. B. Peery, "State space modeling of alternating-current thin-film electroluminescent devices," M.S. thesis, Oregon State University, 1998.
25. G. Vincent, A. Chantre, and D. Bois, "Electric field effect on the thermal emission of traps in semiconductor junctions," *J. Appl. Phys.*, vol. 50, pp. 5484–5487, Aug. 1979.
26. E. Rosencher, V. Mosser, and G. Vincent, "Transient-current study of field-assisted emission from shallow levels in silicon," *Phys. Rev. B: Condens. Matter*, vol. 29, pp. 1135–1147, Feb. 1984.

27. R. Myers and J. F. Wager, "Transferred charge analysis of evaporated ZnS:Mn alternating-current thin-film electroluminescent devices," *J. Appl. Phys.*, vol. 81, pp. 506-510, Jan. 1997.
28. D. Corlatan, K. Neyts, and P. D. Visschere, "The influence of space charge and electric field on the excitation efficiency in thin film electroluminescent devices," *J. Appl. Phys.*, vol. 78, pp. 7259-7264, Dec. 1995.
29. G. O. Muller, "On the efficiency of thin film electroluminescent devices," *Phys. Stat. Sol. (a)*, vol. 139, pp. 263-269, Sept. 1993.
30. F. W. Billmeyer and M. Saltzman, *Principles of color technology*. New York: John Wiley & Sons, second ed., 1981.
31. A. C. Hardy, *Handbook of colorimetry*. Cambridge, MA: The Technology Press, 1936.
32. R. D. Overheim and D. L. Wagner, *Light and color*. New York: John Wiley & Sons, 1982.
33. M. Ando and Y. A. Ono, "Electro- and photo-luminescent quenching effects imposed by field-induced ionization of the Eu^{2+} luminescent centers in CaS:Eu thin films," *J. Appl. Phys.*, vol. 69, no. 10, pp. 7225-7230, 1991.
34. R. S. Crandall, "Mechanism of electroluminescence in alkaline earth sulfides," *Appl. Phys. Lett.*, vol. 50, no. 10, pp. 551-553, 1987.
35. R. S. Crandall, "Light evolution in alkaline-earth-sulfide thin-film a.c. electroluminescent devices," *Appl. Phys. Lett.*, vol. 50, no. 11, pp. 641-643, 1987.
36. R. S. Crandall and M. Ling, "Evidence for recombination-controlled electroluminescence in alkaline-earth sulfides," *J. Appl. Phys.*, vol. 62, no. 7, pp. 3074-3076, 1987.
37. M. Ando and Y. A. Ono, "Role of europium(2+) luminescent centers in the electro-optical characteristics of red-emitting europium-doped calcium sulfide thin-film electroluminescent devices with memory," *Jpn. J. Appl. Phys.*, vol. 68, no. 7, pp. 3578-3583, 1990.
38. K. Ohmi, K. Ishitani, S. Tanaka, and H. Kobayashi, "Role of space charge in SrS:Ce thin-film electroluminescent devices studied by the photoirradiation effect," *Appl. Phys. Lett.*, vol. 67, pp. 944-946, Aug. 1995.
39. K. A. Neyts and E. Soininen, "Space charge and light generation in SrS:Ce thin film electroluminescent devices," *IEEE Trans. Electron Devices*, vol. 42, no. 6, pp. 1086-1092, 1995.

40. K. Ohmi, K. Yamabe, H. Fukada, T. Fujiwara, S. Tanaka, and H. Kobayashi, "Blue SrS:Cu thin-film electroluminescent devices grown by hot-wall deposition using successive source supply," *Appl. Phys. Lett.*, vol. 73, pp. 1889–1891, Sept. 1998.
41. J. Benoit, C. Barthou, P. Benalloul, and K. Polarno, "The electro-optical behavior of SrS:Ce electroluminescent devices under photonic excitation," *J. Appl. Phys.*, vol. 87, pp. 198–202, Jan. 2000.
42. P. Bailey, D. Carkner, and X. Wu, "Trailing edge light emission from ZnS:Mn and ZnS:Tb,F in a thick dielectric electroluminescent display," *J. Appl. Phys.*, vol. 81, pp. 931–936, Jan. 1997.
43. A. A. Douglas, J. F. Wager, D. C. Morton, J. B. Koh, and C. P. Hogg, "Evidence for space charge in atomic layer epitaxy ZnS:Mn alternating-current thin-film electroluminescent devices," *J. Appl. Phys.*, vol. 73, pp. 296–299, Jan. 1993.
44. K. O. Velthaus, R. H. Mauch, H. W. Schock, S. Tanaka, K. Y. and K. Ohmi, and H. Kobayashi, "Efficient electroluminescent devices based on zinc sulfide/cerium-doped strontium sulfide multilayered phosphors," in *Proceedings of the 6th international workshop on electroluminescence* (J. C. McClure and V. P. Singh, eds.), (El Paso), pp. 187–192, Cinco Puntos Press, 1992.
45. C. B. Sawyer and C. H. Tower, "Rochelle salt as a dielectric," *Physical Review*, vol. 35, pp. 269–273, Feb. 1930.
46. D. H. Smith, "Modeling a.c. thin-film electroluminescent devices," *J. Lumin.*, vol. 23, pp. 209–235, 1981.
47. R. C. McArthur, J. D. Davidson, J. F. Wager, I. Khormaei, and C. N. King, "Capacitance-voltage characteristics of alternating-current thin-film electroluminescent devices," *Appl. Phys. Lett.*, vol. 56, pp. 1889–1891, May 1990.
48. J. D. Davidson, J. F. Wager, R. I. Khormaei, C. N. King, and R. Williams, "Electrical characterization and modeling of alternating-current thin-film electroluminescent devices," *IEEE Trans. Electron Devices*, vol. 39, pp. 1122–1128, May 1992.
49. L. V. Pham, "Electrical characterization, maximum charge-maximum voltage (Q_{max} - V_{max}) analysis, aging and temperature studies of thiogallate thin-film electroluminescent devices," M.S. thesis, Oregon State University, 1996.
50. L. V. Pham, J. F. Wager, S. S. Sun, E. Dickey, R. T. Tuenge, and C. N. King, "Electrical characterization of blue electroluminescent devices," in *Advanced Flat Panel Display Technology* (P. S. Friedman, ed.), pp. 190–199, SPIE Proceedings 2174, 1994.

51. A. Abu-Dayah, S. Kobayashi, and J. F. Wager, "Internal charge-phosphor field characteristics of alternating-current thin-film electroluminescent devices," *Appl. Phys. Lett.*, vol. 62, pp. 744-746, Feb. 1993.
52. A. Abu-Dayah, "Internal charge-phosphor field analysis, electrical characterization, and aging studies of ac thin-film electroluminescent devices," M.S. thesis, Oregon State University, 1993.
53. S.-P. Shih, "Electrical characterization and aging studies of ALE ZnS:Mn ACT-FEL devices with varying phosphor thickness," M.S. thesis, Oregon State University, 1996.
54. Y. A. Ono, H. Kawakami, M. Fuyama, and K. Onisawa, "Transferred charge in the active layer and EL device characteristics of TFEL cells," *Jpn. J. Appl. Phys.*, vol. 26, pp. 1482-1492, Sept. 1987.
55. J. C. Hitt, P. D. Keir, J. F. Wager, and S.-S. Sun, "Static space charge in evaporated ZnS:Mn alternating-current thin-film electroluminescent devices," *J. Appl. Phys.*, vol. 83, pp. 1141-1145, Jan. 1998.
56. E. Bringuier, "Electron multiplication in ZnS-type electroluminescent devices," *J. Appl. Phys.*, vol. 67, pp. 7040-7044, June 1990.
57. A. Fuh, R. P. Gallinger, P. Schuster, J. Adolph, and O. Caporaletti, "The effects of post-deposition annealing on ZnS:Mn film crystalline structure and electroluminescent characteristics," *Thin Solid Films*, vol. 10, pp. 202-5, Jan. 1992.
58. Z. K. Kun, D. Leskell, P. R. Malmberg, J. Murphy, and L. J. Sienkiewicz, "The influence of chlorine on the crystal structure and electroluminescent behavior of ZnS:Mn film crystalline structure and electroluminescent characteristics," *J. Electron. Mater.*, vol. 10, pp. 287-300, Jan. 1981.
59. S. Takata, T. Minami, and T. Miyata, "Crystallinity of emitting layer and electroluminescence characteristics in multicolour ZnS thin film electroluminescent device with a thick dielectric ceramic insulating layer," *Thin Solid Films*, vol. 193-4, pp. 481-488, Dec. 1990.
60. Y. Nakanishi, Y. Fukuda, Y. Matanaka, and G. Shimaoka, "The dependence of the polycrystalline structure and electroluminescent properties of ZnS:Mn deposited on Y₂O₃ films on thickness," *Appl. Surf. Sci.*, vol. 48-9, pp. 297-300, May 1991.
61. S. Okamoto, T. Kuki, and T. Suzuki, "SrS:Ce thin-film electroluminescent devices fabricated by post-annealing technique and their electrical properties," *Jpn. J. Appl. Phys.*, vol. 32, no. 4A, pp. 1672-1680, 1993.

62. H. Kina, Y. Tamura, Y. Yamada, and Y. Maruta, "The characteristics of SrS:Ce thin film electroluminescent devices," *Jpn. J. Appl. Phys.*, vol. 36, pp. 150–154, Jan. 1997.
63. R. M. German, *Sintering theory and practice*. New York: John Wiley & Sons, 1996.
64. H. Y. Sun, Y. S. Kim, and S.-H. K. Park, "Fabrication of CaS:Pb blue phosphor by incorporation dimeric Pb^{2+} luminescent centers," *Appl. Phys. Lett.*, vol. 78, no. 6, pp. 721–723, 2001.
65. N. Miura, M. Kawanishi, H. Matsumoto, and R. Nakano, "High-luminance blue-emitting $BaAl_2S_4:Eu$ thin-film electroluminescent devices," *Jpn. J. Appl. Phys.*, vol. 38, no. 11B, pp. L1291–L1292, 1999.
66. J. Robertson and C. W. Chen, "Schottky barrier heights of tantalum oxide, barium strontium titanate, lead titanate, and strontium bismuth tantalate," *Appl. Phys. Lett.*, vol. 74, no. 8, pp. 1168–1170, 1999.
67. V. Pratap, B. K. Verma, and H. B. Lal, "Transport studies on some c-type rare earth sesquioxides," *Proc. Nat. Acad. Sci. India, Sec. A*, vol. 48, no. 1, pp. 20–26, 1978.
68. M. I. Cohen and R. F. Blunt, "Optical properties of strontium metatitanate in the region of the absorption edge," *Phys. Rev.*, vol. 168, no. 3, pp. 929–933, 1968.
69. T. Minami, T. Miyata, S. Takata, and I. Fukuda, "High-luminance green $Zn_2SiO_4:Mn$ thin-film electroluminescent devices using an insulating $BaTiO_3$ ceramic sheet," *Jpn. J. Appl. Phys.*, vol. 33, pp. L117–L119, 1991.
70. P. Atkins, *Physical chemistry*. New York: W. H. Freeman and Company, fifth ed., 1994.
71. G. T. Mearini, "Electron beam evaporation of transparent indium tin oxide." United States Patent No. 6,153,271, Nov. 2000.
72. C. Nunes de Carvalho, A. M. Botelho do Rego, A. Amaral, P. Brogueira, and G. Lavareda, "Effect of substrate temperature on the surface structure, composition and morphology of indium-tin oxide films," *Surf. Coat. Technol.*, vol. 124, no. 1, pp. 70–75, 2000.
73. R. Glang, "Vacuum evaporation," in *Handbook of thin film technology* (L. I. Maissel and R. Glang, eds.), ch. 1, New York: McGraw-Hill, 1970.
74. S. Wolf and R. N. Tauber, *Silicon processing for the VLSI era*, vol. 1: Process technology. Sunset Beach, CA: Lattice Press, 1986.

75. T. S. Moss, R. C. Dye, and R. T. Tuenge, "Production of strontium sulfide coatings by metal organic chemical vapor deposition," *Mater. Res. Soc. Symp. Proc.*, vol. 508, pp. 289–293, 1998.
76. D. Endisch, K. Barth, J. Lau, G. Peterson, A. E. Kaloyeros, D. Tuenge, and C. N. King, "Mocvd srs:ce for applications in electroluminescent devices," *Mater. Res. Soc. Symp. Proc.*, vol. 471, pp. 269–274, 1997.
77. T. Suntola and J. Hyvärinen, *Atomic layer epitaxy*, vol. 15, pp. 177–195. Annual Review of Materials Science, 1985.
78. M. Leskela, L. Niinisto, E. Nykanen, and M. Tammenmaa, "Electroluminescent calcium sulfide thin films doped with terbium(3+) and europium(2+)," *Chemtronics*, vol. 3, no. 2, pp. 113–15, 1988.
79. B. Tuck, *Introduction to diffusion in semiconductors*. Stevenage, England: Peter Peregrinus LTD., 1974.
80. G. Blasse and B. C. Grabmaier, *Luminescent materials*. Berlin: Springer-Verlag, 1994.
81. T. A. Oberacker and H. W. Schock, "Investigations of the influence of halides on the properties of CeX_3 -doped ($\text{X}=\text{Cl}, \text{F}$) strontium sulfide thin film electroluminescent devices," *J. Crystal Growth*, vol. 159, no. 1-4, pp. 935–8, 1996.
82. V. Sannilla, J. Ihanus, M. Ritala, and M. Leskela, "Atomic layer epitaxy growth of BaS and BaS:Ce thin films from in situ synthesized $\text{Ba}(\text{thd})_2$," *Chem. Vap. Deposition*, vol. 4, no. 6, pp. 227–233, 1998.
83. T. A. O'Brien, P. D. Rack, P. H. Holloway, and M. C. Zerner, "Crystal field and molecular orbital calculation of the optical transitions in Ce doped alkaline earth sulfide (MgS , CaS , SrS , and BaS) phosphors," *J. Lumin.*, vol. 78, no. 4, pp. 245–257, 1998.
84. K. O. Velthaus, B. Huttli, U. Troppenz, R. Herrman, and R. H. Mauch, "New deposition process for very blue and bright SrS:Ce,Cl TFEL devices," *Proceedings of the 1997 SID International Symposium*, p. 411, 1997.
85. S.-S. Sun, E. Dickey, R. T. Tuenge, R. Wentross, and J. Kane, "High-performance alkaline-earth thiogallate blue-emitting ACTFEL devices," *J. SID*, vol. 4, no. 4, pp. 305–309, 1996.
86. H. Yamamoto, "Fundamentals of luminescence," in *Phosphor handbook* (S. Shionoya and W. M. Yen, eds.), pp. 35–48, Boca Raton: CRC Press, 1999.
87. N. Yamashita, "Photoluminescence properties of Cu^+ centers in MgS , CaS , SrS , and BaS ," *Jap. J. Appl. Phys.*, vol. 30, pp. 3335–3340, December 1991.

88. N. Yamashita, K. Ebisumori, and K. Nakamura, "Luminescence from the aggregated Cu^+ centers in $\text{SrS}:\text{Cu}$," *Jap. J. Appl. Phys.*, vol. 32, pp. 3846–3850, Sept. 1993.
89. W. M. Li, M. Ritala, M. Leskela, L. Niinisto, E. Soininen, S. S. Sun, W. Tong, and C. J. Summers, "Photo- and electroluminescence of $\text{SrS}:\text{Cu}$ and $\text{SrS}:\text{Ag,Cu,Ga}$ thin films," *J. Appl. Phys.*, vol. 86, no. 9, pp. 5017–5025, 1999.
90. D. Li, *Phosphor development: synthesis, characterization, and chromatic control*. PhD thesis, Oregon State University, 1999.
91. M. Tamatani, "Principal phosphor materials and their optical properties," in *Phosphor handbook* (S. Shionoya and W. M. Yen, eds.), pp. 153–176, Boca Raton: CRC Press, 1999.
92. J. Simonetti and D. S. McClure *Phys. Rev. B*, vol. 16, p. 3887, 1977.
93. Y. E. Perlin and M. Wagner, *The Dynamical Jahn-Teller Effect in Localized Systems*, vol. 7 of *Modern Problems in Condensed Matter Sciences*. North-Holland Physics Publishing, 1984.
94. B. Moine and C. Pedrini, "Kinetic investigations of $\text{NaF}:\text{Cu}$ luminescence," *Phys. Rev. B*, vol. 30, no. 2, pp. 992–996, 1984.
95. S. A. Payne, R. H. Austin, and D. S. McClure, "Effect of a magnetic field on the luminescent lifetime of Cu^+ in alkali halide host crystals," *Phys. Rev. B*, vol. 29, pp. 32–36, Jan. 1984.
96. B. B. Laud and V. W. Kulkarni *J. Phys. Chem. Solid*, vol. 39, p. 555, 1978.
97. D. Li, B. L. Clark, D. A. Kezler, P. D. Keir, and J. F. Wager, "Color control in sulfide phosphors: Turning up the light for electroluminescent displays," *Chem. Mater.*, vol. 12, pp. 268–270, 2000.
98. P. D. Keir, J. F. Wager, B. L. Clark, D. Li, and D. A. Kezler, "Alkali metal coactivators in $\text{srs}:\text{cu,f}$ thin-film electroluminescent devices," *Appl. Phys. Lett.*, vol. 75, pp. 1398–1400, Sept. 1999.
99. W. Park, T. C. Jones, E. Mohammed, C. J. Summers, and S.-S. Sun, "Luminescence properties of $\text{SrS}:\text{Cu,Ag}$ thin-film electroluminescent phosphors," in *Extended abstracts of the fourth international conference on the science and technology of display phosphors / the ninth international workshop on inorganic and organic electroluminescence*, pp. 215–218, Sept. 1998.
100. T. Kano, "Principal phosphor materials and their optical properties," in *Phosphor handbook* (S. Shionoya and W. M. Yen, eds.), pp. 177–200, Boca Raton: CRC Press, 1999.

101. G. Blasse, "Material science of the luminescence of inorganic solids," in *Luminescence of Inorganic Solids* (B. DiBartolo, ed.), p. 457, New York: Plenum Press, 1978.
102. M. Kawanishi, N. Miura, H. Matumoto, and R. Nakano, "Eu²⁺-doped barium thioaluminate EL devices prepared by two-target pulsed-electron-beam evaporation," *J. SID*, vol. 8, no. 3, pp. 247–251, 2000.
103. M. Leskela and L. Niinisto, "Thin films processed by ALE for applications in ACTFEL devices.," in *Proceedings of the 6th International workshop on Electroluminescence*, pp. 249–256, 1992.
104. P. D. Keir, *Fabrication and characterization of ACTFEL devices*. PhD thesis, Oregon State University, 1999.
105. S.-S. Sun, E. Dickey, J. Kane, and P. N. Yocom, "A bright and efficient new blue TFEL phosphor," in *Conference record '97 IDRC*, pp. 301–304, Sept. 1997.
106. S.-S. Sun, "Blue emitting SrS:Ag,Cu TFEL devices," in *Extended abstracts of the fourth international conference on the science and technology of display phosphors / the ninth international workshop on inorganic and organic electroluminescence*, pp. 183–186, Sept. 1998.
107. U. Troppenz, B. Huttli, U. Storz, P. Kratzert, K. O. Velthaus, S.-S. Sun, and R. T. Tuenge, "Photoluminescence and electroluminescence studies on Cu and Ag doped SrS ACTFEL devices," in *Extended abstracts of the fourth international conference on the science and technology of display phosphors / the ninth international workshop on inorganic and organic electroluminescence*, pp. 187–190, Sept. 1998.
108. W. Park, T. C. Jones, and C. J. Summers, "Optical properties of SrS:Cu,Ag two-component phosphors for electroluminescent devices," *Appl. Phys. Lett.*, vol. 74, no. 13, pp. 1785–1787.
109. Y. B. Xin, W. Tong, W. Park, M. Chaichimansour, and C. J. Summers, "Effect of annealing on the grain growth and luminescent properties of srs:cu blue phosphors," *J. Appl. Phys.*, vol. 85, no. 8, pp. 3999 – 4002, 1999.
110. B. A. Baukol, J. C. Hitt, P. D. Keir, and J. F. Wager, "Electroluminescence thermal quenching in thin-film electroluminescent devices," *Appl. Phys. Lett.*, vol. 76, no. 2, pp. 185–187, 2000.
111. W. Lehmann, "Activators and co-activators in calcium sulfide phosphors," *J. Lumin.*, vol. 5, pp. 87–107, 1972.
112. R. D. Shannon, "Revised effective ionic radii and systematic studies of interatomic distances in halides and chalcogenides," *Acta Crystallogr.*, vol. A32, pp. 751–767, Sept. 1976.

113. N. Vlasenko, Y. Kononets, Y. Kopytko, E. Soininen, and S.-S. Sun, "Temperature dependence of luminescence of SrS:Cu(Ag) TFEL display phosphors beyond room temperature," in *Extended abstracts of the fifth international conference on the science and technology of display phosphors*, (San Diego), Nov. 1999.
114. S.-S. Sun and M. Bowen, "Improvement of luminance thermal stability in blue SrS:Cu,Ag ACTFEL devices," in *Conference record '00 IDRC*, Sept. 2000.
115. B. Clark, *Title of Ben's PhD thesis*. PhD thesis, Oregon State University, 2001.
116. J. C. Hitt, *An n-sheet, state-space ACTFEL device model*. PhD thesis, Oregon State University, 2001.
117. A. Hasegawa and A. Yanase, "Electronic structure of strontium monochalcogenides." *J. Phys. C: Solid State Phys.*, vol. 13, no. 10, pp. 1995–1999, 1980.